DISCLAIMER

NATIONAL LABORATORY OF THE ROCKIES

Pumped Thermal Energy Storage Using Low-Cost Particles and a Fluid Bed Heat Exchanger for Maximum Power Efficiency

Zhiwen Ma, Josh McTigue, Jeffrey Gifford, Shin Young Jeong, Jason Hirschey, Umang Patel, Janna Martinek, Munjal Purnkant Shah, and Muhammad Mubashar Ashraf

National Laboratory of the Rockies

The National Laboratory of the Rockies is a national laboratory of the U.S. Department of Energy, Office of Critical Minerals and Energy Innovation, operated under Contract No. DE-AC36-08GO28308.

This report is available at no cost from the National Laboratory of the Rockies (NLR) at www.nlr.gov/publications.

Technical Report
NLR/TP-5700-98019
March 2026

NATIONAL LABORATORY OF THE ROCKIES

Pumped Thermal Energy Storage Using Low-Cost Particles and a Fluid Bed Heat Exchanger for Maximum Power Efficiency

Zhiwen Ma, Josh McTigue, Jeffrey Gifford, Shin Young Jeong, Jason Hirschey, Umang Patel, Janna Martinek, Munjal Purnkant Shah, and Muhammad Mubashar Ashraf

National Laboratory of the Rockies

Suggested Citation
Ma, Zhiwen, Josh McTigue, Jeffrey Gifford, Shin Young Jeong, Jason Hirschey, Umang Patel, Janna Martinek, Munjal Purnkant Shah, and Muhammad Mubashar Ashraf. 2026. *Pumped Thermal Energy Storage Using Low-Cost Particles and a Fluid Bed Heat Exchanger for Maximum Power Efficiency.* Golden, CO: National Laboratory of the Rockies. NLR/TP-5700-98019. https://www.nlr.gov/docs/fy26osti/98019.pdf.

The National Laboratory of the Rockies is a national laboratory of the U.S. Department of Energy, Office of Critical Minerals and Energy Innovation, operated under Contract No. DE-AC36-08GO28308.

This report is available at no cost from the National Laboratory of the Rockies (NLR) at www.nlr.gov/publications.

Technical Report
NLR/TP-5700-98019
March 2026

National Laboratory of the Rockies
15013 Denver West Parkway
Golden, CO 80401
303-275-3000 • www.nlr.gov

NOTICE

This work was authored by the National Laboratory of the Rockies for the U.S. Department of Energy (DOE), operated under Contract No. DE-AC36-08GO28308. Funding provided by the U.S. Department of Energy Office of Energy Efficiency and Renewable Energy (EERE) under the Solar Energy Technologies Office agreement number 38480. The views expressed herein do not necessarily represent the views of the DOE or the U.S. Government.

Cover photos (clockwise from left): Josh Bauer, National Laboratory of the Rockies 61725; Visualization from National Laboratory of the Rockies Insight Center; Getty-181828180; Agata Bogucka, National Laboratory of the Rockies 91683; Dennis Schroeder, National Laboratory of the Rockies 51331; Werner Slocum, National Laboratory of the Rockies 67842.

NATIONAL LABORATORY OF THE ROCKIES

National Laboratory of the Rockies
Final Scientific/Technical Report

Pumped Thermal Energy Storage Using Low-Cost Particles and a Fluid Bed Heat Exchanger for Maximum Power Efficiency

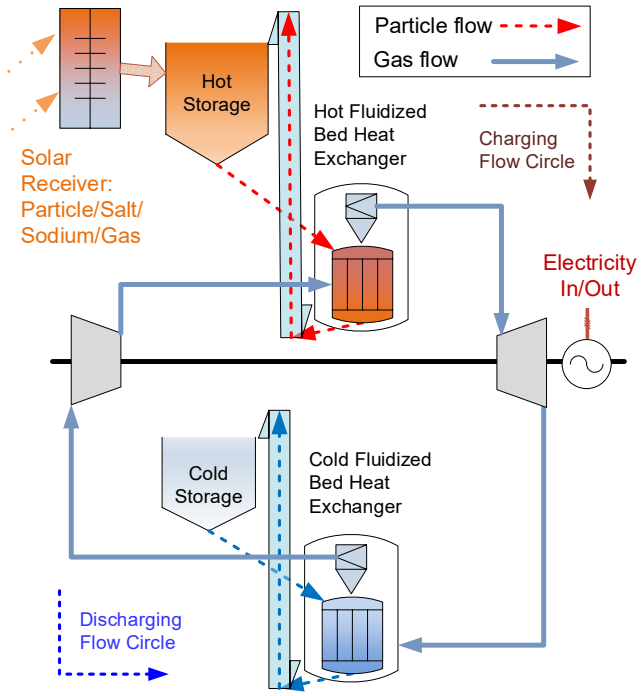

Award Number:	Project CPS #: 38480
Sponsoring Agency	U.S. Department of Energy Solar Energy Technologies Office (SETO)
Lead Recipient:	National Laboratory of the Rockies (NLR)
Project Team Members	Brayton Energy Babcock & Wilcox Modelon Colorado School of Mines
Project Title:	**P**umped Thermal Energy Storage **U**sing Low-Cost Particles and a Fluid Bed Heat Exchanger for **M**aximum **P**ower Efficiency (PUMP)
Program Manager:	David Haas, Rajgopal Vijaykumar
Principal Investigator:	Zhiwen Ma
Contract Administrator:	Jina Martingano
Date of Report:	October 20, 2025
Reporting Period:	October 2022–July 2025

Acknowledgements

This work was authored in part by NLR for the U.S. Department of Energy (DOE), operated under Contract No. DE-AC36-08GO28308. This material is based upon work supported by the U.S. Department of Energy's Office of Energy Efficiency and Renewable Energy (EERE) under the Solar Energy Technologies Office (SETO) Award Number 38480. The views expressed in the article do not necessarily represent the views of the DOE or the U.S. Government. The U.S. Government retains and the publisher, by accepting the article for publication, acknowledges that the U.S. Government retains a nonexclusive, paid-up, irrevocable, worldwide license to publish or reproduce the published form of this work, or allow others to do so, for U.S. Government purposes.

We thank SETO program managers David Haas, Rajgopal Vijaykumar, and Matthew Bauer for their direction and support.

We acknowledge the contributions from Timothy Fuller and Thomas Flynn of Babcock & Wilcox to advise on thermal system and component designs. Project contributors included Dr. Josh McTigue, Dr. Jason Hirschey, Dr. Shin Young Jeong, Dr. Umang Patel, Dr. Munjal Shah, Dr. Jeffrey Gifford, Dr. Janna Martinek, and Dr. Xingchao Wang, Patrick Davenport, and Muhammad Mubashar Ashraf (NLR). The authors thank their NLR colleagues and DOE Program Managers in advising on the project development and reviewing the report. We thank NLR communication experts Susannah Shoemaker for editing the report and Sara Fall for supporting publication of the report.

List of Acronyms

AMIGO	Approximate M-Constrained Integral Gain Optimization
ARPA-E	Advanced Research Projects Agency–Energy
ASME	American Society of Mechanical Engineers
BOM	bill of materials
CAPEX	capital expenditure
CEPCI	Chemical Engineering Plant Cost Index
CFD	computational fluid dynamics
CSP	concentrating solar thermal power
DAYS	Duration Addition to Electricity Storage
DNI	direct normal irradiation
DOE	U.S. Department of Energy
ENDURING	Economic Long-Duration Electricity Storage by Using Low-Cost Thermal Energy Storage and High-Efficiency Power Cycle
FB	fluid bed
FMI	functional module interface
FMU	functional module unit
HATS	Hot Air Testing Station
HX	heat exchanger
IPS	iron pipe size
LCOS	levelized cost of storage
LDES	long-duration electricity storage
LMTD	log mean temperature difference
MIT	Massachusetts Institute of Technology
MFIX	Multiphase Flow With Interphase Exchanges
MS-PTES	molten salt pumped thermal energy storage
NETL	National Energy Technology Laboratory
NLR	National Laboratory of the Rockies
P-PTES	particle pumped thermal energy storage
PFB	pressurized fluid bed
PID	proportional-integral-derivative
PTES	pumped thermal energy storage
SCFM	standard cubic feet per minute
SCO_2	supercritical carbon dioxide
SETO	Solar Energy Technologies Office
TEA	techno-economic analysis
TES	thermal energy storage

Nomenclature

A_b	bed cross-sectional area [m^2]
$c_{p,air}$	specific heat of air [$J \cdot kg^{-1} \cdot K^{-1}$]
$c_{p,p}$	specific heat of particle [$J \cdot kg^{-1} \cdot K^{-1}$]
d_p	particle diameter [m]
g	gravitational acceleration [$m \cdot s^{-2}$]
n_p	particle number density [m^{-3}]
$\dot{m}_{air}$	air mass flow rate [$kg \cdot s^{-1}$]
$\dot{m}_p$	particle mass flow rate [$kg \cdot s^{-1}$]
ΔP	pressure drop [Pa]
$\dot{q}_{p\text{-}air}$	volumetric heat transfer between the particles and air [$W \cdot m^{-3}$]
t	time [s]
T_{air}	air temperature [°C]
T_p	particle temperature [°C]
U_{air}	air velocity [$m \cdot s^{-1}$]
U_p	particle velocity [$m \cdot s^{-1}$]
$\dot{W}_{out}^{dis}$	power output (during discharging)
$\dot{W}_{in}^{chg}$	power input (during charging)
N_h	number of holes
N_m	number of manifolds
D_{head}	diameter of the header in air distributor
D_m	diameter of air distributor manifold

Greek symbols

ε	bed voidage
μ_{air}	dynamic viscosity of air [$kg \cdot m^{-1} \cdot s^{-1}$]
ρ_p	particle density [$kg \cdot m^{-3}$]
ρ_{air}	air/gas density [$kg \cdot m^{-3}$]
ϕ	particle average sphericity
γ	polytropic exponent
η_{fan}	fan efficiency

Executive Summary

Robust, efficient, cost-effective long-duration electricity storage (LDES) solutions can enhance grid resiliency, support existing transmission and distribution infrastructure, and enable a greater share of low-cost, variable alternative energy sources to penetrate the market. To meet this need, the project team at the National Laboratory of the Rockies developed a transformative LDES system based on **p**umped thermal energy storage (TES) **u**sing low-cost particles and a fluid bed heat exchanger for **m**aximum **p**ower efficiency (**PUMP**). The PUMP system is composed of high-temperature, low-cost particle TES coupled with an advanced pressurized fluid bed heat exchanger (PFB HX) that supports a high-efficiency pumped thermal energy storage (PTES) system integrated with concentrating solar thermal power (CSP). The PUMP project developed and de-risked a PFB HX and particle CSP system intended to be integrated with reversible turbomachinery and a modeling tool to assess PTES cost and performance.

The PUMP project focused on system design and key components for stand-alone PTES and hybridized CSP-PTES integrated with particle TES. The team developed modeling tools to optimize cycles and system configurations and a prototype test station for demonstrating a prototype PFB HX in relevant operating conditions to study the novel air/particle direct-contact heat exchanger. The project addressed key component risks, including (1) realizing low air/particle approach temperature in the PFB HX, (2) dehumidification measures to enable particles to be used for cold storage, and (3) integrating reversible turbomachinery.

The PFB HX is unique due to its direct-contact air/particle counterflow design, which eliminates the interfacial heat transfer surfaces and thus dramatically reduces its cost. The PFB HX design requires advanced air/particle flow controls and has the potential to achieve a low approach temperature based on computational fluid dynamics analysis. Prototype testing demonstrated the PFB HX operation and achieved high heat transfer effectiveness. We implemented particle TES for cold storage by eliminating moisture in air or particles for a low-cost, high-efficiency PTES system. Development efforts for critical components and an optimized system will support future pilot demonstration and scale-up of the PTES or hybrid CSP-PTES system.

Cost and performance analyses at the component and system level, based on the modeling tools developed in the project, also show the potential economic benefits of the PUMP system. A bare erected cost estimation using subcomponent material and labor cost inputs shows various deployment paths by leveraging the infrastructure of existing thermal power plants to minimize capital investment. The development indicates that the technology is promising for future demonstration and subsequent implementation. In addition, we explored technology applications beyond electricity storage for industry process heat.

The project involved considerable industry participation, including Brayton Energy (reversible turbomachinery for PTES), Babcock & Wilcox (heat exchanger design, testing, and commercialization), Allied Mineral Products (insulation materials), and Worley Consulting (system integration). These industry participants provided insights into their products and services for component and system designs. The project successfully achieved its technical goals of demonstrating technology feasibility for electrothermal energy storage. The project generated one awarded patent, five published journal papers, and a manuscript in preparation, in addition to numerous conference papers and presentations.

Table of Contents

List of Figures

List of Tables

Project Objectives and Accomplishments

Funded by the U.S. Department of Energy (DOE) Solar Energy Technologies Office (SETO), the National Laboratory of the Rockies (NLR) developed an advanced pumped thermal energy storage (PTES, a.k.a. Carnot battery) system using inexpensive particle-based thermal energy storage (TES) operating in either a stand-alone electricity storage configuration or hybridized with concentrating solar thermal power (CSP). The novel PTES or hybrid CSP-PTES systems offer high-efficiency (>55%) electric energy storage for long-duration (>10 h) energy supply solutions to support a low-cost, reliable electric grid.

Figure 1 shows the schematic of the PTES system developed in this project. The system operates as a thermal battery, which charges the thermal storage by using a heat pump configuration and low-cost, off-peak electricity to heat solid particles. The heated particles are then stored in internally insulated containment silos. At peak demand hours, stored thermal energy is discharged through a fluid bed heat exchanger (HX) to drive a heat engine (reversing the heat pump). The project aims to develop a full-scale system design with round-trip efficiency exceeding 55%.

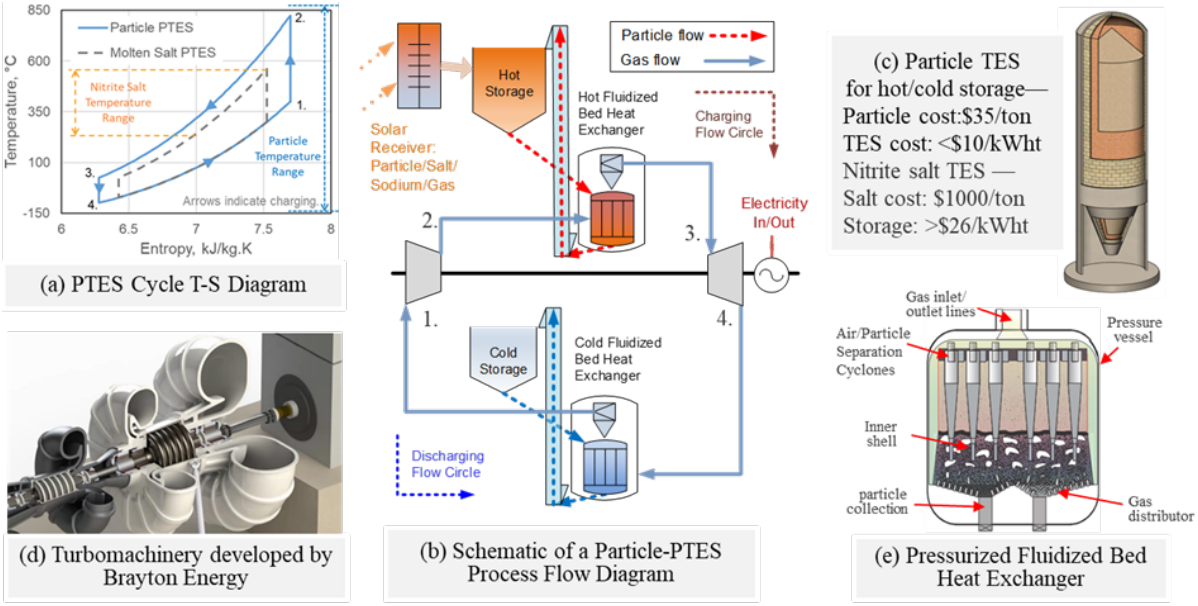

Figure 1. Configuration of a particle PTES system based on an air-Brayton combined cycle for thermal electricity generation

Silica sand particles are stored in unpressurized silos, from which they are transported using skip hoists. To exchange heat with the thermal cycles, the particles then enter a pressurized fluid bed (PFB) HX in which they come directly in contact with working fluid, air, thereby achieving high heat transfer rates. The HXs necessary to transfer energy to/from the turbomachinery working fluid and the hot and cold storage media are critical components that strongly affect the cost and performance of the overall system. The system in Figure 1 incorporates a novel direct-contact air/particle fluid bed rather than a conventional HX design. Prototype HX fabrication and testing in this project demonstrated the design principles and operation of this low-cost, high-performance HX development, which represents a breakthrough technology in a first-of-its-kind high-temperature air/particle direct-contact heat exchange.

The particle-based PTES system has several advantages over other PTES technologies, including:

1. Allowing the use of low-cost particles as cold storage media in place of the costly organic fluids proposed for molten salt PTES (MS-PTES) systems
2. Enabling operation over a larger temperature range, thereby increasing the volumetric energy storage density and eliminating the additional capital costs of a recuperator
3. Facilitating a higher hot storage temperature and thereby a higher discharge efficiency than MS-PTES.

The main objective of the PUMP project was to integrate a particle TES system—using low-cost silica sand as storage media—with a high-performance PTES cycle and hybrid CSP-PTES for grid-scale energy storage. This project included innovative component designs and novel system configurations and was achieved via modeling and testing activities. The PUMP technology development considers both stand-alone PTES for bidirectional grid electricity storage and hybridized CSP with PTES for lower cost, long duration, and high storage efficiency. The project developed comprehensive modeling and experimental tools to de-risk key components, understand expected system performance and operation, and identify feasible component designs and promising system configurations.

The project team produced three journal papers, published in *Solar Energy, Applied Energy,* and *Journal of Energy Resources Technology*, and was awarded a patent in 2023 for an innovative PFB HX design. Numerous conference papers and presentations were prepared for conferences, workshops, and invited talks. Dissemination of the PTES technology development informs the energy storage community about this highly effective energy storage technology that supports reliable energy supply.

Project Activities

The PUMP project consisted of five technology development tasks. These tasks included the design and thermodynamic analysis of subscale and full-scale PTES systems (Task 1); the design, analysis, and prototype testing of critical system components (Tasks 2–4); and the development of a Modelica-based model designed to predict the performance techno-economic analysis (TEA) of a full-scale PUMP system for technology transfer and outreach (TTO) (Task 5). The project focused on designing and, where possible, de-risking critical components through prototype testing.

The project tasks are depicted in Figure 2, which shows the relationships between model development, system and component designs, PFB HX prototype testing, and system integration, including TEA.

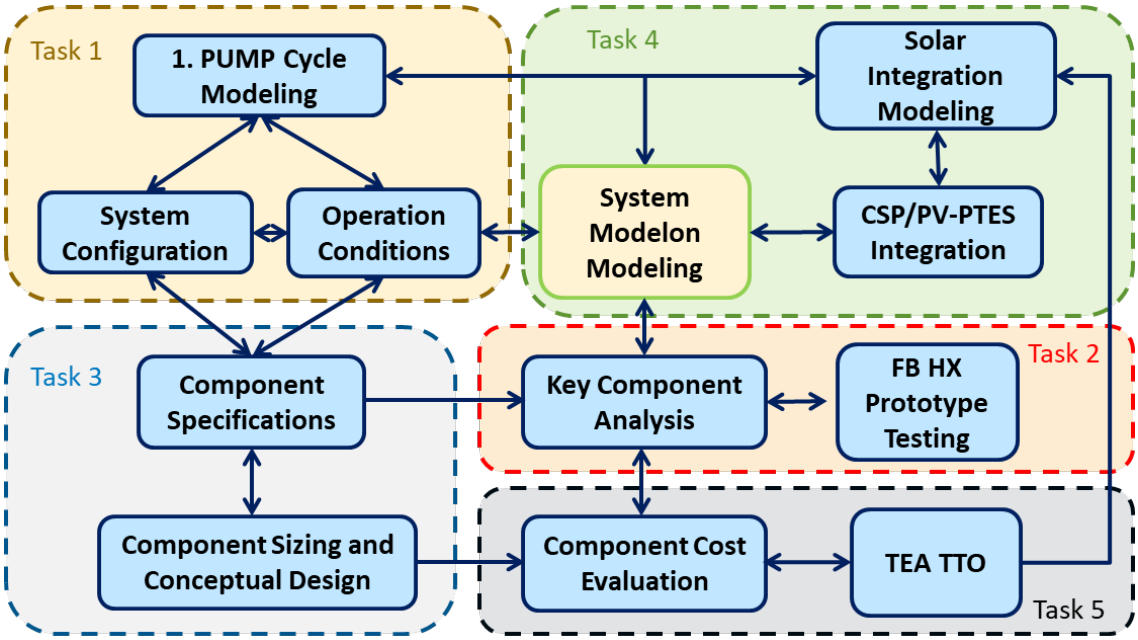

Figure 2. Tasks and key activities of the PUMP project

The project tasks summarized in Figure 2 aimed at addressing key risks in the particle PTES (P-PTES) system to advance the technology and realize its advantages. The early stage of the project identified the technology critical path, component or system-level challenges, and associated project activities, including:

1. Stand-alone or hybrid CSP-PTES system design and operation
    A. Conducted thermodynamic analysis and cycle optimization to select promising operation conditions.
    B. Determined size and cost of key components.
    C. Evaluated CSP operating conditions for hybrid CSP-PTES systems and addressed hot/cold heat storage imbalance.

D. Developed strategies for charging/discharging control of stand-alone PTES and hybrid CSP-PTES systems.

2. PFB HX research and development
    A. Performed computational fluid dynamics (CFD) modeling to understand theoretical performance.
    B. Developed pilot-scale design, sizing, and integrating to prepare for future pilot demonstration of key components.
    C. Conducted lab-scale PFB HX prototype testing to demonstrate feasibility, operation, and a low approach temperature.
    D. Established a commercial-scale design, manufacturing, and cost for system TEA.
3. PTES turbomachinery evaluation
    A. Evaluated options to use or modify turbomachinery at existing CSP plants.
    B. Investigated implications of reversible turbomachinery versus separate turbomachinery on the techno-economic potential of the system.
4. System/component modeling tool development and performance and cost analysis
    A. Developed thermodynamic and cost modeling tools.
    B. Developed a user modeling tool using Modelon-Modelica software to assess the system performance and operation of the PTES and hybrid CSP-PTES systems.

Cost targets for the P-PTES system included capital costs of $650/kW for power-relevant components and $4/kWht for energy storage components. This report documents the outcomes of the PUMP technology development and the activities undertaken to achieve the project goals. The following sections describe the research and development outcomes of major tasks.

1 Task 1: Evaluate PTES Cycle Configurations with Particle TES

In Task 1, we conducted thermodynamic analysis of PTES cycle performance and defined cycle configurations and optimal operating conditions for P-PTES systems. This led to an analysis of the thermodynamic cycle performance and economic benefits of integrating particle TES with PTES and hybridized CSP-PTES cycles. The cycle analysis led to turbomachinery integration, system integration and TEA in subsequent tasks (Tasks 3 and 5).

1.1 Identify PTES Cycle Configurations Suitable for Integration with Particle TES

1.1.1 Overview of P-PTES System and Storage Cycles

Figure 3 shows the overall P-PTES configuration and major components with process flow in (a) charge and (b) discharge processes. The charging phase of a PTES system uses a heat pump cycle, where an electrical work input is used to extract heat from a low-temperature reservoir and upgrade it to higher temperatures, which are delivered to a high-temperature reservoir. A system schematic is presented in Figure 3, and a corresponding exemplary temperature-entropy cycle diagram is shown in Figure 4 in a charge process (Diagram (a) in Figure 3 and Figure 4) and a discharge process (Diagram b in Figure 3 and Figure 4).

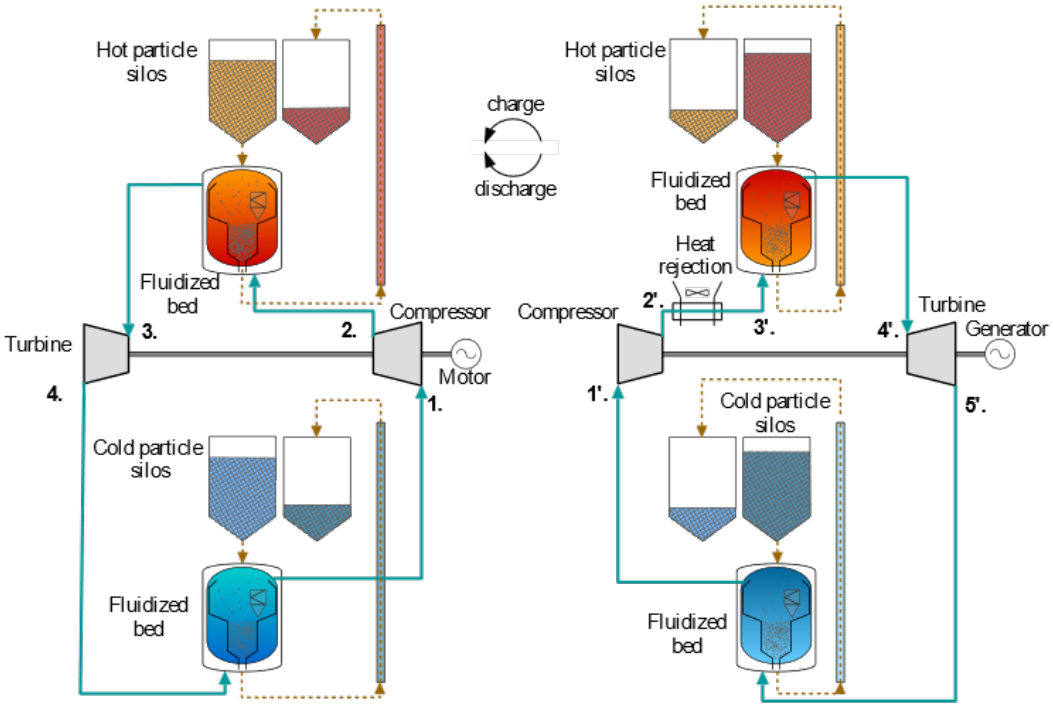

(a) Air and particle flow in a charge process

(b) Air and particle flow in a discharge process

Figure 3. Schematic of the charge and discharge phases of a Joule-Brayton PTES cycle with particle TES

The working fluid (air or nitrogen) is compressed from temperature T_1 to T_2 in the compressor; then, it transfers heat to the particles and is cooled to T_3. The cool, high-pressure gas is expanded in a turbine to sub-ambient temperature T_4 before entering a second HX, where it cools another set of particles that return the gas to temperature T_1. For the storage cycles shown in Figure 4, the "cold" storage particles operate between a sub-ambient temperature (~-45°C) and a hot temperature (~450°C), and the "hot" storage particles operate between an above-ambient temperature (~50°C) and a hot temperature (~800°C).

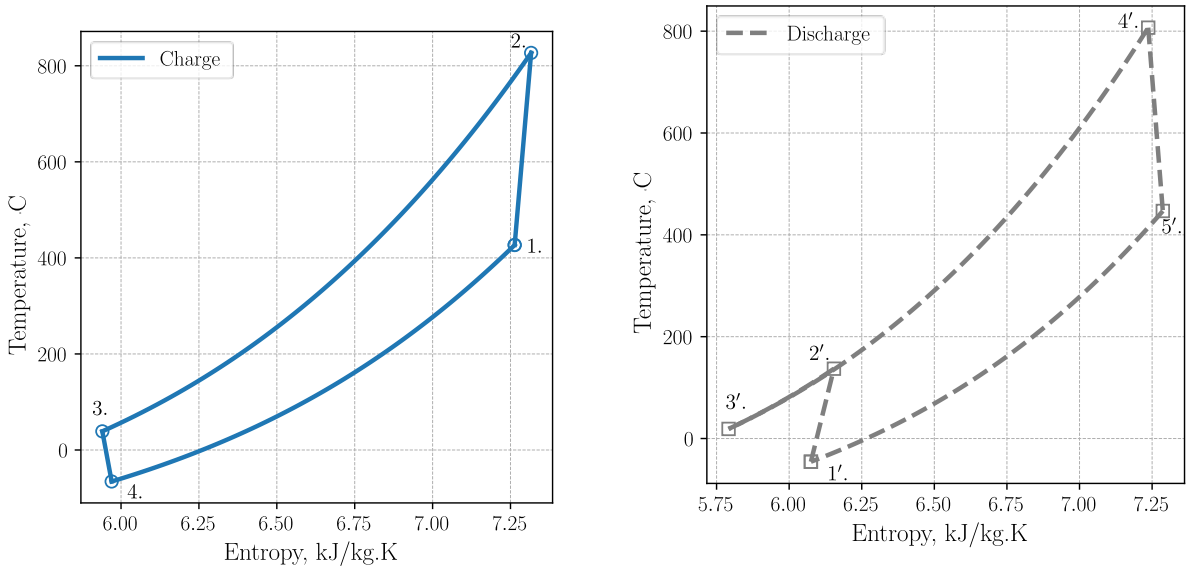

(a) Charging heat pump (b) Discharging heat engine

Figure 4. Temperature-entropy diagram of a nominal PTES system using particle TES. Numbering corresponds to Figure 3.

The discharging phase has a similar operational principle to that of conventional thermal power stations, whereby heat flows from the high-temperature reservoir to the low-temperature reservoir and thus generates an electrical work output. The direction of gas flow is reversed compared to the heat pump. Although the same HXs are used, an additional set of turbomachinery is required. A reversing turbomachinery design is being developed to combine one turbomachinery running for charging and discharging in a reservable mode [2,3]. Reversible turbomachinery was an innovative design that reduces component costs and improves performance, as described in Section 3.

The pressure ratio of the discharging cycle is chosen to ensure that both the hot and cold particles are returned to their original temperatures. As a result, the discharging pressure ratio is larger than the charging pressure ratio [4] . Heat is rejected from the cycle in the discharging phase using an air-cooled HX.

1.1.2 Components, Media, and Operating Ranges of the P-PTES System and a Comparison with MS-PTES Technology

The P-PTES system shown in Figure 3 incorporates particle storage, particle handling, and HXs between the particles and working fluid (which are silica sand and air, respectively) in the current development. Media properties, allowable temperature ranges, and component design

assumptions provide input to the thermodynamic models, selection/optimization of operating conditions, and system performance predictions and are described briefly here.

The storage media are silica particles, which are also being developed for thermal storage in CSP systems [5] and electricity storage systems [6] Previous work found that silica sand produced in the U.S. Midwest has a high SiO_2 purity (>99%). The thermal stability, material compatibility, and physical properties were investigated by testing the sand for 500 hours at 1,200°C with refractory coupon samples present. The sand was also cycled between 300°C and 1,200°C for 100 cycles, and no size change was observed. These results indicate that silica particles are suitable for TES at high temperatures without degradation.

The particles are contained in unpressurized concrete silos that are internally insulated with refractory liners, and the hot storage container was designed and analyzed for use up to 1200°C [7]. P-PTES uses a multiple-container arrangement, in which particles are moved from one particle container to another during charge or discharge. The silos are designed to be tall and narrow, similar to those described in [8]. The system is designed such that there is only one empty silo at a time. Short-duration energy storage (e.g., <10 h) may need a pair of two hot silos and a pair of two cold silos, whereas long-duration energy storage systems to 100-hour discharge duration may have multiple full hot silos with one buffer silo. This helps reduce the cost of energy components as the system scales up.

HXs between silica particles and air use a novel direct-contact fluid bed (FB) working scheme to eliminate interfacial heat transfer surfaces for low cost and high temperature ability. Direct air/particle contact leverages the enormous surface area of particles to transfer heat with air. It can operate above 1,000°C without the material limitations compared to traditional HX relying on heat transfer surface to separate air from particles. In those conventional HX designs beyond 1,000°C, the heat transfer surface area often relies on expensive alloys or ceramic materials to separate two media streams, imposing significant cost and reliability challenges. The use of low-cost sand and conventional insulated concrete silos plus direct-contact FB HXs provides substantial cost and performance advantages to well-developed PTES technology based on molten salt storage, as a comparison is shown below.

Table 1 compares the properties of the silica particles to those of nitrate molten salts and chloride molten salts. The volumetric heat capacity (ρc_p) of silica particles is somewhat lower than nitrate molten salts and a little better than chloride molten salts. When operated over the same temperature range, nitrate molten salts have the highest energy density. However, silica particles can be operated over much larger temperature ranges than molten salts, and as a result, silica particle TES can achieve an energy density that is double that of nitrate molten salts. In addition, particles have a lower material cost per kilogram than molten salts, and this translates to a cost per unit of energy capacity ($/kWh) that is an order of magnitude lower than that of molten salts. (Note that these cost comparisons are based only on the storage media and do not include the cost of the containment).

Particle-based PTES has significant potential for cost and performance and several advantages over MS-PTES, including:

- A wider range of possible operating temperatures for the storage medium (from sub-ambient to >1,000°C), which allows for a larger storage temperature swing and eliminates the expense and exergy penalty of the recuperator required in MS-PTES systems due to a high molten salt freezing point.
- The ability to use the particle media in both cold and hot storage, eliminating the expense and hazards of the organic fluids proposed for cold storage in MS-PTES systems.
- A lower-cost storage medium that can operate at higher storage temperatures, facilitating higher discharge efficiency and round-trip efficiency.

Table 1. Properties and Costs of Molten Salts and Silica Particles, From [4,9]

Parameters	Units	Nitrate Molten Salt	Chloride Molten Salt	Particles
Composition		$NaNO_3$-KNO_3	NaCl-KCl-$MgCl_2$	SiO_2
Particle diameter	m	-	-	0.000625
Minimum temperature	°C	230	450	-
Maximum temperature	°C	565	750	-
Average heat capacity	kJ/kg-K	1.51	1.03	1.15
Density	kg/m^3	1840	1460	2650
Cost	$/kg	0.5–1.3	0.4–1.1	0.03–0.04
Energy density ($\boldsymbol{\Delta T = 300\ K}$)	kWh_{th}/m^3	231	125	148
Energy density ($\boldsymbol{\Delta T = 900\ K}$)	kWh_{th}/m^3	-	-	445
Cost ($\boldsymbol{\Delta T = 300\ K}$)	$/$kWh_{th}$	3.97–10.33	4.66–12.82	0.31–0.42
Cost ($\boldsymbol{\Delta T = 900\ K}$)	$/$kWh_{th}$	-	-	0.10–0.14

The opportunity to incorporate a direct-contact air/particle PFB HX provides cost and performance benefits to particle TES integrated with a PTES system. The direct-contact HX can perform on both cold and hot side of PTES cycles and enable wide temperature range for high storage efficiency and simple operation without the freezing issue of molten salt.

1.1.3 PTES Cycle Thermodynamic Modeling

In this project, a PTES thermodynamic cycle model has been developed to quantitatively compare and optimize the PTES cycle. One measure of PTES performance is the round-trip efficiency, η_{RT}; it is simply defined as the fraction of input electricity that is recovered during discharge:

$$\eta_{RT} = \frac{W_{out}^{dis}}{W_{in}^{chg}} \quad (1)$$

where $W_{\text{in}}^{\text{chg}}$ is the net electrical input to the heat pump during charge and $W_{\text{out}}^{\text{dis}}$ is the net electrical work output during discharge. Another useful metric is the specific work output, w_{out}, given by:

$$w_{\text{out}} = \frac{W_{\text{out}}^{\text{dis}}}{\dot{m}\,\tau_{\text{dis}}} \tag{2}$$

where $\dot{m}$ is the working fluid mass flow rate and τ_{dis} is the discharge duration. The specific work output indicates the power generation per unit mass flow—larger values correspond to a system that will require smaller turbomachines and HXs and therefore reduce costs.

Compressors and turbines are modeled as axial turbomachines characterized by a polytropic efficiency η_p. For a compression process, the infinitesimal specific work input is given by $dw = dp\ /\ (\eta_p \rho)$, which, for perfect gases, leads to:

$$\frac{T_2}{T_1} = \left(\frac{p_2}{p_1}\right)^{\frac{\gamma-1}{\gamma\eta_p}} \tag{3}$$

where T_2/T_1 is the ratio of outlet to inlet temperature, p_2/p_1 is the pressure ratio, and γ stands for polytropic exponent. A similar expression can be found for expansion processes. Although nitrogen is often modeled as an ideal gas, heat capacity variations over the range of operating temperatures do have an appreciable impact on performance and are therefore considered here by integrating Equation 3 over the temperature range of the compressor (or expander) fluid properties from CoolProp software [10].

The compressor and expander are assumed to be on the same shaft and are therefore driven by a motor during charge and drive a generator during discharge. The motor and generator have an efficiency—e.g., the mechanical work into the cycle during charge is less than the electrical work provided to the motor, and a design value of 98.2% is obtained from [11].

The PFB HXs are modeled using an assumed approach temperature and pressure loss. The approach temperature ΔT is the average temperature difference between the gas and the particles. For example, during charge in the hot PFB HX, the gas is at T_2 and is cooled down to T_3, while the hot particles are initially at $T_3 - \Delta T$ and are heated up to $T_2 - \Delta T$. Previous work quantified the model-predicted PFB HX approach temperature to be less than 1°C [12]. Such low values are possible due to the direct contact between gas and particles if a strict air/particle counterflow can be realized in a moving packed bed configuration. The approach temperature is controllable by varying the relative mass flow rates of the air and particles. Additional temperature losses occur when moving particles between the silo and the PFB HX. Simple models indicate that, for insulated skips, these losses are small. The ΔT value includes these losses, and a conservative nominal value of $\Delta T = 10$ K is used. The PFB HX pressure loss is defined in terms of a fractional pressure loss, $f_p = \Delta p / p_{\text{in}}$. Previous work has estimated this pressure loss to be 4% [12].

In a commercial-scale system, particles can be transported between storage silos and a solar receiver or the highest point of the storage tower using a skip hoist. Lifting the particles

consumes power that reduces the overall efficiency. A model of the lifting process was developed, and the lifting power requirement is expressed in terms of the particle mass flow rate $\dot{m}_{\text{particle}}$ and the lifting height H, which is assumed to be 100 m. The lifting power is given by:

$$\dot{W}_{\text{lift}} = 0.0142\, \dot{m}_{\text{particle}} H \tag{4}$$

Efficiency is improved slightly by using two skips: One ascends while the other descends, which allows a degree of energy recovery.

Thermodynamic models of the PTES cycle were developed to assess the cycle performance under various ranges of operating conditions, understand key factors influencing PTES performance, compare the performance of P-PTES to that of MS-PTES, and select optimal system operating conditions. Past analysis indicated that the components with the greatest impact on the system performance are the turbomachinery and the HXs. Other components that must be included in the technical models include motors, generators, heat rejection equipment, and skip hoists. Nominal values of the parameters that govern the performance of these components are shown in Table 2.

Air fans are required to move air through the heat rejection equipment, and the work input to these fans is calculated by considering the fractional pressure drop, f_p, on the air side of the heat rejection equipment. The fans must provide the work to overcome this pressure drop and are governed by an efficiency term η_{fan}. The work input is given by:

$$\dot{W}_{\text{fan}} = \frac{\dot{m}_{\text{air}}\, \Delta p}{\rho\, \eta_{\text{fan}}} \tag{5}$$

where ρ is the density of air. This formulation makes it possible to rapidly evaluate cycle state points. For the charging process, p_1, T_1, and T_2 are specified. Equation 3 is used to find p_2, and the turbine inlet pressure is given by $p_3 = p_2(1 - \Delta p)$. The pressure after the cold PFB HX must equal to the compressor inlet temperature—i.e., $p_1 = p_4(1 - \Delta p)$, from which p_4 is found. The charge turbine pressure ratio is now known, and T_4 is then found. Particle temperatures are calculated using the approach temperatures. For instance, hot particles are heated from $T_{\text{hot},1} = T_3 - \Delta T$ to $T_{\text{hot},2} = T_2 - \Delta T$, whereas cold particles are cooled from $T_{\text{cold},1} = T_1 + \Delta T$ to $T_{\text{cold},2} = T_4 + \Delta T$. The relative mass flow rate of particles to air is given by the ratio of heat capacities. For example, for hot particles:

$$\frac{\dot{m}_{\text{particle}}}{\dot{m}_{WF}} = \frac{c_p(T_2 - T_3)}{c_s\left(T_{\text{hot},2} - T_{\text{hot},1}\right)} = \frac{c_p(T_2 - T_3)}{c_s(T_2 - \Delta T - T_3 + \Delta T)} = \frac{c_p}{c_s} \tag{6}$$

where $\dot{m}_{WF}$ is the mass flow rate of the working fluid (air), c_s is the specific heat of the solid particles, c_p is the specific heat of the working fluid (air) at constant pressure, $\left(T_{\text{hot},2} - T_{\text{hot},1}\right)$ is the change in temperature of the particles, and $(T_2 - T_3)$ is the change in temperature of the working fluid. The particle temperatures at the end of charge are used as the starting point for the discharge cycle. A constraint is imposed that requires the particles to return to their original temperature during discharge, which ensures cyclic operation. This requirement sets several of the discharge cycle state temperatures, because $T_{1,} = T_{\text{cold},2} + \Delta T$, $T_{3,} = T_{\text{hot},1} - \Delta T$, $T_{4,} =$

$T_{\text{hot},2} - \Delta T$, and $T_{5'} = T_{\text{cold},1} + \Delta T$. The minimum pressure, $p_{1'}$, is specified, and the turbine exit pressure is given by $p_{5'} = p_{1'} / (1 - \Delta p)$. Then, the turbine inlet pressure, $p_{4'}$, is calculated. The compressor exit pressure is given by $p_{2'} = p_{4'} / (1 - \Delta p)^2$, which sets the compressor pressure ratio. From this ratio, $T_{2'}$ is found by using Equation 3.

Once the temperatures and pressures around the charge and discharge cycle have been evaluated, the enthalpy and entropy are calculated. From these, the specific work input and output from the compressors and turbines can be found.

The discharging power output $\dot{W}_{out}^{dis}$ is given by:

$$\dot{W}_{out}^{dis} = \dot{m}_{\text{dis}}\left(\dot{w}_{\text{turb}} - \dot{w}_{\text{comp}}\right)\eta_{\text{gen}} - \dot{W}_{\text{fan}} - \dot{W}_{\text{lift,hot}} - \dot{W}_{\text{lift,cold}} \quad (7)$$

while the charging power input $\dot{W}_{in}^{chg}$ is given by:

$$\dot{W}_{in}^{chg} = \dot{m}_{\text{chg}}\left(\dot{w}_{\text{comp}} - \dot{w}_{\text{turb}}\right)/\eta_{\text{motor}} + \dot{W}_{\text{lift,hot}} + \dot{W}_{\text{lift,cold}} \quad (8)$$

In these equations, $\dot{m}_{\text{dis}}\left(\dot{w}_{\text{turb}} - \dot{w}_{\text{comp}}\right)$ is the gross mechanical power generated by the turbine-compressor cycle. This term is multiplied by the generator efficiency η_{gen} to account for electrical conversion losses. The terms $\dot{W}_{\text{fan}}$, $\dot{W}_{\text{lift,hot}}$, and $\dot{W}_{\text{lift,cold}}$ are auxiliary power consumers, representing the power needed to run fans and perform lifting operations. For power output calculations, they are subtracted from the gross generated power, as they are parasitic loads. The term $\dot{m}_{\text{chg}}\left(\dot{w}_{\text{comp}} - \dot{w}_{\text{turb}}\right)$ represents the mechanical power needed to drive the compressor-turbine system. This mechanical power input is divided by the motor efficiency (η_{motor}) to find the electrical power needed to drive it from the grid. The charging and discharging durations are assumed to be equal, $\tau_{chg} = \tau_{dis}$, and the round-trip efficiency is then found from Equation 1, such that $\eta_{RT} = \dot{W}_{out}^{dis} / \dot{W}_{in}^{chg}$. The discharging power output is specified, from which it is possible to calculate the discharging mass flow rate and the particle mass flow rate (from Equation 6). The total mass of particles moved during the discharge process (and therefore stored in the silos) is simply given by $M_{particle} = \dot{m}_{particle}\tau_{dis}$. The particle mass flow rate is equal in charge and discharge, as the particles are operated over the same temperature range and the charge and discharge durations are equal. (Consequently, $\dot{m}_{\text{chg}} = \dot{m}_{\text{dis}}$, as a result of the constant approach temperature, ΔT).

1.1.4 Nominal Design Parameters

A nominal design is chosen for an MS-PTES system and a P-PTES system. These nominal designs give a preliminary indication of the performance and cost and provide a benchmark from which parametric analysis can be conducted. Table 2 provides the design assumptions for the two systems. The nominal MS-PTES design uses nitrate molten salts, as this is the configuration currently being commercialized by Malta Inc. These molten salts are limited to a maximum temperature of 560°C, so the maximum cycle temperature is 570°C. The nominal P-PTES design builds on work conducted for the Advanced Research Projects Agency–Energy (ARPA-E) Duration Addition to Electricity Storage (DAYS) program, in which particle silos and PFB HXs were designed for operation at 1,100 K (827°C) [13]. Results for the nominal designs are provided in Table 3 for systems that deliver 100 MW_e for 10 hours.

Table 2. Nominal Design Inputs Used for Calculations, Unless Otherwise Stated

Parameter	Unit	MS-PTES	P-PTES
Turbomachinery polytropic efficiency	%	90	90
Motor-generator efficiency	%	98.2	98.2
Air fan efficiency	%	75	75
Liquid pump efficiency	%	80	-
Skip hoist power consumption	kW/(kg/s)	-	1.42
HX approach temperature	K	10	10
Heat rejection approach temperature	K	4	4
HX pressure loss	%	2.0	4.0
Heat rejection pressure loss	%	0.5	0.5
Working fluid	-	Nitrogen	Nitrogen
Hot storage fluid	-	$NaNO_3$-KNO_3	Silica particles
Cold storage fluid	-	Methanol	Silica particles
Recuperator	-	Yes	No

Table 3. Techno-Economic Performance of Nominal Designs

Parameter	Units	MS-PTES	P-PTES
Discharge power output	MW_e	100	100
Discharge duration	h	10	10
Charge pressure ratio	-	3.2	4.8
T_1	°C	321	427
T_2	°C	570	827
T_3	°C	330	49
T_4	°C	27	-57
T_5	°C	-48	-
T_6	°C	15	-
Hot storage volume	m^3	30,814	12,811
Cold storage volume	m^3	42,154	12,811
Round-trip efficiency	%	52.3	57.5
Specific work output	kJ/kg	106.7	207.1
Capital cost	M$	365 ± 98	286 ± 63
Power capital cost, $\boldsymbol{C_P}$	$/$kW_e$	3084	2437
Energy capital cost, $\boldsymbol{C_E}$	$/$kWh_e$	54	42
LCOS	$/$kWh_e$	0.175 ± 0.05	0.139 ± 0.03

P-PTES outperforms MS-PTES in terms of the round-trip efficiency, specific work output, capital cost, and levelized cost of storage (LCOS). This is largely due to P-PTES operating at higher maximum temperatures and with a larger pressure ratio. This also leads to P-PTES requiring much smaller storage volumes to provide the same electricity output. Therefore, even though silica particles have a lower volumetric heat capacity than molten salts, their larger operating temperature range leads to higher energy densities. Details of the P-PTES component costs and economic model are described in Section 5. The higher energy density and specific work output of P-PTES lead to reduced capital costs and LCOS compared to MS-PTES, with the LCOS being 20% lower. Although these nominal designs are not directly comparable, they illustrate the potential of P-PTES to improve the cost and efficiency of PTES systems. Parametric studies are conducted in Section 1.2.1 to examine the extent of this improvement.

1.2 Conduct Multi-Objective Cycle Optimization Relative to Cost and Round-Trip Efficiency Over Cycle Configurations

Based on the PTES system configuration, as shown in Figure 3, and the modeling methods and conditions shown above, we have performed parametric analysis on operation parameters to understand their effects on PTES cycle performance and subsequently determine optimum component design and operation conditions. The nominal designs defined in Table 2 are used as a baseline to investigate the impact of key design parameters, such as the charge pressure ratio, HX approach temperature, pressure loss, and maximum temperature. Results are calculated for several maximum temperatures. A MS-PTES system is evaluated at 570°C and 760°C, which correspond to using nitrate molten salts and chloride molten salts, respectively. A P-PTES system is evaluated at these temperatures to enable a direct comparison. P-PTES systems operated at higher temperatures (827°C and 1,027°C) were also analyzed, since silica particles are stable at those temperatures.

1.2.1 Turbine/Compressor Pressure Ratio

The maximum cycle temperature is kept constant, while the charge pressure ratio varies, this corresponds to varying the charge compressor inlet temperature. Figure 5 indicates that at the same maximum temperature, MS-PTES has higher η_{RT} and w_{out} than P-PTES. This may be understood by carefully considering the discharge turbine temperature ratio. The cycles are constrained by the requirement that the storage materials are returned to their original temperature at the end of discharge. For P-PTES, this constraint on the cold particles means that the discharge turbine exit temperature T_{TET} must be $T_{\text{TET}} = T_1 + 2\Delta T$. However, for MS-PTES, the discharge turbine exit temperature is constrained by the hot storage fluid due to the recuperator, which leads to $T_{\text{TET}} = T_1 + \Delta T$. In both cases, the discharge turbine inlet temperature is $T_{\text{TIT}} = T_2 - \Delta T$. As a result, for the same maximum temperature and pressure ratio, MS-PTES has a larger discharge power output due to the larger turbine temperature ratio. Similar effects are observed in the discharge compressor. Although MS-PTES outperforms P-PTES when both are evaluated at the same maximum temperatures, silica particles can be operated at higher temperatures than molten salts. Figure 5 shows that higher-temperature P-PTES designs have higher η_{RT} and w_{out} than MS-PTES.

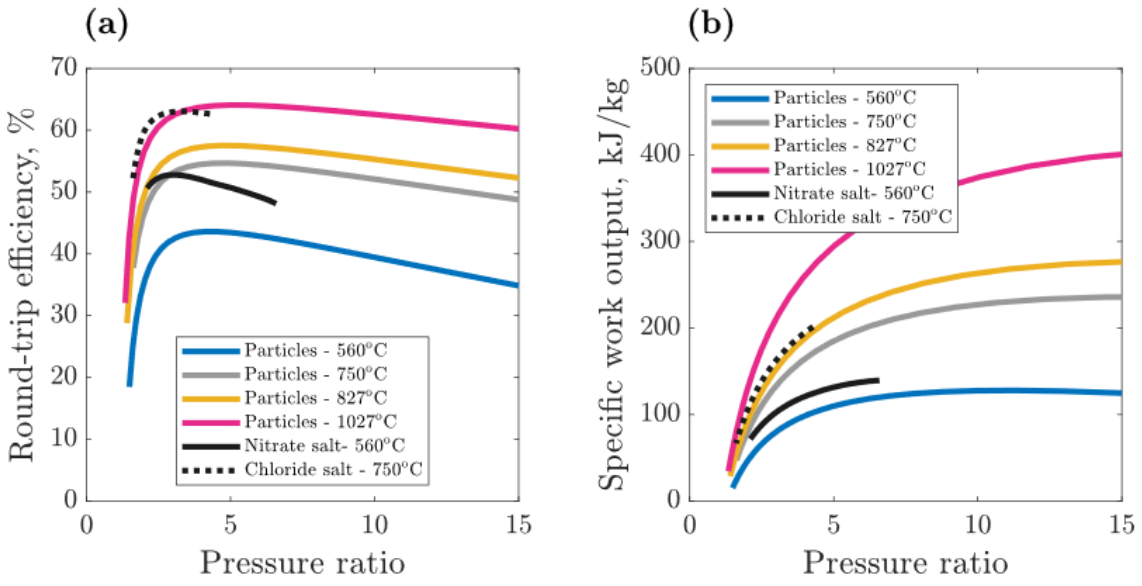

Figure 5. Influence of pressure ratio on round-trip efficiency and specific power output

Similar results are seen for capital costs and LCOS in Figure 6: For the same maximum temperature, nitrate salt MS-PTES outperforms P-PTES because it has better efficiency. Chloride salt MS-PTES has higher capital costs and therefore does not outperform P-PTES at the same maximum temperature.

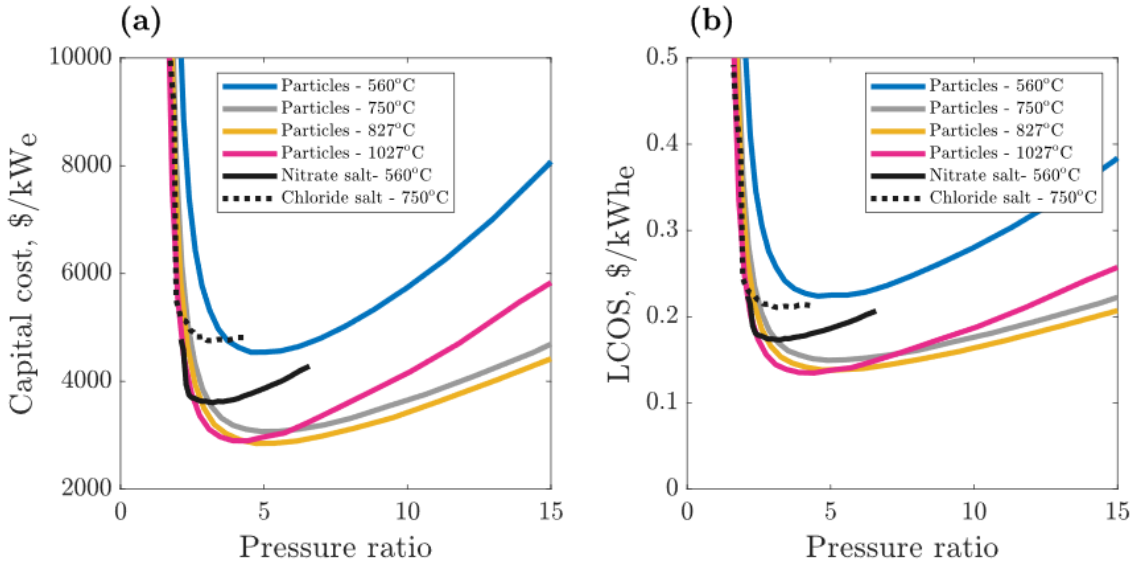

Figure 6. Influence of pressure ratio on capital cost and LCOS

P-PTES can achieve lower costs than all MS-PTES systems when operated at higher temperatures. There appear to be diminishing returns when increasing the temperature, which is explored in more detail in Task 4 (Section 4). The chloride molten salt system has higher costs than the nitrate molten salt system as a result of having to use nickel alloys in the hot HX and recuperator [4]. Costs rapidly increase as the pressure ratio drops, particularly for chloride MS-

PTES, because lower pressure ratios lead to higher temperatures in the recuperator, which then requires nickel alloys above 600°C [4].

In each MS-PTES and P-PTES system, an optimal pressure ratio exists that maximizes η_{RT} and minimizes cost and LCOS. This optimal point occurs due to a trade-off between exergy losses in the HXs (low pressure ratio) and in the turbomachinery (high pressure ratio); see Figure 7. This can be explained in terms of work ratio and heat-to-work ratio [14]. The work ratio is the ratio of charge compression work to expansion work, whereas the heat-to-work ratio is the total heat transferred divided by the charge work input. At high pressure ratios (when the maximum cycle temperature is fixed), the cycle has a lower work ratio, which corresponds to the efficiency being more sensitive to the turbomachinery efficiency. Therefore, exergy losses are increased in the turbomachinery at high pressure ratios. On the other hand, low pressure ratios lead to larger heat-to-work ratios, which correspond to a large quantity of heat being transferred for a given work input. Therefore, at low pressure ratios, the performance of HXs is more important and exergy losses in HXs are more significant.

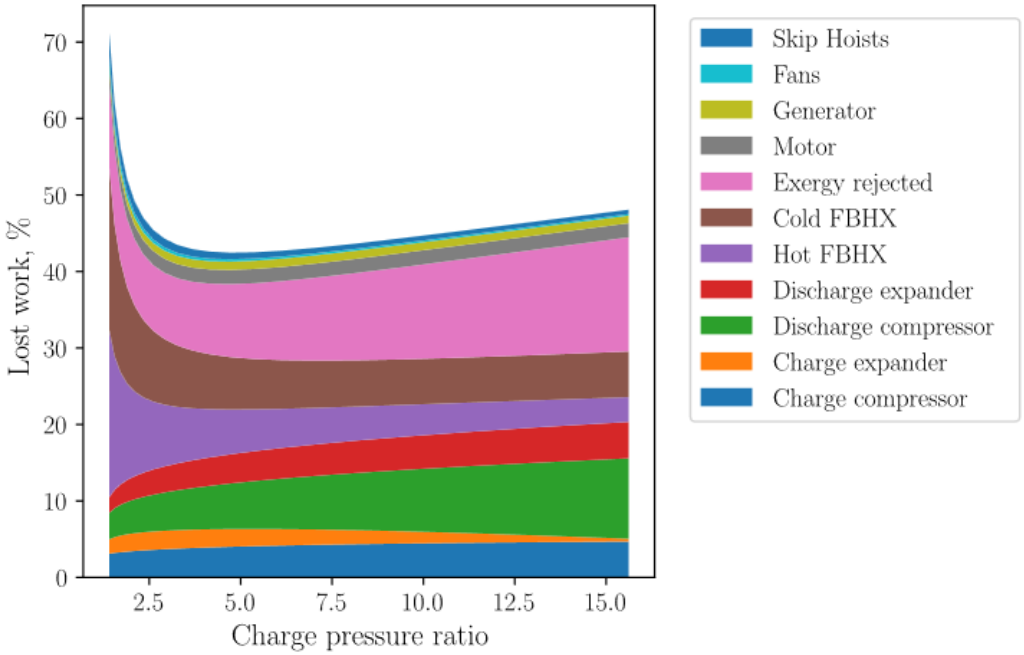

Figure 7. Distribution of exergy losses in P-PTES as a function of pressure ratio

For each maximum temperature, the pressure ratio that minimizes the LCOS is chosen as the nominal point for further parametric studies. For MS-PTES at 570°C and P-PTES at 827°C, these values correspond to those shown in Table 3. As the maximum temperature increases, the optimal pressure ratio decreases slightly.

1.2.2 Heat Exchanger Approach Temperature

PTES cost and performance depend critically on the HX design and effectiveness. Here, HX performance is quantified in terms of pressure loss and approach temperature, which is the temperature difference between the working fluid and the particles or storage fluid. In this report, the approach temperature is defined as the average temperature difference over the length of the HX. The approach temperature ΔT is an input to the P-PTES model described above, but the

MS-PTES model requires the effectiveness ε to be defined instead. The effectiveness of each HX is varied iteratively until the required ΔT is achieved. Figure 8 and Figure 9 show results for several maximum temperatures.

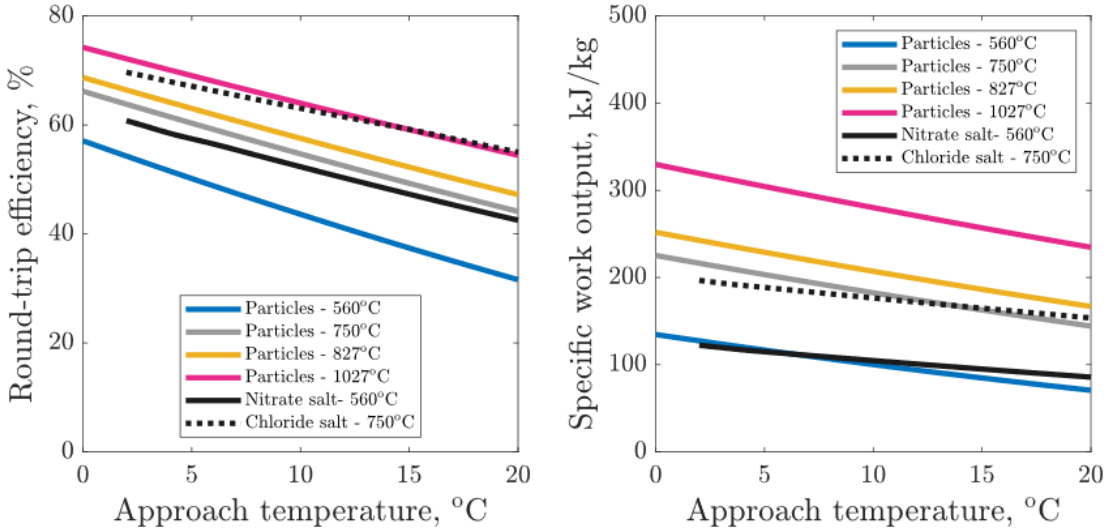

Figure 8. Influence of HX approach temperature on round-trip efficiency and specific power output

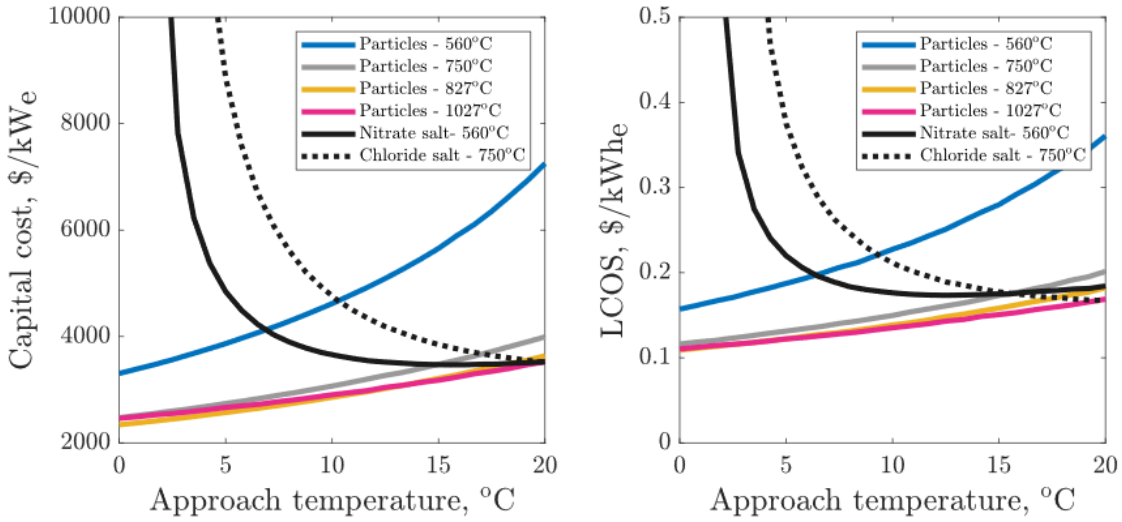

Figure 9. Influence of HX approach temperature on capital cost and LCOS

The round-trip efficiency and specific work decrease linearly as ΔT is increased. The gradient of the P-PTES curves is slightly steeper than that of the MS-PTES curves, indicating that P-PTES is more sensitive to variations in ΔT. MS-PTES costs increase rapidly as ΔT is reduced because a high effectiveness requires large metal surface areas, which lead to high costs. The results in [4] suggest that costs begin to escalate rapidly when $\varepsilon > 95\%$, while Figure 8 shows that this happens when $\Delta T < 10$ K for nitrate molten salt systems. (Note that $\Delta T = 10$ K is equivalent to a hot HX with $\varepsilon = 0.96$, so these results are in agreement.) On the other hand, P-PTES costs decrease as ΔT is reduced because of the direct-contact heat transfer in the PFB HX. Lower

approach temperatures are achieved by controlling the relative flow rates of the particles and working fluid, and a CFD study in [12] indicated that $\Delta T < 1$ K is possible. Therefore, low ΔT is achieved without requiring additional capital expenditure.

For P-PTES systems, there does not appear to be an economic benefit to increasing the maximum temperature beyond 750°C once ΔT is sufficiently low—e.g., $\Delta T < 5$ K. This is due to increased turbomachinery costs, as explored in Section 3.

1.2.3 Heat Exchanger Pressure Loss

The influence of pressure losses in the HXs is illustrated in Figure 10 and Figure 11.

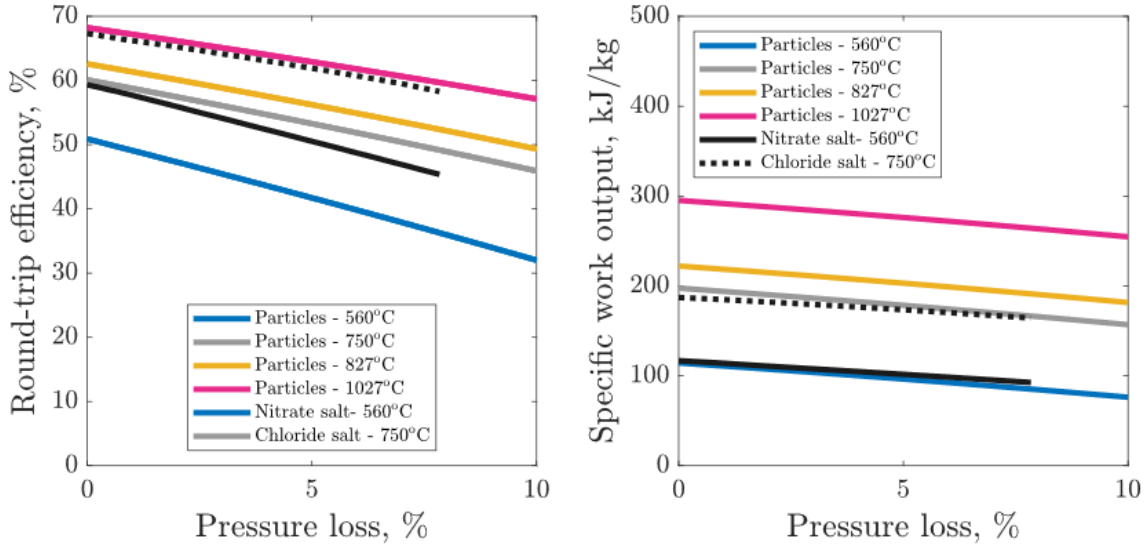

Figure 10. Influence of HX pressure loss on round-trip efficiency and specific power output

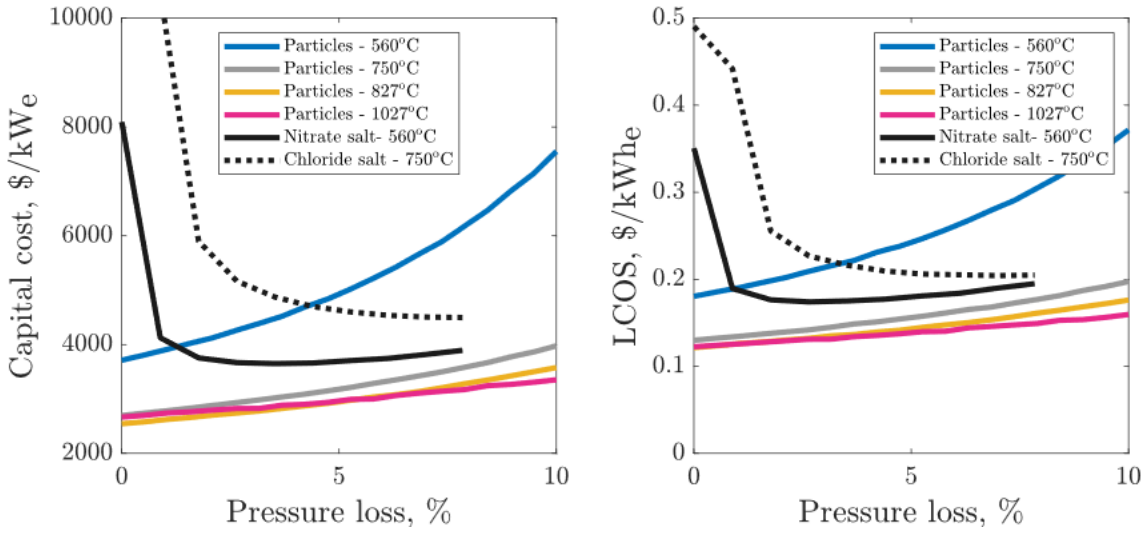

Figure 11. Influence of HX pressure loss on capital cost and LCOS

For P-PTES systems, the hot and cold PFB HX have an equal pressure loss that is equal to the value shown on the x-axis. For MS-PTES, the total pressure loss through the hot HX and high-pressure recuperator is equal to the value on the x-axis (and is also equal to the pressure loss in the cold HX and low-pressure recuperator). This ensures the two systems have equivalent pressure losses between the compressor outlet and turbine inlet, and between the turbine outlet and compressor inlet, during charge.

Trends in these results are similar to those for the approach temperatures. The η_{RT} and w_{out} increase nearly linearly as the fractional pressure loss f_p drops. P-PTES cost and LCOS decrease for low values of f_p, while MS-PTES costs increase rapidly—again due to the HX size increasing to facilitate lower pressure losses. For PFB HXs, lower pressure losses can be achieved by adjusting the aspect ratio of the FB, which does not have a strong impact on the capital cost.

1.2.4 P-PTES Maximum Heating Temperature

Parametric studies in Section 1.2.1 indicate that there are limited economic benefits to increasing the P-PTES maximum temperature beyond 800°C. Figure 12(a) demonstrates how the LCOS depends on the maximum temperature for two approach temperatures. For each maximum temperature, results are shown for the optimal pressure ratio that minimizes the LCOS. Figure 12(a) indicates that there is a maximum temperature that minimizes LCOS. Increasing the maximum temperature improves η_{RT} and w_{out}, which helps reduce capital costs by reducing the size of the turbomachinery and HXs. However, some of the compressor cost correlations include temperature dependence because material selection and fabrication difficulties increase with parts operating temperatures. High charge compressor exit temperatures are likely to increase the cost, especially if blade cooling is required. Therefore, at high temperatures, capital cost increases. This is reflected in the capital cost distribution chart shown in Figure 12(b): The cost of most components drops as the maximum temperature increases. However, the charge turbomachinery cost increases rapidly once the temperature exceeds 800°C, when the approach temperature is 10°C. Figure 12(a) indicates that the optimal maximum temperature increases as the approach temperature reduces.

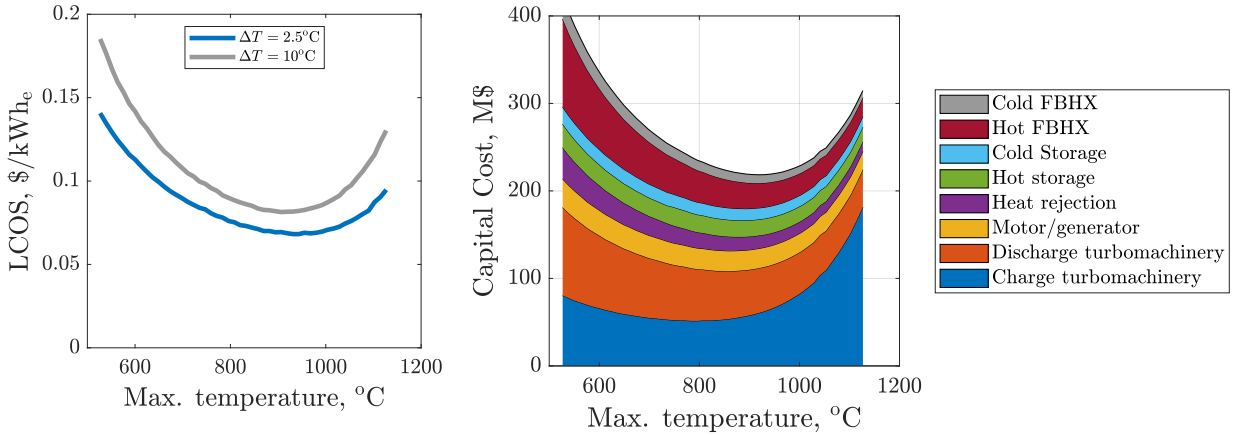

(a) LCOS for two approach temperatures

(b) Distribution of capital costs for P-PTES for an approach temperature of 10 K

Figure 12. Influence of P-PTES maximum temperature

In summary, Task 1 has developed system configurations and correspondent modeling tools for PTES thermodynamic cycle analysis. The P-PTES system can achieve high temperature (>1,000°C) using particle-based TES for high efficiency (>55%) and long duration energy storage (>10 hours). Comparison with current molten-salt PTES technology shows the motivation to develop particle PTES and hybrid CSP-PTES to overcome certain issues of molten salt PTES with no high/low temperature limitations of molten salt storage. With the verification of cycle performance and system feasibility, the development focuses on enabling high-temperature components and testing to demonstrate a particle heat exchanger.

2 Task 2: PFB HX Design, Modeling, and Laboratory-Scale Testing

Task 2 focused on the development of the air/particle direct-contact PFB HX, a key component in the system. As shown in Section 1, the HX performance and cost have significant impacts on the system technical and economic performance, and the ability of the PFB HX to avoid expensive heat transfer interfaces and achieve low approach temperatures is a key enabling feature for the economic feasibility of the P-PTES system.

2.1 Product-Scale System Layout and PFB HX Concept

We have completed the conceptual design of a commercial-scale P-PTES system using particle TES for both hot and cold energy storage. The system was designed with a 50-MW_e discharge capacity and 100 hours of storage. The commercial-scale PFB HX concept was originally developed in a prior project (Economic Long-Duration Electricity Storage by Using Low-Cost Thermal Energy Storage and High-Efficiency Power Cycle [ENDURING]) [13], funded by the ARPA-E DAYS program. The preliminary concept from the ENDURING project was adopted and refined in the PUMP project for the advanced PTES system. Table 4 shows the operating conditions based on the turbomachinery capacities provided by Brayton Energy, which were used to design the 50-MW_e system. Figure 13 illustrates process flow diagrams for the 50-MW_e system in its charging process (Figure 13(a)) and discharging process (Figure 13(b)). Charging and discharging processes on the cold and hot sides can be realized by only one set of PFB HXs and particle dispensing lock hoppers.

Table 4. Process Operating Conditions From Brayton Energy

Parameters	Units	Values
Air mass flow rate at charging and discharging	kg/s	297.6
Hot storage T range	°C	88.85 –826.85
Cold storage T range	°C	-41.15 – 554.85
Pressure at turbine inlet	MPa	1.46
Pressure at compressor outlet	MPa	1.50
Pressure at compressor inlet	MPa	0.50
Approach temperature in PFB HX	°C	15

In the charging process, low-temperature particles are discharged from the hot side silo and transported to the top of the lock hopper by a particle conveyor. The lock hopper is divided into two separate chambers that operate alternately to enable continuous particle flow through the PFB HX. The particles from the silo fill one side of the lock hopper, while the other side (already filled with particles) is at balanced pressure with the PFB HX. Low-temperature particles enter the PFB HX from the pressurized side of the lock hopper and are heated up by the hot air from the high-temperature turbomachinery (working as a compressor). High-temperature particles are then transported back through a skip hoist to fill the hot side silo to complete the hot side charging process. The low-temperature air from the hot side PFB HX goes to the low-temperature turbomachinery (working as a turbine) to expand to reach the low temperature of the

cold side. Warm particles from the cold side silo are cooled by cold air in the cold side PFB HX and are transported back to cold silos to complete the cold side charging process. In the discharging process, the hot side silos are full of high-temperature particles and the cold side silos are full of low-temperature particles at the initial stage. The particle levels in the PFB HX during charging versus discharging processes are different in both the hot and cold sides so that the PFB HX can perform in an opposite way.

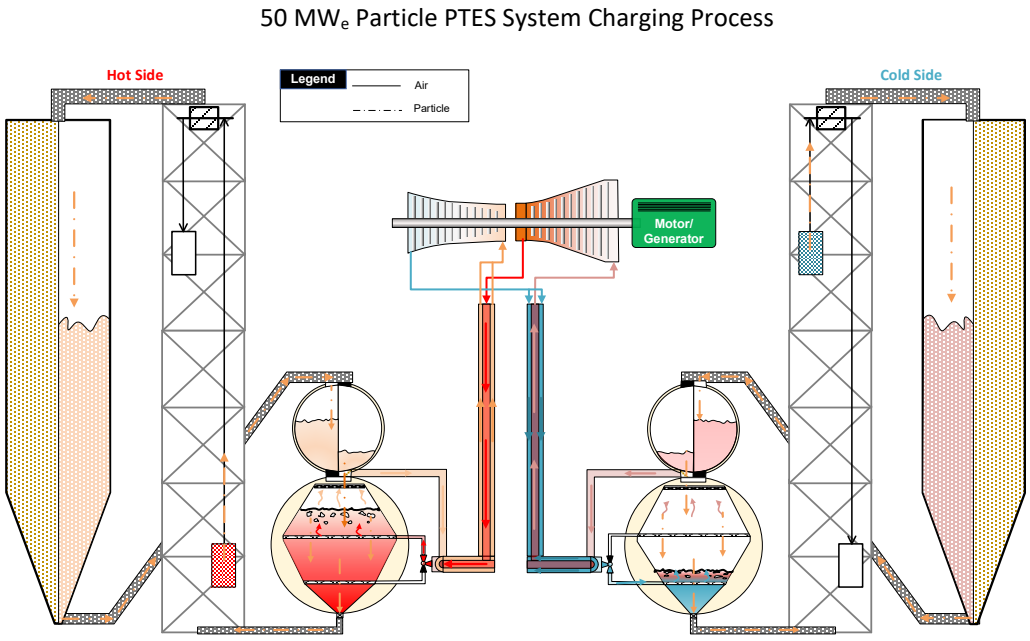

(a) System diagram and components of 50-MW_e P-PTES charging process

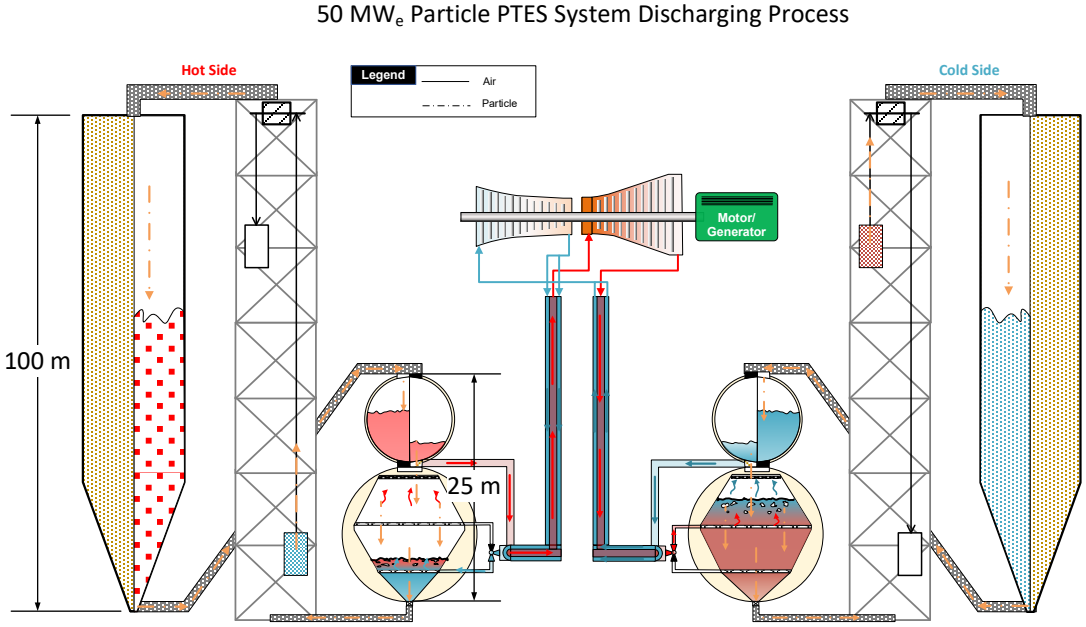

(b) System diagram and components of 50-MW_e P-PTES discharging process

Figure 13. System configuration for a 50-MW_e system with 100 hours of storage capacity in charging and discharging processes

Table 5 shows the overall design results, including the system thermal performance and air pressure drops derived from the power cycle from Brayton's turbomachinery. The cold side discharging process energy "loss" is energy gained from the ambient, as the low-end temperature at the cold side is much lower than the ambient temperature. The heating of the cold side results in reduced power cycle efficiency due to a smaller temperature difference between the hot and cold storage. The insulation designs of all components perform as expected, and the energy loss per day is less than 2% of the total energy exchanged during the operation.

Table 5. Overall System Design Specifications

Parameters	Units	Hot Side	Cold Side
Power plant capacity	MW_e	50	
Storage hours	hours	100	
Air mass flow rate	kg/s	296.7	
Particle mass flow rate	kg/s	296.12	284.96
TES capacity	GWh_{th}	25.29	19.62
Total thermal energy stored	GJ	91025	70727
Total heat loss during discharging to ambient	kW	5035.81	289.77 (Gain)
Total discharging gas side pressure drop	kPa	29.25	28.28
Total discharging heat loss percentage	%	2.00	0.15
Total heat loss during charging to ambient	kW	466.81	3504.08
Total charging gas side pressure drop	kPa	34.86	26.02
Total charging heat loss percentage	%	0.18	1.79
Total designed system height	m	100	

Figure 14 shows the concept PFB HX for direct-contact air/particle heat transfer. The PFB HX can support high effectiveness with air/particle direct-contact heat transfer for high-temperature operation without interfacial materials between air and particles.

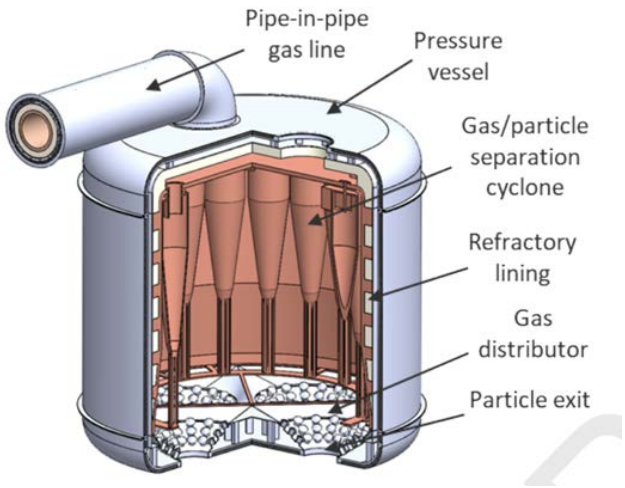

Figure 14. Conceptual design of an FB HX, from [6]

The HX is contained inside a pressurized vessel in which particles are fluid by the working fluid, as illustrated in Figure 14, where an outer shell is designed to withstand high pressures, while the actual HX is contained within an inner shell. The pressure vessel contains compressed air. The air flow is directly integrated with the compressor and turbine through a tube-in-tube connection. The exit air from a PFB HX flows through an array of air/particle separation cyclones inside the pressure vessel to remove any entrained particles. The PFB HX achieves high effectiveness without the large metal surface areas of conventional shell-and-tube HXs due to turbulent mixing processes and direct-contact heat exchange.

2.2 Development of Laboratory-Scale PFB HX Test Station

A prototype PFB HX was designed, built, and tested to demonstrate the HX operation and performance. The prototype HX was designed and operates near ambient pressure without the need of pressure vessel; thus, it is referred to as a FB HX in the sections that follow. The design approach is analogous to the configuration of PFB combustion boilers.

2.2.1 Test Station and Prototype FB HX Design

The prototype FB HX is part of a closed particle loop, as shown in Figure 15. The solid particles are held in a storage vessel above the FB HX. The particles are gravitationally fed into the FB HX by a nonmechanical L-valve. The particles have a net downward flow through the FB HX while exchanging heat with the fluidizing air flowing upward. At the bottom of the FB HX, particles are removed by a screw conveyor, balancing the particle mass flow inlet from the L-valve and ensuring a constant particle mass inside the FB HX and a constant bed height. The screw conveyor moves the particles to a pneumatic conveying line, where they are entrained in air (separate from the fluidizing air) and returned to the storage vessel. Details on the particle conveyance and system loop are presented by Jeong [15]. Air-particle separator cyclones are used to minimize particle losses through the air exhaust ports. There is no cooling system in this lab-scale prototype, nor different hot and cold storage vessels; thus, the test run is limited by the quantity of particles in the system, the mass flow rate of particles through the FB HX, and the rate of natural cooling. In addition, this system does not contain intercoolers or separate hot and cold storage vessels—it was built specifically to test the FB HX technology, not to demonstrate a whole PTES system.

The FB HX test station was designed to test hot air, cold particle operation (i.e., the air is being used to heat the particles). Prior work as part of the ENDURING project focused solely on the opposite heat transfer direction and only included a closed particle system (i.e., no particle inlets or outlets). Hot air, cold particle operation is analogous to the HX that transfers heat from the hot air to the particles during the charging process in the P-PTES system driven by low-cost off-peak electricity. Reverse operation of the FB HX when hot particles heat up compressed air is corresponding to a discharge process of stored thermal energy to drive turbine for electric generation back to the grid.

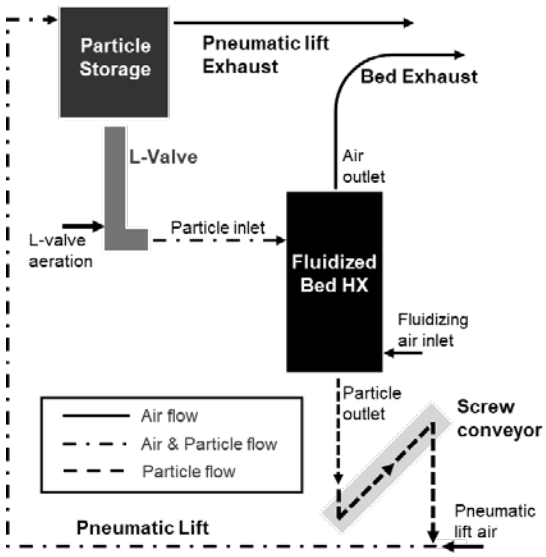

Figure 15. Schematic of FB HX test bed showing particles and air flows

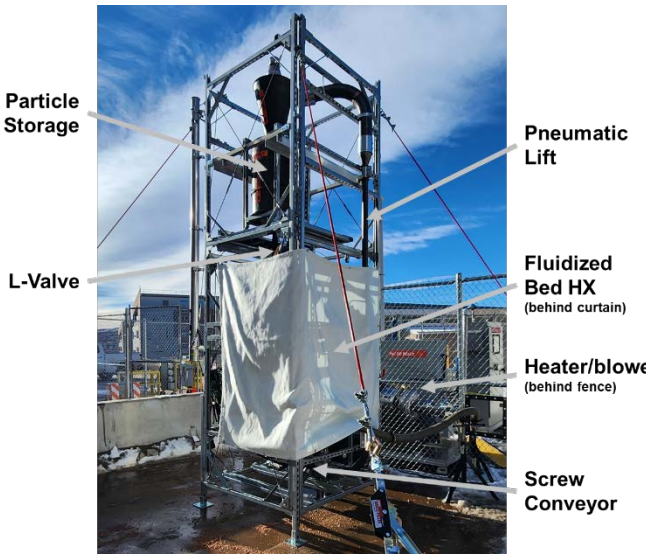

Figure 16. FB HX test stand during test

The hot air for fluidization is provided by a 60-kW electric heater and blower system: a skid-mounted MHI Airtorch and Republic Manufacturing 1202 centrifugal blower. The air flow rate and thus the fluidizing behavior of the bed is controlled by this heater and blower system with a separate control system. This heater/blower skid is a laboratory asset, appropriately named Hot Air Testing Station (HATS), that is available at the NLR Energy Systems Integration Facility for future use. Hence, its control system and data acquisition (DAQ) are separate from those of the PUMP PFB HX.

The HATS outputs to a 2-in. American Society of Mechanical Engineers (ASME) B16.5 Class 150 flange, which is connected to the FB HX via a 10-ft flexible stainless-steel hose (McMaster-Carr 5793K68). Thus, the measurement of flow rate from the blower is separated from the FB HX by this distance (it takes approximately 1.2 seconds for the air to traverse through the hose to the FB HX). The HATS is controlled in increments of standard cubic feet per minute (SCFM) of air. This unit will be used in the description of the test results and discussion of data. This HATS system has a lower limit air flow rate of 20 SCFM (0.0116 kg/s); however, the practical lower limit is 22 SCFM (0.0127 kg/s) to protect the heater from interlocks that shut off the equipment if the flow rate inadvertently drops below 20 SCFM (0.0116 kg/s) due to fluctuations in the air flow from pressure perturbations in the FB HX.

The experimental setup shown in Figure 16 was built and contained within a steel structure built from Unistrut. The structure is approximately 4-ft square with a height of nearly 15 ft. Forklift pockets were installed at the bottom of this structure for easy transportation from the inside high bay storage to the outside testing area. It was necessary to store the structure inside when not in use; it was not built to be weather-rated (rain and wind, specifically), did not have permanent anchored support, and could not be operated inside the building due to safety concerns, interference with other research and development projects in the shared lab space, and unwanted noise level. We recommend that future laboratory endeavors of a PFB HX design be operated in

place to avoid the hassle of moving, setup, and teardown at the beginning and end of each testing day.

The FB HX vessel was fabricated out of 11-gauge stainless steel 304. The vessel has the same internal dimensions as 12-in diameter with flanges matching the ASME B16.5 Class 150 flange dimensions. The air distributor was fabricated out of 11-gauge stainless steel 304 and is affixed to the lower hopper section of the FB HX via the matching flanges. A graphite gasket seals this connection. A cutaway view of the FB HX with the air distributor CAD model is shown in Figure 17(a), with the fabricated version shown in Figure 17(b).

Details on the air distributor operation and fundamental principles are presented by . The air distributor consists of a central manifold that passes through the vessel wall to mate with the heater/blower via a 2-in. ASME B16.5 Class 150 stainless steel flange.

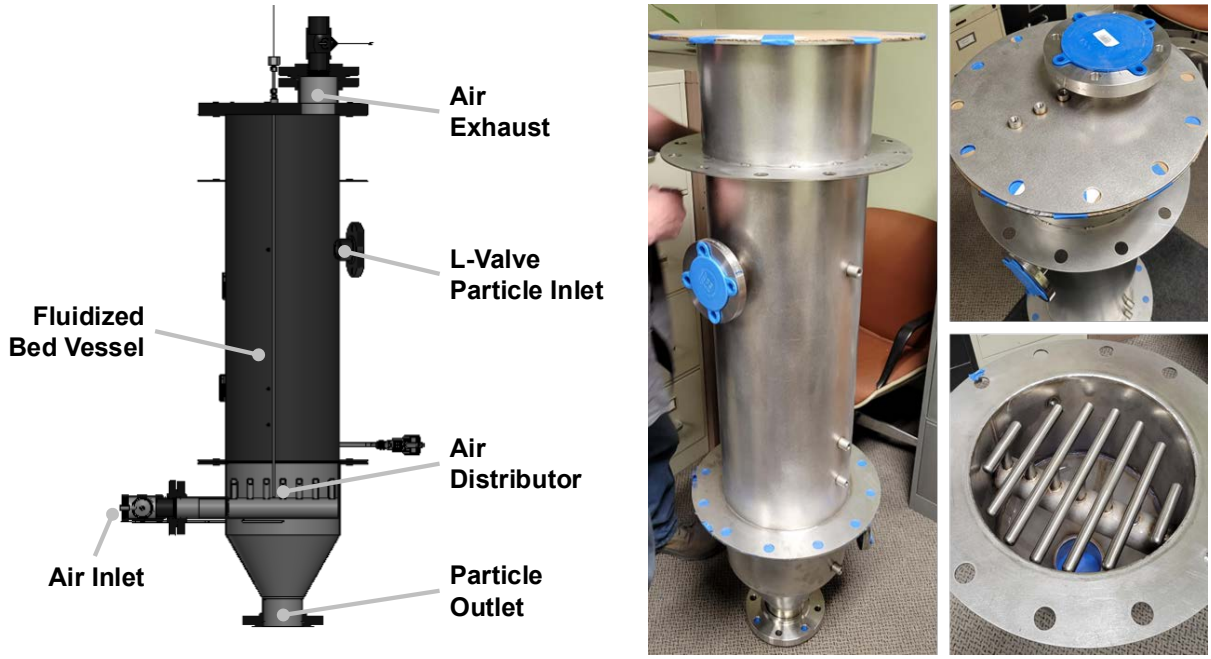

(a) CAD model of air/particle direct-contact HX design

(b) Fabricated parts for air/particle HX

Figure 17. Development of the prototype FB HX

Inside the FB HX, the manifold branches into seven fingers that roughly contour to the circular shape of the FB HX vessel, with aeration holes facing downward, 30° from vertical. The particle bed sits above the air distributor, and particles flow downward between the fingers. These downward holes prevent particles from clogging the aeration nozzles and disrupting the air flow. The air initially flows downward, but the mass of particles beneath the air distributor in the hopper blocks the air flow and results in the air flowing upward through the bed, fluidizing it, and exiting the exhaust pipe to the air/particle separation cyclone. The hopper beneath the air distributor is angled 30° from vertical, terminating in a 4-in ASME B16.5 Class 150 flange.

Above the air distributor is the main body of the FB HX. Three pressure transducers (Setra 230) measure the pressure at varying intervals upward in the bed; see Figure 18. These pressure

transducers can be used to estimate the bed height when air flow is supplied. The L-valve injects the particles into the bed at a height of 0.6 m above the air distributor. This is also the maximum bed height achievable—L-valves are self-locking; thus, when the bed height reaches this point, no additional particles can flow into the bed.

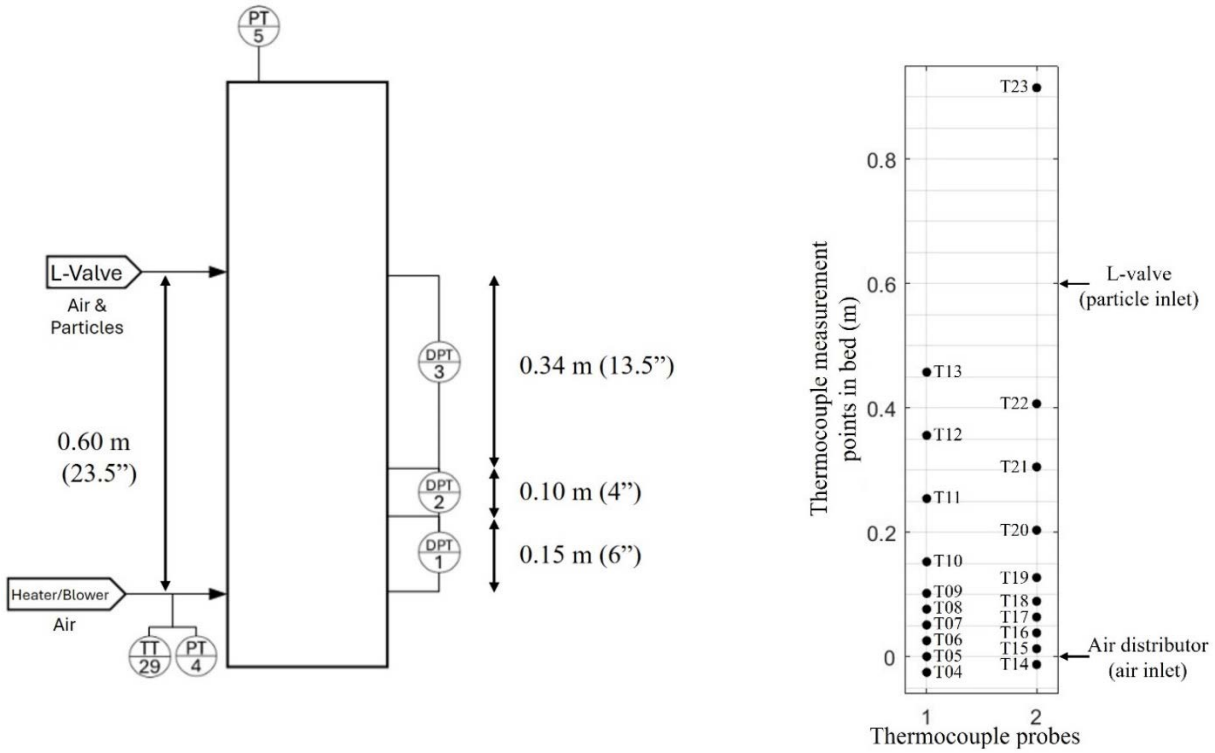

(a) Measurement points for pressure transducers

(b) Thermocouple immersed in the particle bed. Two vertical probes each contain 10 measurements.

Figure 18. Dimensions of the differential pressure transducer in the FB HX prototype

Two thermocouple probes extend from the top cover flange of the bed into the FB HX to measure the vertical temperature profile in the bed. Each thermocouple contains 10 measurement points, which are mapped in Figure 18. Vertically through the bed, the measurement points alternate between the two probes due to limitations on the minimum spacing for each probe. The measurement points record an average of the air-particle temperature at this location in the bed and serve as the basis for analyzing the thermal behavior within the bed.

The solid particles used in this FB HX demonstration are silica sand. The sand is Granusil W4095, procured from Black Lab (a subsidiary of Covia Inc.), with a reported average diameter of D_p = 625 µm, which belongs in Geldart Group B. The target net particle flow rate for operating this FB HX is between 0.02 kg/s and 0.05 kg/s, depending on the fluidization conditions and HX performance data desired. Thus, all equipment must be capable of conveying this particle rate for different experimental conditions. Furthermore, to stabilize the FB height and HX performance, the screw conveyor and L-valve must be independently controllable during test. Larger FB HXs will require higher particle flow rates and thus may require more particle handling systems or many smaller systems working in parallel.

2.2.1.1 Air Distributor Design and Fabrication

The air distributor used in the FB HX consists of laterally flowing spargers, which have several advantages: minimized particle grid leakage, good operational range, low pressure loss, safe thermal elongation, easy air hole cuts, tiered fluid injection, and better particle movement. The air distributor was designed based on the design guidelines for uniform air distribution and to provide the desired fluidization conditions presented previously. Manifold and header diameters were designed to avoid maldistribution of air by:

$$\left(\frac{D_{\mathrm{m}}^2}{N_{\mathrm{h}} D_{\mathrm{h}}^2}\right) > 5 \tag{9}$$

$$\left(\frac{D_{\mathrm{head}}^2}{N_{\mathrm{m}} D_{\mathrm{m}}^2}\right) > 5 \tag{10}$$

where D_{m} is the diameter of the manifold, D_{head} is the diameter of the header, N_{h} is the number of holes, and N_{m} is the number of manifolds. In designing the air distributor geometry and hole size, pressure drops of air flow over the lengths of the in manifolds are less than $0.1\Delta P_{\mathrm{grid}}$ to provide even air flow across the grid holes. The length of header is also considered a pressure drop in the header, which is less than 0.1 of pressure drops in manifolds for the same reason. The determined design parameters for the air distributor are presented in Table 6. The design and the fabricated air distributor are shown in Figure 19.

The relationship of ΔP_{grid} and U_{h} as a function of $\dot{m}_{\mathrm{air}}$ was used to design the air distributor. U_{h} showed a linear increase as $\dot{m}_{\mathrm{air}}$ increased. High U_{h} can result in strong air jets to the FB with undesirable fluidization conditions, but laterally facing holes can reduce this effect.

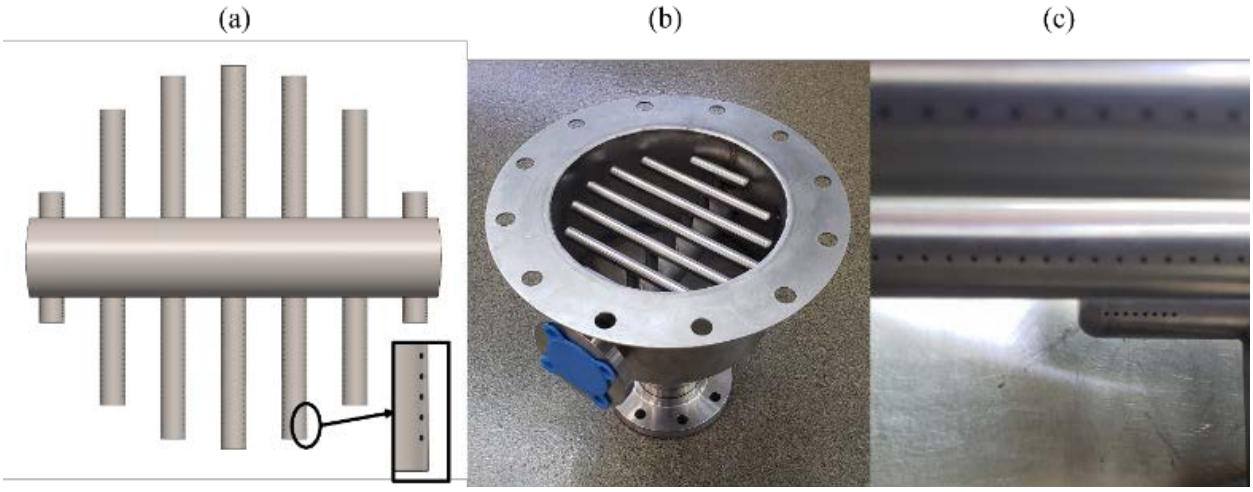

Figure 19. (a) Drawing of the air distributor with a bottom view. (b) Fabricated air distributor assembled with particle collector. (c) Bottom side of the fabricated air distributor showing the air grid holes. The air holes face downward to avoid particle clogging. The air distributor was designed to provide evenly distributed aeration for stable fluidization.

Table 6. Design Parameters of the Air Distributor

Parameter	Value	Units
Distributor grid thickness, t	3.05	mm
Distributor grid hole diameter, D_h	1	mm
Number of holes, N_h	540	-
Pitch, L_h	4.06	mm
Angle between rows of holes	120	°
Number of manifolds, N_m	7	-
Manifold diameter, D_m	12.95	mm
Lengths of manifolds	291.6, 276.36, 225.04, 99.06	mm
Header diameter, D_{head}	52.32	mm
Length of header	312.42	mm

2.2.1.2 Screw Conveyor

The screw conveyor is a modified Archimedes screw for mechanically conveying particles. The screw conveyor sits at the bottom of the HX and controls particle outflow. The screw conveyor is a repurposed 2-in soil augur fit into a 2-in iron pipe size (IPS) carbon steel pipe. Modifications were made to the augur and custom flanges, and bearing housings were fabricated to seal the particles and temperature. The augur can rotate freely in the pipe housing. Figure 20 shows a cutaway view of the screw conveyor design.

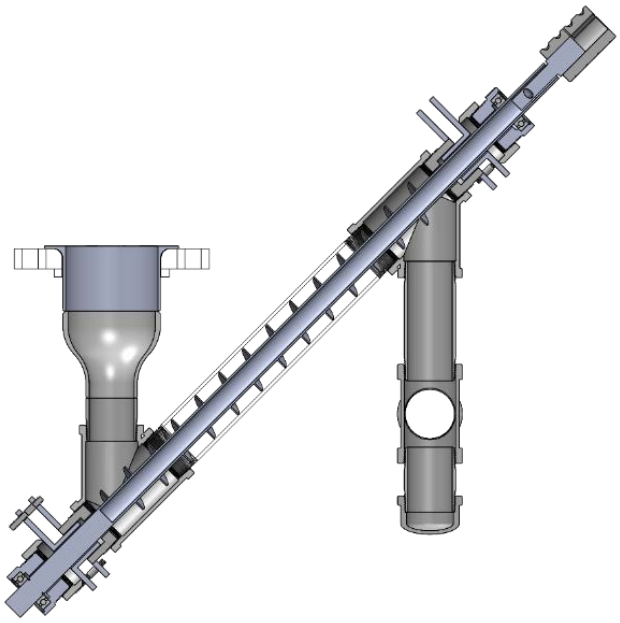

Figure 20. Screw conveyor consisting of a helical screw blade coiled around a shaft within a tube. As the shaft rotates, the screw blade moves the material along the length of the conveyor from bottom end to the upside.

The augur is turned by a three-phase induction motor (WorldWide Electric Corporation NATE1-18-56CB), which is speed controlled by a variable frequency drive (LSLV-G100). The screw conveyor assembly was tested in an independent test stand to calibrate the rotational frequency of the augur to the particle mass flow rate. The screw conveyor is inclined at a 45° angle from the bottom of the HX. This effectively plugs the FB and prevents fluidizing air from the air distributor from escaping downward and thus negating the fluidization.

The results of the screw conveyor calibration testing are displayed in Figure 21. Two calibration runs were performed to check whether the particles would smooth any roughness in the augur or the surrounding pipe. The average standard deviation of the measurement was 0.002 $kg \cdot s^{-1}$, resulting from the vibration and friction between the particles and the screw. It was thought that roughness would be smoothed away by the friction of the particles during initial runs and thus that subsequent running of the equipment would yield lower particle flow rates. This was not observed. Thus, for this short-lived research project, wear was not considered. However, if this design is scaled up or used in commercial or production equipment, screw wear might be significant after prolonged operation and would need to be accounted for.

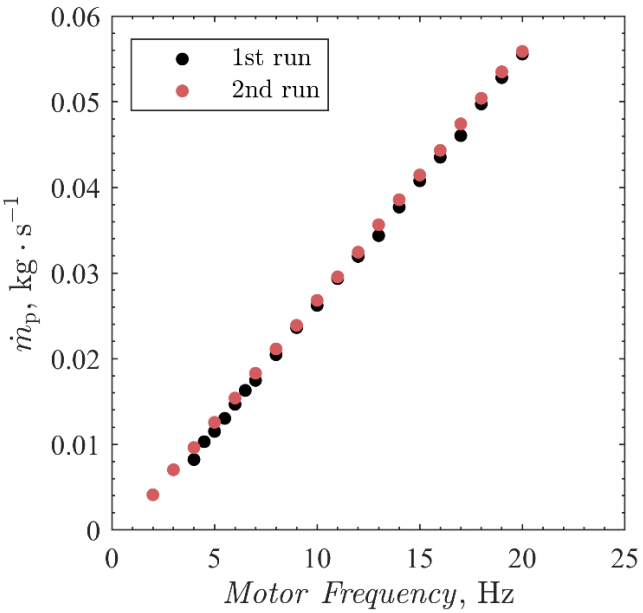

Figure 21. Screw conveyor particle mass flow rate as a function of augur frequency. The particle mass conveying rate showed a linear relationship to the screw rotation speed.

2.2.1.3 L-Valve Design, Fabrication, and Calibration

An L-valve is a pneumatically actuated, gravitationally driven particle flow rate control device. The L-valve, as its name suggests, is shaped like the letter L. It has a tall vertical standpipe and a relatively short horizontal pipe that are joined at a sharp 90° angle. The L-valve vertical standpipe is filled with particles. The sharp corner prevents particles from flowing under normal circumstances; the angle of repose of the particles from the corner requires a shorter horizontal section than is installed on the system. An aeration port is fitted toward the bottom of the vertical standpipe, through which air is injected into the packed particles. The location of this aeration

port and the resistance from the packed particles in the vertical standpipe causes air to preferentially escape through the horizontal section of the L-valve (the path of least resistance). This in effect "loosens" the particles sitting in the horizontal section, effectively decreasing the angle of repose and allowing the particles to traverse the horizontal section of the L-valve before ultimately exiting the L-valve. The constant supply of particles in the vertical standpipe allows this to run continuously.

The L-valve used in this prototype is a modified 2 IPS carbon steel pipe. Two aeration ports were added at 1.5 diameters and 2 diameters above the centerline of the horizontal section. Figure 22 shows the comparison between the engineering drawing of the L-valve and the part as received.

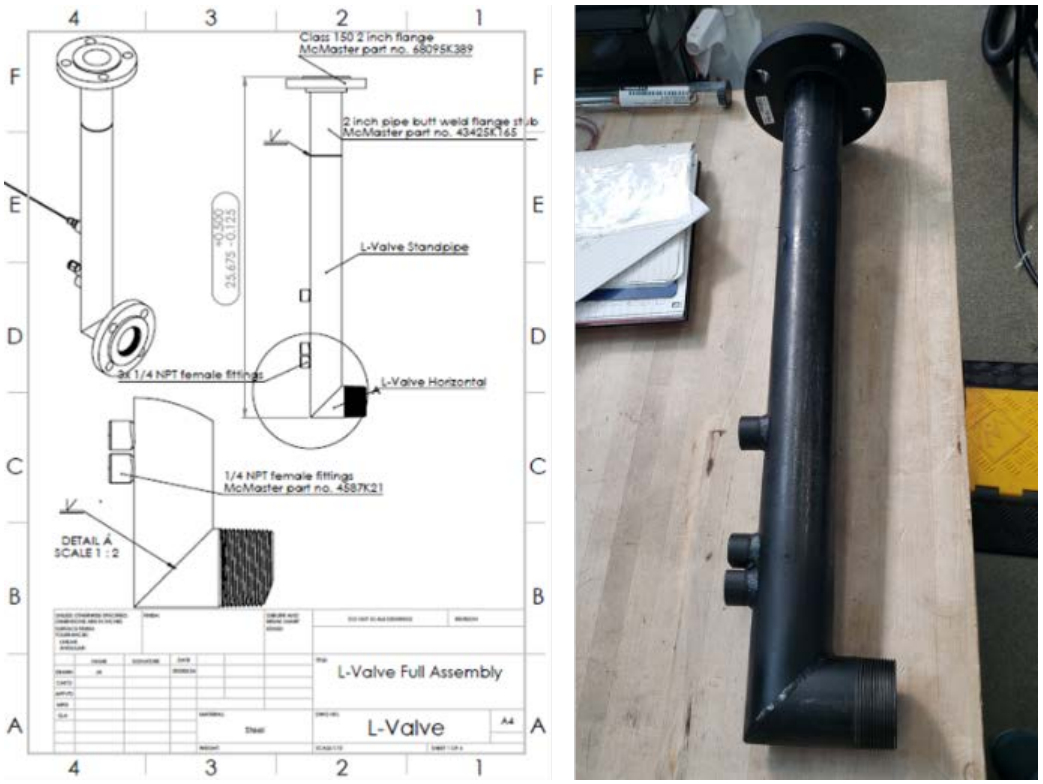

Figure 22. L-valve engineering drawing for fabrication (left) and as received (right). An L-valve is a pneumatically actuated system that can control the flow rate of particles moving downward.

Calibration tests were conducted on the L-valve used in the prototype FB HX to determine the particle mass flow rate ($\dot{m}_p$) compared to the air flow rate for the two aeration ports. These results are shown in Figure 23. Note that the linear relationship between the air flow rate and $\dot{m}_p$ is only valid for the air flow rates presented in Figure 23. Aeration below what is shown does not elicit any particle flow (air flows between particles as a packed bed behavior). Aeration above what is shown in Figure 23 may not maintain the linear relationship; $\dot{m}_p$ may plateau above a certain aeration rate and could even decrease, as reported by , but the calibration testing equipment was insufficient to achieve higher aeration flow rates to demonstrate the change of particle/air flow relationship. The average standard deviation of the measurement showed 0.005 $kg \cdot s^{-1}$, likely attributable to pressure fluctuations within the L-valve and variations in particle characteristics that impact the flow dynamics.

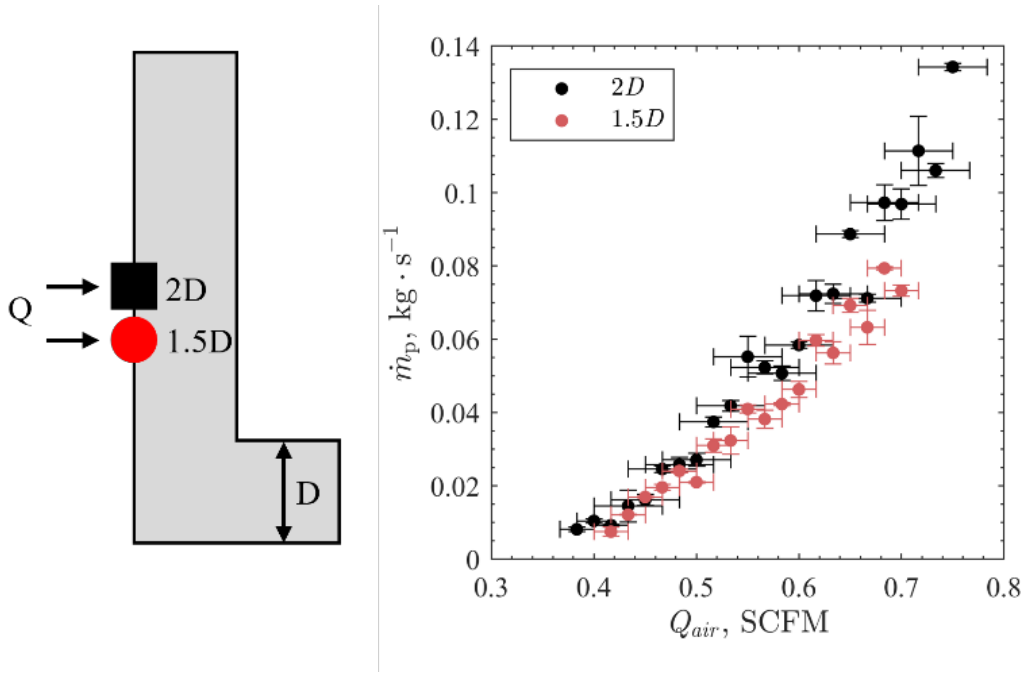

Figure 23. Calibration test results on the L-valve for particle mass flow rate as a function of air flow rate at different aeration ports and port sizes. The particle flow rate can be varied for different particle types, L-valve geometries, and air flow rates.

2.2.1.4 Pneumatic Conveyor Design and Analysis

Pneumatic conveying systems can transport solids in dilute or dense phase flow patterns. Dilute phase flow occurs when the air flow is great enough to create an even distribution of particles within the piping. Dense phase flow occurs when the air flow is too low to generate an even distribution of particles within the piping. Lower air flow can result in more particles gathering at the bottom of the piping, eventually moving the particles in slugs or plugs. Solid-to-air ratios of <10 typically result in dilute phase flow, whereas ratios >30 typically result in dense phase flow . Various particle properties determine whether dilute or dense phase flow is more appropriate; however, the process can often be simplified by looking at the particles' loose-poured bulk density. Typically, particle density more than 1,000 kg/m^3 can only be transported in dilute phase flow .

Air speed within a pneumatic lift system must be greater than the system's choking and saltation velocities to ensure proper flow. The system's choking velocity represents the air speed at which the gravitational force on the particles matches the upward forces acting on them. Air speeds below the choking velocity result in blockages forming at the bends, leading to vertical piping sections. A pneumatic transport system's saltation velocity represents the air speed at which particles fall out of suspension and is the point at which the flow switches between dense and dilute phase transport. Dilute phase systems should not have issues with choking, as choking velocities are less than or equal to their respective saltation velocities .

Although this makes the chocking velocity less important for dilute system design, it is still a good way to double-check the accuracy of saltation velocity predictions. Choking can be prevented by keeping the air velocity greater than two times the particle terminal velocity . A spherical particle's terminal velocity is expressed as:

$$U_{\mathrm{t}} = \sqrt{\frac{4gD_{\mathrm{p}}(\rho_{\mathrm{p}} - \rho_{\mathrm{air}})}{3\rho_{\mathrm{air}}C_{\mathrm{D}}}} \tag{11}$$

where C_{D} is the particle drag coefficient , D_p is the particle diameter, g is gravitational acceleration, ρ_{p} is the particle density, and ρ_{air} is the air density. The saltation velocity can be expressed as :

$$U_{\mathrm{gs}} = \left[\left(\frac{\rho_{\mathrm{p}}}{\rho_{\mathrm{air}}}\right)^{-1.06}\left(\frac{U_{\mathrm{t}}}{10\sqrt{gD_{\mathrm{p}}}}\right)^{3.7}\frac{4\dot{m}_{\mathrm{p}}\times 10^{3.61}\left(\sqrt{gD_{\mathrm{pipe}}}\right)^{3.61}}{0.373\pi\, D_{pipe}^{2}\,\rho_{\mathrm{air}}}\right]^{1/4.61} \tag{12}$$

where D_{pipe} is the piping diameter and $\dot{m}_{\mathrm{p}}$ is the particle mass flow rate. A safety factor of 10%–20% of the saltation velocity is recommended to ensure that flow remains in the dilute phase throughout the transport system .

The total pressure drop within particle-air lifts is expressed as:

$$\Delta P_{\mathrm{t}} = \Delta P_{\mathrm{a}} + \Delta P_{\mathrm{s}} + \Delta P_{\mathrm{f}} + \Delta P_{\mathrm{m}} \tag{13}$$

where ΔP_{t} is the total pressure drop; ΔP_{a} is the acceleration pressure drop; ΔP_{s} is the static pressure drop; ΔP_{f} is the frictional pressure drop; and ΔP_{m} is the miscellaneous pressure drop . The pressure required to accelerate initial stationary particles in the pneumatic conveying system is ΔP_{a}. ΔP_{a} is expressed as:

$$\Delta P_{\mathrm{a}} = \frac{2\dot{m}_{\mathrm{p}}{U_{\mathrm{p,h}}}^{2}}{U_{\mathrm{gs}}\pi D_{\mathrm{pipe}}^{2}} \tag{14}$$

where $U_{\mathrm{p,h}}$ is the particle velocity in the horizontal sections of the piping. A straight pipe length of at least 25–50 x D_{pipe} is necessary to ensure particles have enough time to accelerate to their maximum speed . ΔP_{s} results from the gravitational force within the vertical piping sections, expressed as:

$$\Delta P_{\mathrm{s}} = \rho_{\mathrm{p}}(1 - \varepsilon_{\mathrm{pipe}})\Delta Z g + \varepsilon_{\mathrm{pipe}}\rho_{\mathrm{air}}\Delta Z g \tag{15}$$

where $\varepsilon_{\mathrm{pipe}}$ is the particle voidage in the pneumatic pipe and ΔZ is the net increase in elevation. $\varepsilon_{\mathrm{pipe}}$ is expressed as:

$$\varepsilon = 1 - \frac{\rho_{\mathrm{air}}U\dot{m}_{\mathrm{p}}}{\rho_{\mathrm{p}}U_{\mathrm{p}}\dot{m}_{\mathrm{air}} + \rho_{\mathrm{air}}U\dot{m}_{\mathrm{p}}} \tag{16}$$

The frictional pressure drop ΔP_{f} is expressed as:

$$\Delta P_{\mathrm{f}} = \Delta P_{\mathrm{p}} + \Delta P_{\mathrm{air}} \tag{17}$$

where ΔP_{p} is the frictional pressure drop due to particles and ΔP_{air} is the frictional pressure drop due to the air. ΔP_{p} is expressed as:

$$\Delta P_{\mathrm{p}} = \left(\frac{\dot{m}_{\mathrm{p}}}{\dot{m}_{\mathrm{air}}}\lambda_{\mathrm{p}}\right)\frac{\rho_{\mathrm{air}}U^2 L_{\mathrm{pipe}}}{2D_{\mathrm{pipe}}} \tag{18}$$

where λ_{p} is the solids friction factor and L_{pipe} is the total length of the piping. λ_{p} is expressed as:

$$\lambda_{\mathrm{p}} = K\left(\frac{\dot{m}_{\mathrm{p}}}{\dot{m}_{\mathrm{air}}}\right)^a\left(\frac{U^2}{gD_{\mathrm{pipe}}}\right)^b\left(\frac{{U_{\mathrm{t}}}^2}{gD_{\mathrm{p}}}\right)^c\left(\frac{D_{\mathrm{pipe}}}{D_{\mathrm{p}}}\right)^d \tag{19}$$

where K, a, b, c, and d are coefficients and exponents. Weber's coefficients for coarse particles ($D_{\mathrm{p}} > 500$ μm) were adopted, where $K = 0.082$, $a = -0.3$, $b = -0.86$, $c = 0.25$, and $d = 0.1$. ΔP_{air} is expressed as:

$$\Delta P_{\mathrm{air}} = \lambda_{\mathrm{air}}\frac{\rho_{\mathrm{air}}U^2 L_{\mathrm{pipe}}}{2D_{\mathrm{pipe}}} \tag{20}$$

where λ_{air} is the air friction factor.

The pneumatic conveyor is powered by a Republic Manufacturing HRC500 blower. From the screw conveyor, particles are injected into the pneumatic conveyor piping, which is constructed from 2 IPS carbon steel pipe. At the top of the pneumatic conveyor, an air-particle separator (Oneida Air Systems AXD002030SS) separates particles, returning them to the particle storage bin and allowing the air to exhaust. The opening to the air-particle separator is 5-in. inner diameter (ID). A custom pipe reducer was fabricated to mate the 2 IPS pipe with the 5-in. tube. Long radius elbows were procured to minimize pressure drops through the pneumatic conveyor system. All piping is fitted with wraparound couplers (Morris Couplings) that do not protrude into the flow and thus do not introduce any restrictions or accompanying pressure drops. The pneumatic conveyor closes the particle loop.

After the air-particle separator, this lab-scale prototype uses a secondary filter: a water barrel in which the exhaust pipes from the pneumatic lift and the FB HX are submerged. Any fine particles that are not effectively separated by the cyclones will be captured by the water and not exhausted into the air, where they could pose harm to operators, bystanders, or nearby equipment.

The pneumatic conveyor was calculated to assume an $\dot{m}_{\mathrm{air}}$ of 10 times the $\dot{m}_{\mathrm{p}}$ for dilute phase pneumatic conveying. Because ρ_{p} is several orders of magnitude higher than ρ_{air}, the pressure drop throughout the pneumatic conveyor was calculated assuming a single-phase air flow. The pressure drop of each component of the pneumatic conveyor was determined, including the pressure drop of flow through a pipe, elbows, expansion from 2 IPS to 5 in., an air-particle cyclone, and the water filter. To demonstrate these calculations, $\dot{m}_{\mathrm{p}} = 0.05$ kg·s^{-1} is used. U_{t} of the particle is calculated from the particle terminal velocity in classical physics. At the $\dot{m}_{\mathrm{air}}$ provided by the blower, the drag coefficient on the spherical particle is estimated at 1.5 . Thus, the U_{t} of the particle is approximately 3.1 m·s^{-1}. To ensure the particles remain entrained in the air flow, the air speed must remain above this value.

The total length of the pneumatic conveyor was conservatively estimated at 6 m. Furthermore, the elbows each add an approximate equivalent 1 m of length . The pressure drop caused by the length of the pneumatic system is calculated from the Darcy–Weisbach equation, resulting in a

pressure drop of 4.5 kPa. The pressure drop introduced by the expansion from 2 IPS pipe to 5 in. expander is calculated by Hooper's 2-K method. Based on the geometry of the as-received reducer, the pressure drop was calculated as only 0.4 kPa and thus is a minor loss in the system. The pressure drop in the air-particle separating cyclone was calculated by summing pressure drops attributed to the fluid contraction, acceleration of solids, barrel friction, fluid reversal, and outlet contraction. Based on the geometry of the as-received cyclone, the pressure drop is estimated as 0.6 kPa. The pressure drop caused by the water filter is estimated as the hydrostatic pressure of the water. This is a controllable element in this system and can change based on experimental observations. However, to keep the system within the pumping pressure provided by the blower, the exhaust pipe is submerged in approximately 0.5 m of water, or approximately 5 kPa. By summing each element of the pneumatic conveyor, the total pressure drop is estimated at 10 kPa with a minimum air speed of 20 $m \cdot s^{-1}$. These satisfy the capacity of the blower and the necessary air speeds to maintain the entrainment of particles.

2.2.2. Air/Particle Direct-Contact Heat Exchanger Operation Studies

The assembled test station was verified through a shake-down test and commissioning and performance testing under applicable operation conditions. The test procedure and outcomes are described to show the critical operating principles of the air/particle direct-contact FB HX design and operation needs.

Tests were performed by filling the bed to the desired height with particles and fluidizing the particles with the air incoming at the specified temperature and flow rate. Because the fluidizing air first passes through the heating system and because the heater has significant thermal mass, the system took considerable time to reach the desired set point. During this warmup period, the air flow was directed into the FB HX, which fluidized and heated the particles — air flow through the heater is necessary for the heater to heat up, and there were no bypass valves installed that would allow the air to be exhausted away from the FB HX until reaching the desired temperature. In a way, this mimics the behavior of a real system startup, but it added complication to establishing uniform starting conditions. Particles flow through the bed were maintained during this warmup period.

The inherent challenge of this system is to carefully balance the behavior between fluidization, which mixes bed media into a uniform temperature mass, and desired counterflow HX behavior, which performs optimally with stratified temperature gradients. Thus, the goal becomes injecting air into the particle bed to improve the convective heat transfer coefficient but minimize mixing of particles throughout the bed. If done successfully, the bed will attain thermal stratification, whereby the temperature of the particles at the bottom of the bed is nearly equal to the temperature of the incoming air, and the temperature of the particles at the top of the bed is equal to the incoming particles from the feeder (by extension, the outgoing air temperature should be equal to the temperature of the top layer of the bed).

By nature of the direct contact between the fluidizing air and the particles, and the low particle Biot number, the local temperature difference between air and particles is quite small , and a single temperature measurement can be assumed to be representative of both the air and particles at that location. Because of this small local temperature difference between air and particle, the heat exchange occurs as the air from one thermal layer moves upward to colder thermal layers. Due to the density difference between air and particles, the particles appear relatively stationary:

The residence time of air is on the order of seconds, and the residence time of particles is on the order of an hour.

As the air moves between thermal layers of the bed and exchanges heat with the local particles, the air temperature changes, and therefore its thermophysical properties change. Most notably, a change in air density occurs between the top and bottom of the bed due to the temperature variations. In this experiment, hot air enters the bottom of the particle bed and cools as it moves upward. Thus, the density is lowest at the bottom and increases as it moves toward the top. Because this bed is straight-walled and the mass flow of air is constant, the superficial velocity of air is a function of this changing density—fastest velocity at the bottom of the bed, slowest velocity at the top. This complicates the operation of this FB HX: To increase convective heat transfer between particles and air, the velocity of the air should be increased. However, if the air superficial velocity exceeds the minimum fluidization velocity (u_{mf}) in any thermal layer, the bed is prone to significant mixing. Thus, it was determined that the maximum velocity of the air must be near to or slightly less than the minimum fluidization velocity. Adding uncertainty is the sheer number of correlations for the minimum fluidization velocity . Through extensive testing, it was determined that the correlation presented by , despite its age, best represents the behavior in the FB HX used in this test and is reproduced in Equation 21.

$$u_{mf} = \frac{\mu}{\rho_a d_p}((33.7^2 + 0.0408Ar)^{0.5} - 33.7) \quad (21)$$

where u_{mf} is the minimum fluidization velocity, d_p is the particle average diameter, ρ_a is the density of fluidizing air, μ is the dynamic viscosity of the fluidizing air, and Ar is the Archimedes number that compares gravitational/buoyancy forces to viscous forces. Local mixing is not always problematic; if mixing occurs only within a thermal layer, it ensures that the air does not channel through the particles, which can create dead zones of low particle mobility through the HX. However, achieving only local mixing within individual thermal layers is challenging and difficult to control. Even in the bubbling phase of fluidization for Geldart B particles, there can be significant back mixing of particles between layers of the bed . And it is hypothesized that bubble growth inhibits heat exchange between air and particles; the effective contact area between air and particles decreases as bubbles grow. This results in hot air bubbles from the bottom of the bed traversing the vertical height of the bed without exchanging significant heat with the particles; thus, the exhaust gas from these bursting bubbles expels hot air that failed to thermally interact with the particles. As the superficial velocity increases, fluidization becomes more turbulent, and the solids holdup decreases, which further results in air traversing through the bed without significantly exchanging heat with the particles. The decrease in air residence time is not a significant factor, but it does further reduce the heat transfer.

The final complication of air/particle heat transfer is that the energy transfer rate of air and particles should equal each other. In practice, because the air flow rate is determined by the fluidization condition, balancing the energy transfer rate is achieved by determining the particle mass flow rate (Equation 22). Because the specific heat is also a function of temperature, it is necessary to integrate over the conditions achieved in the bed to get a more accurate match. However, this can be fine-tuned during testing if the data is available and dynamic controls are installed. The temperature range in these tests is relatively small, but temperature-dependent

properties must be carefully considered for accurate system balancing, especially if larger temperature ranges are considered. For a balanced HX, the mass flow rate of particles can be represented by Equation 22:

$$\dot{m}_{particle} = \frac{\left(\dot{m}\int_{T_{air,out}}^{T_{air,in}} c_p(T)dT\right)_{air}}{\left(\int_{T_{part,in}}^{T_{part,out}} c_p(T)dT\right)_{particle}} \quad (22)$$

where $c_p(T)$ is the temperature-dependent specific heat. Because the air velocity is tied to the mass flow rate and it is necessary to operate such that the maximum velocity is near the minimum fluidization velocity, there is a very narrow window of allowable operation, if any. The achievable lower limit of the fluidization air for this system is 22 SCFM (0.0127 kg/s). Initially, the minimum for this system was 40 SCFM (0.0213 kg/s), which translated to a $u/u_{mf} \approx 2.2$ using the correlation from ; this is far higher than is desired to maintain thermally stratified layers (and assuming the air temperature at the bottom of the bed is 300°C). Considerable effort was made to reduce the lower limit of the fluidizing air flow rate while reusing the equipment available. At a flow rate of 22 SCFM (0.0127 kg/s), the $u/u_{mf} \approx 1.1$, which is acceptable for the desired conditions in the bed (assuming the air temperature at the bottom of the bed is equal to 300°C). As will be shown, the measured air-particle temperature will not approach this upper value, and thus this air flow rate does allow some operation in both packed bed and FB regimes.

Satisfying Equation 22 results in a balanced HX. However, an unbalanced HX provides more flexibility to operate over additional conditions. Because the transfer rate of air must be set such that it satisfies the flow rates to meet the minimum fluidization velocity requirement, only the particle flow rate can be varied. Therefore, despite the limited operating window afforded by meeting the minimum fluidization requirements with the equipment available, some degree of freedom for operating the system is achieved by purposefully unbalancing the HX.

The overall heat exchange can be calculated using Equation 23. As shown, there are three equivalent equations: (1) the change in energy of the air, (2) the change in energy of the particles, and (3) the overall heat exchange calculated using the log mean temperature difference method. The first two can be calculated with the data collected from the test results and should show agreement if no significant losses are present. The last is used for analysis of the overall HX performance.

$$\dot{Q} = \dot{m}_{air}\int_{T_{air,out}}^{T_{air,in}} c_{p,air}(T)dT = \dot{m}_{particle}\int_{T_{part,in}}^{T_{part,out}} c_p(T)dT = UA(LMTD) \quad (23)$$

where UA is the overall heat transfer coefficient multiplied by the heat transfer area and LMTD is the log mean temperature difference.

2.3 Analysis of PFB HX Prototype Test Results

The PUMP FB HX was tested under many different conditions, and only a subset of test results is included here. Figure 24 shows the temperature profile of the bed during a test condition in which the fluidizing air was delivered at 325°C at an average air flow rate equal to 24.2 SCFM (0.0140 kg/s). The air velocity is expected to range from very slightly above minimum

fluidization to slightly below minimum fluidization over the range of air temperature conditions in this test. The horizontal axis is the location in the bed ascending from left to right, and the vertical axis is the temperature measured by the thermocouple probes immersed in the bed. The vertical lines represent the range of recorded temperatures during the test period. In this scenario, the HX flow rates were balanced. The first item of note is that the approach temperature at the bottom of the bed is quite high, at >125°C. The inlet air temperature is measured within the air distributor, which records only the air temperature; however, the thermocouples immersed in the bed measure the combined air-particle temperature, which should be locally uniform. Additional thermocouple probes measure the packed particle temperature beneath the air distributor—there should be no air-particle mixing in this location.

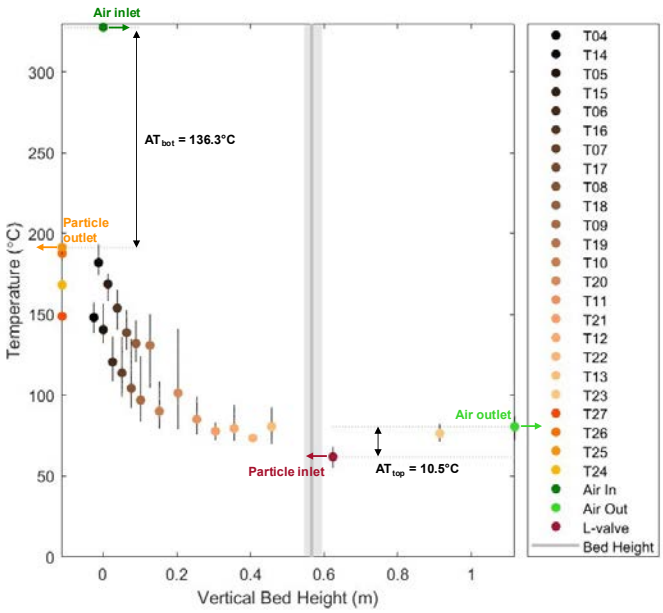

Figure 24. Temperature distribution of the FB HX test with inlet air flow of 24.2 SCFM (0.0140 kg/s) at 325°C with a balanced HX flow rate

Also of note in Figure 24 is that the two thermocouple probes indicate two different temperature gradients in the bed. We hypothesize that the air flow from the distributor is not uniform. The cause of this could be imperfections in the air distributor, which can cause air to preferentially flow through some nozzles but not others.

Another explanation is that the bed may also not have a uniform height, which affects the air flow patterns through the bed. The L-valve injects particles into the bed through the side wall. This inlet is preferentially oriented toward one thermocouple probe, as shown in Figure 25. If the superficial air velocity at the top of the bed is less than the minimum fluidization velocity, there is no mixing at the top of the bed. This may cause the bed surface to slope away from the L-valve inlet at the angle of repose of the particles. This sloped bed surface may then cause small pressure gradients within the bed, resulting in a nonuniform flow from the air distributor. The nonuniform flow may result in differing heat transfer between air and particles at different locations within the bed, and this is recorded by the thermocouple probes. The thermocouple probe recording the lower temperature is nearer to the L-valve inlet. Thus, the hypothesis is that

the higher bed surface height nearer the L-valve inlet location causes air to preferentially flow on the side of the bed opposite the L-valve inlet, which means that there is more air flow, and thus more heat exchange, between particles in this region of the bed. More data will be needed to validate this hypothesis and test the significance of small bed height effects.

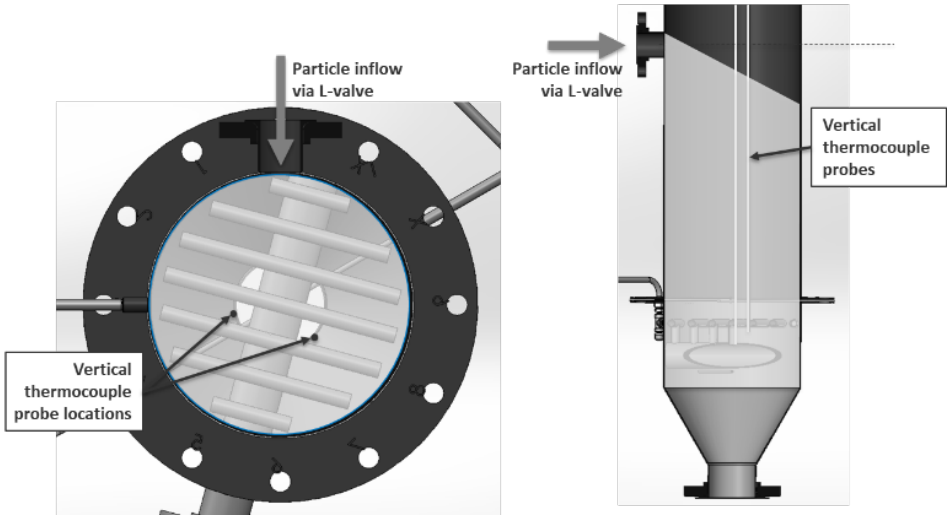

Figure 25. CAD drawings of the FB HX showing the location of the L-valve inlet and the positions of the vertical thermocouple probes

Figure 26 shows the calculated u/u_{mf} for the bed based on the test data presented in Figure 24. As can be seen, the different temperature profiles measured by the two different probes appear here due to the temperature dependency of the superficial velocity and, to a lesser extent, the minimum fluidization velocity. What is notable in Figure 26 is that the bottom of the bed has a calculated $u/u_{mf} > 1$, but this value drops to less than one toward the top of the bed. We hypothesize that the pressure caused by the weight of the particles at the top of the bed suppresses bubble growth in the bottom of the bed. The air bubbles shrink with reduced fluidization when they move upward until they are dispersed, and a packed bed flow dominates at the top of the bed. This operation is dubbed a "mixed bed," where the minimum fluidization indicator suggests fluidization at the bottom of the bed but a packed bed at the top.

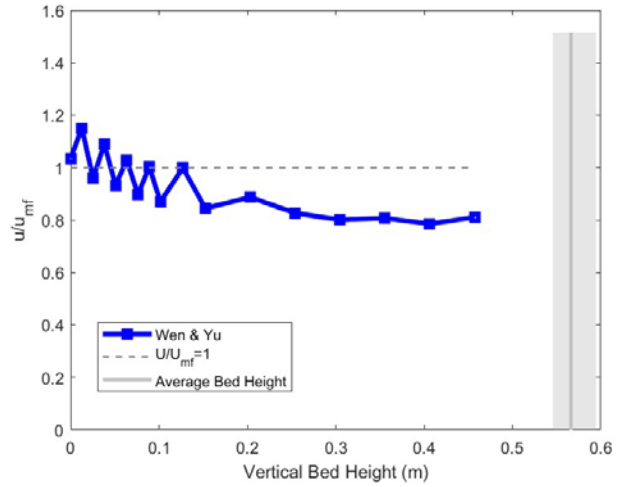

Figure 26. Ratio of superficial velocity to minimum fluidization velocity, calculated from the test results presented in Figure 24

Figures 24 and 26 show the performance when the bed was operating in a "mixed" configuration, where the calculated superficial velocity fell below the minimum fluidization velocity partway through the vertical column of the bed. In contrast, Figures 27 and 28 show data of the same type but during a test in which the bed was fully fluid. In this test, fluidizing air was delivered at 300°C with an average flow rate of 24.9 SCFM (0.0144 kg/s). A key difference in this test event was that the measured temperatures fell within a much narrower range (128°C–154°C). This indicates that the bed was mixing more than the results presented in Figure 24, resulting in a more uniform temperature gradient throughout.

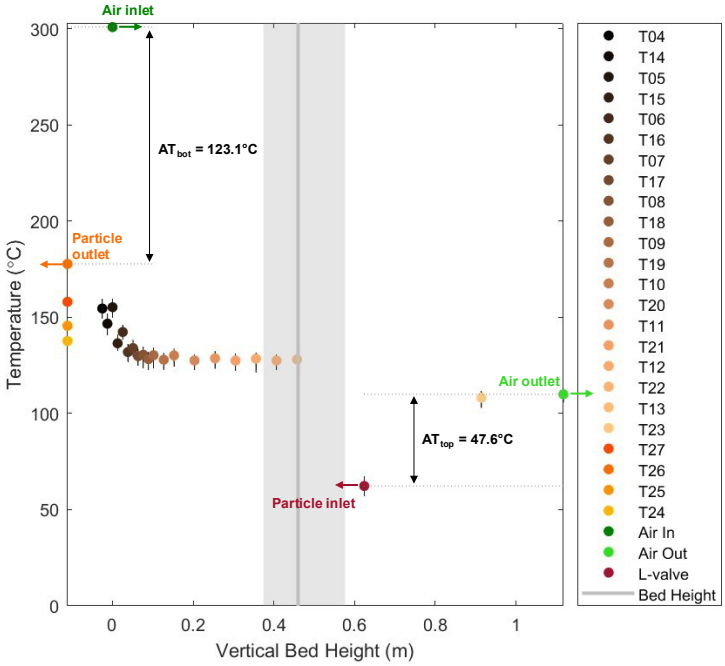

Figure 27. Temperature distribution of FB HX test with inlet air flow of 24.9 SCFM (0.0144 kg/s) at 300°C with a balanced HX flow rate

The ratio of the superficial velocity to the minimum fluidization velocity shown in Figure 27 indicates that the whole bed column is fluid. Again, the temperature dependency of the bed is evident in this calculation. Also note that Figures 27 and 28 show the comparison of the average bed height, which is shown by a vertical grey line. The shaded region around this line indicates the fluctuations in this calculation during the time series. For the "mixed bed" test shown in Figures 24 and 26, the bed height is more consistent (i.e., the shaded region is narrower) than the fully fluid bed in Figures 27 and 28. The bed height calculation is derived from readings of the differential pressure transducers. Because fluid beds contain rapid and unstable pressure fluctuations , a noisier signal and therefore noisier calculation is an additional check that the fluid bed is in the regime of moving bed.

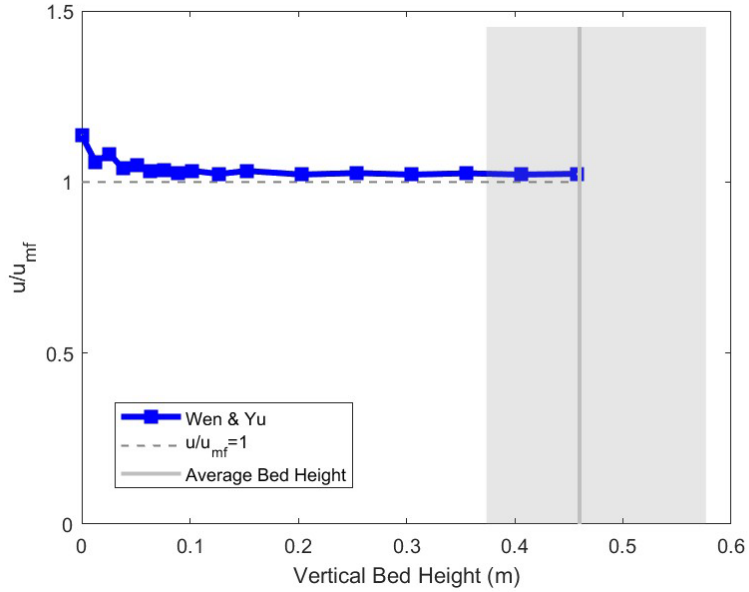

Figure 28. Ratio of superficial velocity to minimum fluidization velocity calculated from the test results presented in Figure 27

For both tests presented in Figures 24 and 26 (mixed bed) and Figures 27 and 28 (FB), the mass flow rates of air and particles are nearly identical, about 0.014 kg/s and 0.015 kg/s, respectively. Thus, the overall heat transfer rate, $\dot{Q}$, and the overall heat transfer coefficient, *UA*, can be calculated and compared from Equation 23. The mixed bed had an overall heat transfer rate of 1.4 kW, whereas the fully fluid bed had an overall heat transfer rate of just 0.74 kW. This decrease in overall heat transfer rate is attributed to the unwanted mixing and bubbling behavior of the FB in the fluid regime; as hypothesized, the bubbles grow such that they traverse the FB without interacting and exchanging heat with the particles.

Using the LMTD method, the *UA* values for the mixed and fluid beds are 24 W/K and 9 W/K, respectively. For a direct-contact HX, these values are low, and it is an ongoing investigation to increase these values. An important note is that in this FB HX system, and any direct particle-air HXs, the HX surface area is the summative surface area of the particles within the bed. This can be calculated by knowing the bed height, the solids holdup for the current fluidization regime, and the particle diameter and shape. It is estimated that in this system, there is ~9,600 m^2 of heat transfer surface area per cubic meter of HX volume. This is orders of magnitude higher than FB

HX configurations with immersed structures or partitions. Therefore, the FB HX concept presented here is an excellent candidate for solid-particle HX systems, but more work is needed to debug the operation and develop the technology to achieve lower approach temperatures, higher overall heat transfer rates, and more robustness to off-design operation. Potential solutions are discussed below.

The difference between the mixed bed operating at an average air flow rate of 24.2 SCFM (0.0140 kg/s) and the FB operating at 24.9 SCFM (0.0144 kg/s) is just 0.4 g/s of air. This sensitivity to air flow results in a system that is difficult to control with the equipment available. Much effort was expended on developing controls to minimize any fluctuation in the air flow rate supply that could inadvertently trip the system from a mixed bed condition to an FB condition. Once the system is tripped into fluidization, it cannot be easily recovered; the mixing causes higher temperatures throughout the bed column that result in faster air velocities in the bed—a positive feedback loop. Because the particle residence time is nearly an hour or more, removing the particles and developing a new thermally stratified bed takes considerable time and is not guaranteed to develop in the same way. Because this system is a closed particle loop, particles accumulate temperature throughout the test period; what started out as room temperature particles entering the bed at the beginning of the test can turn into particles of up to 70°C near the end of the test period. This changes the HX calculations and energy flow rate balance, meaning that the particle flow rate needs to be dynamic and watched throughout the test. In a large-scale PTES system, this problem is unlikely to arise, as the cold storage will have sufficient particles to negate the need to recycle particles (unless there is some unique operation configuration).

Larger particle sizes needed to be considered to improve the FB HX performance. The 625-µm particles used in this test appear to be too small to practically achieve the balance between fluidization behavior and desired HX thermal stratification. Larger particles, even moving into the Geldart Group D size range, should yield more favorable trade-offs for the equipment available. Perhaps the most impactful effect of using larger particles will be in the calculation of the minimum fluidization velocity. As shown in Equation 21, the diameter of the particle, d_p, is reciprocal to the minimum fluidization velocity. Thus, using larger particles will allow for higher superficial velocities, which will increase the convective heat transfer coefficient and the total heat transfer of the HX. However, there is some uncertainty about using Geldart Group D particles. Firstly, it is unclear whether the same correlation for minimum fluidization velocity can be used—this will need to be evaluated through testing. Secondly, the fluidization behavior is different from Group B particles, as there is no bubbling regime and the bed can spout .

Considering the need to increase the particle size to improve the HX performance, we then performed tests with particles of 825-µm mean diameter. These particles straddle the border between Geldart Groups B and D when fluidized by air at the temperatures and pressures in this test but behave closer to Geldart D particles during fluidization. The motivation for using Geldart D particles was that the larger particles will allow for higher fluidizing air flow rates without destabilizing mixing, resulting in unwanted turbulent fluidization behavior, or enabling the bubble growth associated with Geldart B particles.

Figure 29 shows this measured temperature distribution within the bed with 825-µm particles with a 23-SCFM (13.3-g/s) fluidizing air flow rate. In comparison to Figure 24 and Figure 27

with 600-µm particles, the results presented Figure 29 show a much greater temperature gradient in the bed with a lower approach temperature at the bed bottom: 64.0°C. We hypothesize that these larger particles are less prone to mixing, which results in more stable temperature stratifications in the bed vertical column.

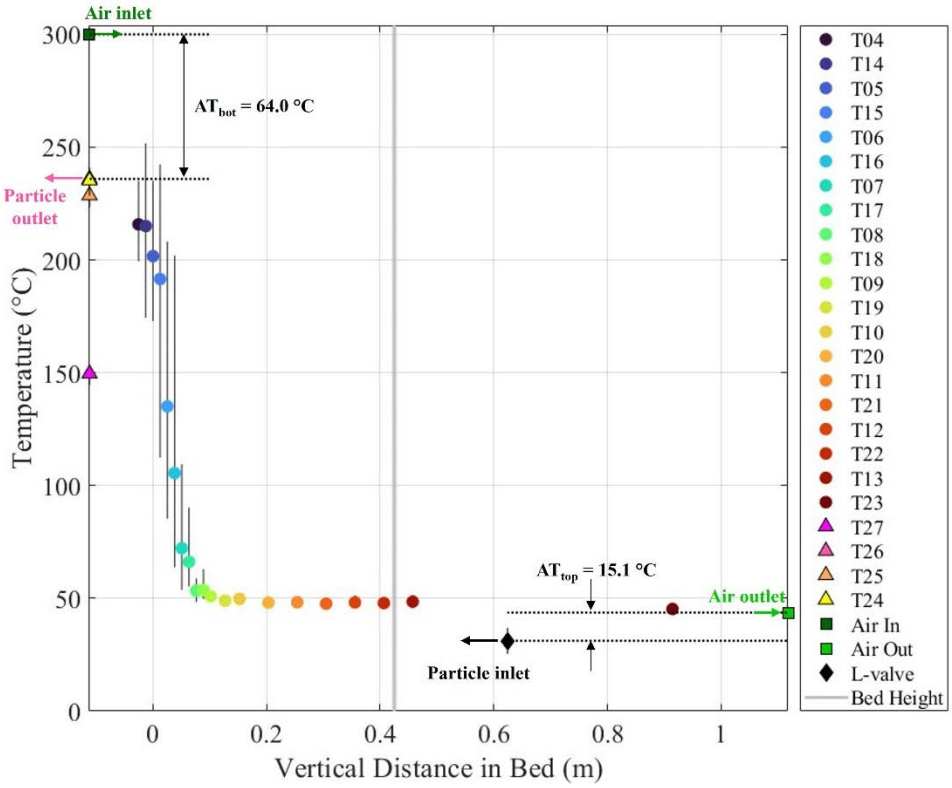

Figure 29. Temperature distribution of the HX with 825-µm particles at a fluidizing air flow rate of 23 SCFM (13.3 g/s)

Figure 30 shows the temperature gradient in the bed with 825-µm particles experiencing a fluidizing air flow rate of 25 SCFM (14.5 g/s). Compared to Figure 29, the temperature gradient is less steep, but it is wholly contained within the bed column, which leads to the lowest approach temperatures recorded in this setup: 43.5°C and 11.1°C at the bottom and top of the bed, respectively. Figure 31shows the time series for the data presented in Figure 30. It is evident that the temperature stratifications in the bed are stable in the long run; fluctuations at the lower thermocouple measurement points may indicate some local mixing, but this does not destabilize the bed column, leading to a uniform temperature mass in the bed (as seen with the 600-µm particles). Above 25 SCFM, the 825-µm particles display less stable behavior and are prone to mixing from perturbations in the system.

In these experiments, hot air is brought in at the bottom of the HX and exchanges heat with cold particles. The air properties—most notably the air density—change as a function of temperature. Thus, the air density is lowest at the bottom of the HX. Because the HX is a straight-walled cylinder, the low air density corresponds to the highest superficial velocity at the bottom of the bed, and as the air moves upward and exchanges heat with the particles, the density increases and the superficial velocity decreases. This creates a precarious situation, wherein if the superficial

velocity at the bottom of the bed causes significant fluidization, the entire vertical bed column is likely to fluidize due to particle mixing and bubble growth. This destroys thermal stratification, causing the air temperature in the upper portions of the bed to increase and thus fluidization mixing to increase in these upper regions. This behavior is a positive feedback loop that occurs nearly instantaneously.

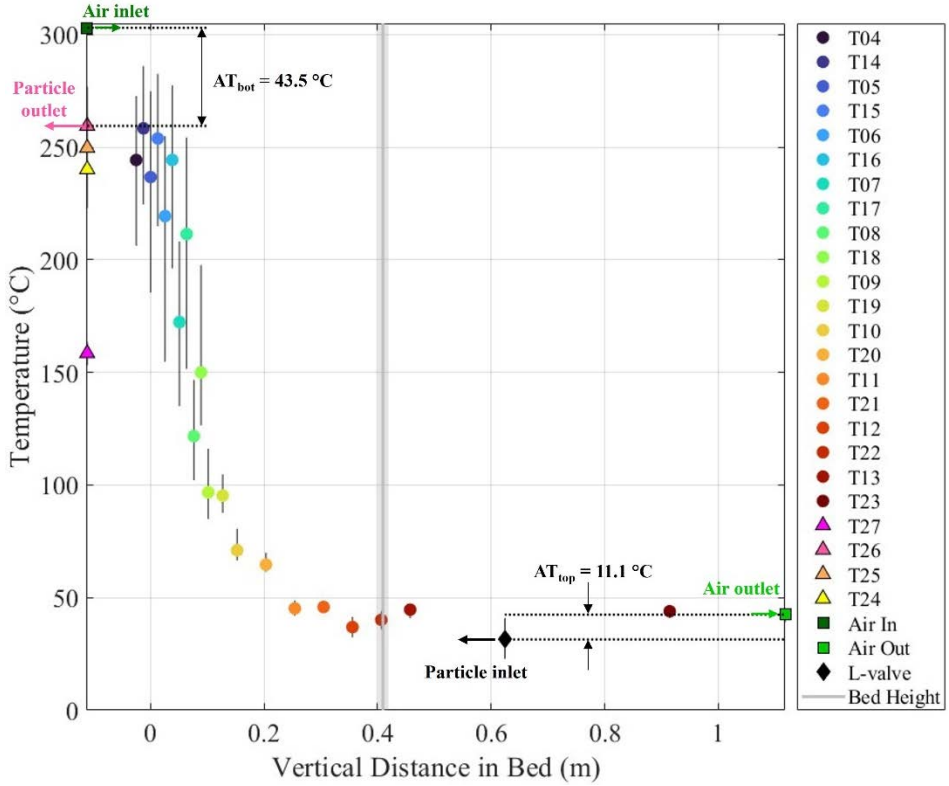

Figure 30. Temperature distribution of the HX with 825-µm particles at a fluidizing air flow rate of 25 SCFM (14.5 g/s)

The larger particles, bordered between Geldart Group B and D classifications, resulted in more stable beds, where the thermal stratification remained despite some local mixing seen in the time series data. The larger particles are heavier and less likely to be carried around by the air flow, preventing unwanted mixing in the bed column. Therefore, the large particles allow higher superficial air flow rates, increasing local convective heat transfer between air and particles while maintaining thermal stratification. It is unclear how Geldart Group D particles would perform in this HX; the fluidization behavior differs from Group B particles in that there is no bubbling phase, and the bed can spout and channel more readily. The drawback of using large particles relates mostly to considerations of particle conveyance and the specific surface area of the bed. In a pneumatic conveyance pipeline, larger particles will require more energy to move. In the bed, the larger particles have a lower surface area to exchange heat with the air, which may detract from the desired HX performance. Further investigations with Geldart Group D particles are needed to derive solid conclusions.

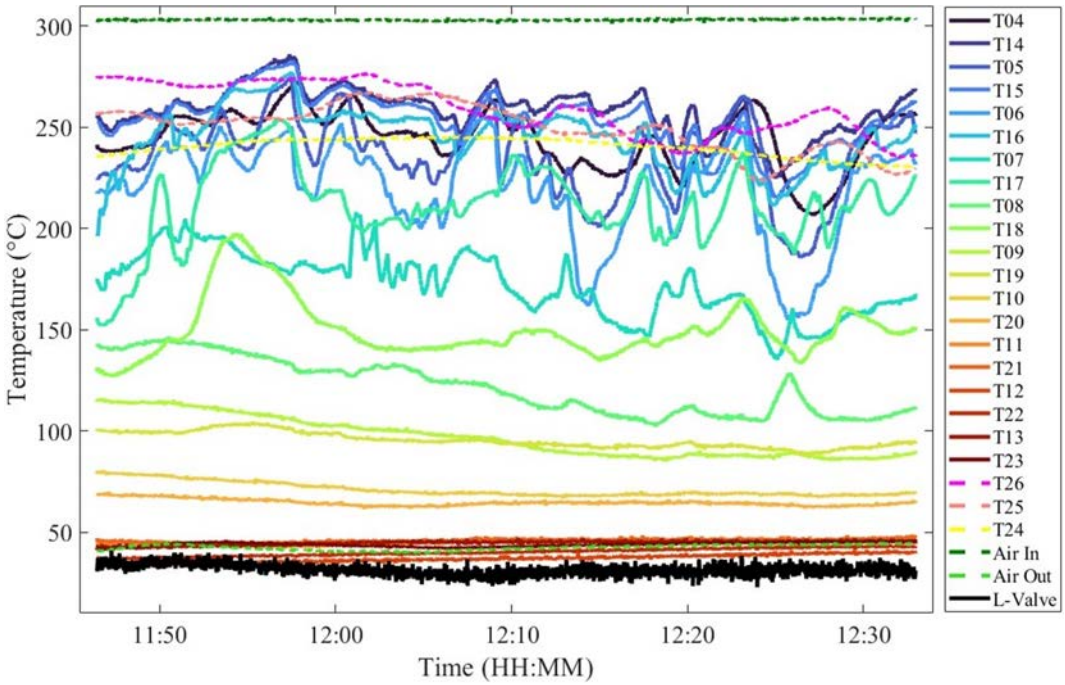

Figure 31. Time series of bed temperature measurement with 825-µm particles at a fluidizing air flow rate of 25 SCFM (14.5 g/s)

An alternative or additional approach to operating an FB HX is to insert baffles within the bed. These will segregate vertical portions, which will limit mixing of the entire bed volume. Ideally, baffles will allow local mixing while maintaining thermal stratification. alludes to increased thermal gradients in the bed when baffles are present. For typical uses of fluid beds (e.g., chemical reactions), this often presents a problem in achieving uniform conditions in the bed. However, for this application, where thermal gradients are desirable, baffles may be beneficial.

2.4 Computational Fluid Dynamics (CFD) Modeling of PFB HX Designs

CFD modeling of the PFB HX can provide opportunities to investigate more design variations, fluidization conditions, and particle size options that would be feasible to vary in the prototype experimental testing. However, multiphase CFD for large domains is a computationally expensive process. To mitigate the computational time and effort, we developed a model of a section of the PFB HX with simplifying assumptions for the CFD analysis. The model was modified by the output obtained from the Ansys Fluent simulations. Figure 32 shows three models used for analysis. The analysis initially started with model (a), a CFD analysis model with air inlets, and faced convergence errors due to the very small air inlet surface areas along with the relatively small flow rate for the system.

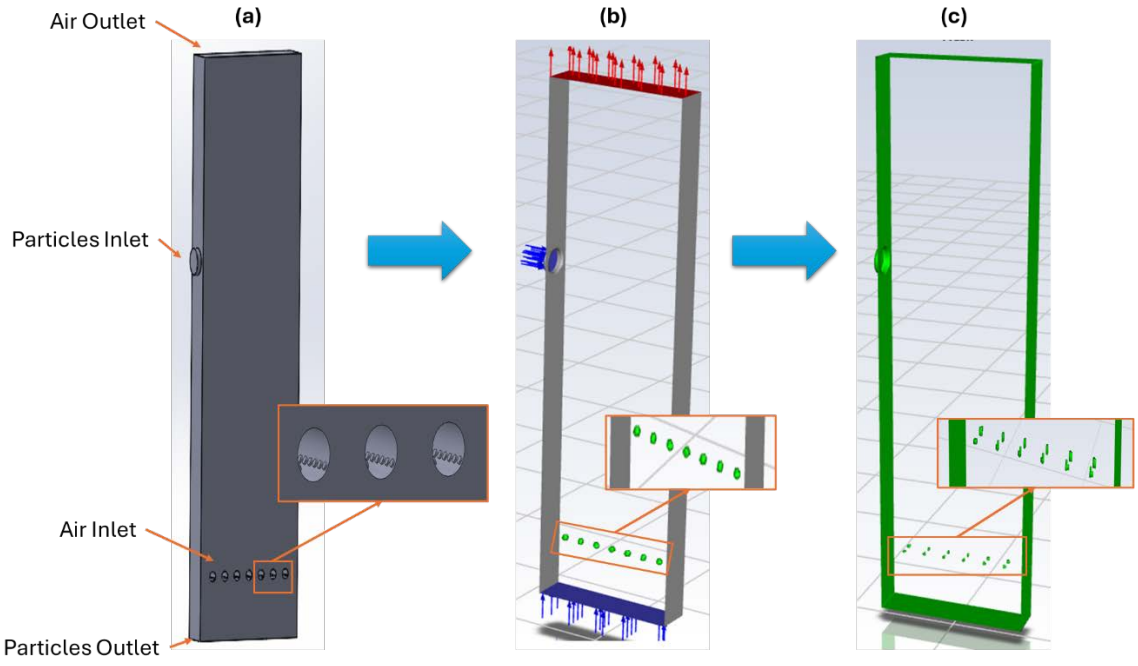

Figure 32. PUMP CFD PFB HX section model

To address the convergence problem, we made model (b), a CFD analysis model with seven air pockets. In this model, the air inlet pockets were generated in Ansys Fluent, which seemed to resolve the convergence problem. Model (c), a CFD analysis model with 12 air pockets, was generated to see the effects of the number and size of the air pockets on the temperature distribution inside the bed. The results generated better temperature profiles with model (c) compared to experimental temperature distribution results. The boundary conditions applied to the system are shown in Figure 33.

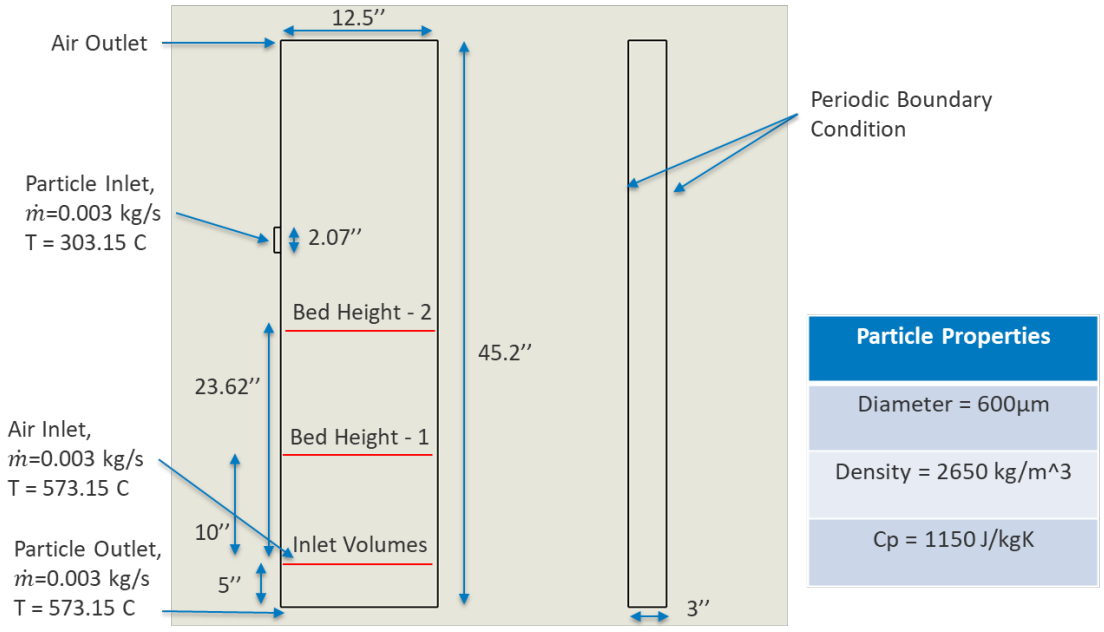

Figure 33. Boundary conditions for the PFB HX section model

The Eulerian approach in Ansys Fluent, a widely used method for simulating fluid bed systems, is used for the current simulations. In this approach, both the solid and fluid phases are treated as the interpenetrating continua. Governing equations (mass, momentum, and energy) are solved for each phase within the shared domain. Semi-empirical formulations for exchange terms govern the transfer of momentum and energy between phases.

The current analysis was carried out using the measured nonlinear temperature profile to initialize the particle domain at the start of the simulations. This nonuniform initial temperature distribution was intended to avoid simulation of the full transient startup conditions such that the simulation could reach pseudo-steady-state conditions in a manageable computational time. The transient temperature profiles are plotted in the comparison plot in Figure 35. Additionally, the flow was considered to be laminar for the simulations due to the low value of the Reynolds number. The nonlinear initial profile of the temperature was taken from the experimental results and set up to vary from 300°C (573 K) near the air distributor to 30°C (303 K) near the initial non-expanded particle bed height (10 in. above the air distributor).

The mesh convergence study, illustrated in Figure 34, indicates a similar particle temperature rise for all mesh densities. Although the meshes exhibited some local temperature deviations near the air distributor region, all three meshes showed smaller differences near the bed height, suggesting mesh independence. Considering the balance between computational cost and solution accuracy, the medium mesh, comprising approximately 0.7 million elements, was deemed sufficient and was used for all subsequent analyses.

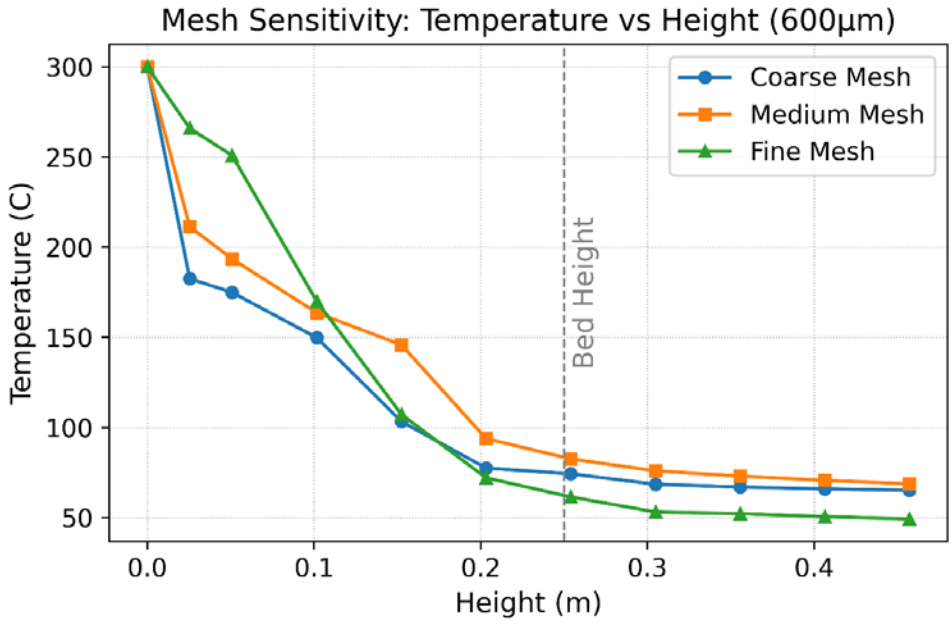

Figure 34. Grid convergence analysis for 600-µm particles (0.25-m bed height)

The results obtained from the CFD simulations are discussed in the section below.

2.5 CFD Model Validation Using Lab-Scale FB HX Test Results

The simulations were set up with planes above and below the distributor to monitor the temperature distribution, pressure, volume fraction, and velocity of the air and particles. Some of this data is shown in this report to discuss the behavior of mixing inside the bed and address any differences from the experimental results. The air distributor is set at 0-m height, and the temperature monitors are set at a 1-in. height difference up to 20-in. height. Figure 35 compares the different model setups. The different models in the plots are named based on the number of air inputs in the domain (7 versus 12), as shown in Figure 32. The boundary conditions are kept the same for all the simulations.

The green line (7 inputs) and the light blue line (12 inputs) show a direct comparison of two cases with the same boundary conditions and constitutive models but different numbers of air inputs. It can be observed from Figure 35 that the simulation with more air inputs shows more mixing inside the bed and presents better agreement with the temperature profile obtained from the experimental results and used to initialize the model (shown as a dashed blue line). The number of air inputs are kept to 12, in keeping with the maximum number that Ansys Fluent allows to be introduced in the fluid domain.

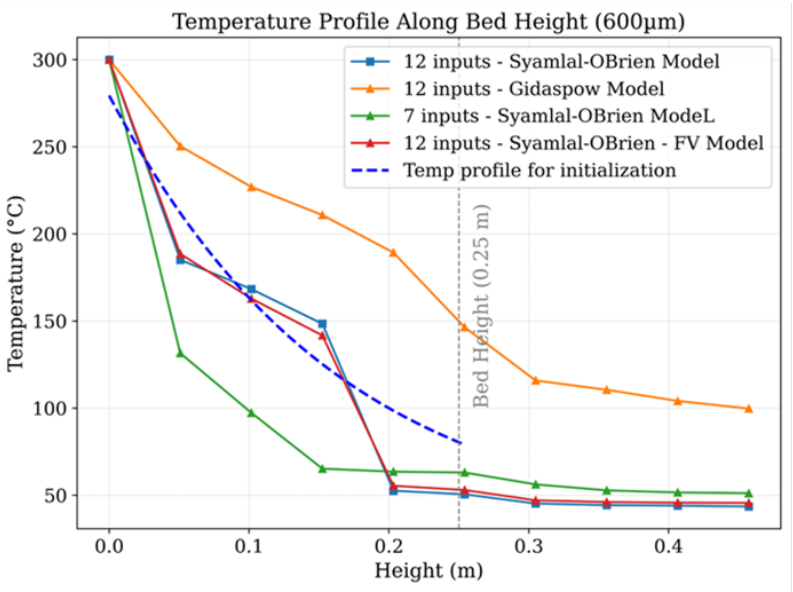

Figure 35. PUMP CFD plots at multiple model settings

We also simulated two other cases: one with the frictional viscosity term enabled and one using the Gidaspow drag model in place of the Syamlal-O'Brien drag model. The "12 inputs - Syamlal-OBrien - FV Model" plot is the simulation with the frictional viscosity term enabled. In the context of Eulerian multiphase models, the frictional viscosity term accounts for the particle frictional stresses that can dominate when the solid phase approaches its maximum packing limit. Regions close to the distributor can become tightly packed and particles are not able to move freely, causing the frictional force between them to generate stress. The frictional viscosity term is used to model that behavior. However, the comparison plot in Figure 35 shows that the simulation results without the frictional viscosity term (light blue line) have temperature values that are close to the simulation results with the frictional viscosity term (red line).

The Syamlal-O'Brien drag model was used for all the initial simulations. Drag models play an important role in governing the momentum exchange between the air and particles, which directly affects the bed behavior. We tested the Gidaspow drag model and compared the results in Figure 35. It can be observed from the "12 inputs - Gidaspow Model" plot (orange line) that the temperature values are significantly different than those in the "12 inputs - Syamlal-O'Brien Model." The Gidaspow model is recommended for dense phase particles, whereas the Syamlal-O'Brien model is commonly used over a wide variety of bed conditions. Further investigation is still being carried out to understand the difference of behavior in the simulations. Multiphase Flow with Interphase Exchanges (MFIX), an open-source multiphase flow simulation software, was also used to simulate the behavior of the fluid bd at a smaller scale. The results are shown in Figure 36. The MFIX simulations were carried out at a much smaller scale to save computational cost, and thus the results are not integrated with the CFD results in the comparison. The MFIX simulations used the linear temperature profile to initialize the analysis, and the temperature result from the MFIX model showed good agreement with the temperature profile.

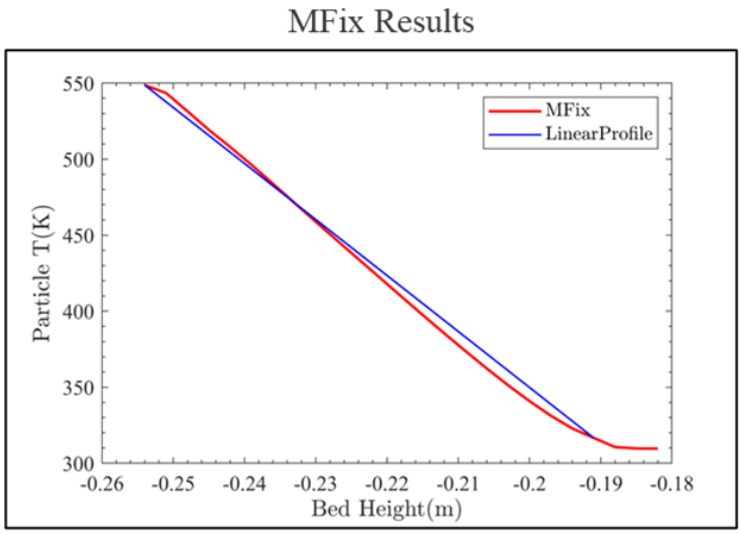

Figure 36. Additional results from Multiphase Flow With Interphase Exchanges (MFIX)

The initial simulations were performed for the 600-µm particles at a bed height of 0.25 m (10 in.), but the simulations for experimental validation for the 600-µm particles were carried out at a bed height of 0.6 m (23.62 in.). Figure 37 shows the plots obtained from the Syamlal-O'Brien and Gidaspow models in comparison to the experimental results.

The percentage errors from the experimental results for the Gidaspow model and the Syamlal-O'Brien model are plotted in Figure 37. The plot shows that overall, the Syamlal-O'Brien model shows better agreement, with percentage errors less than 10% at most locations. The maximum difference is observed in the freeboard region near the air outlet, where the percentage error is around 10%. On the other hand, the Gidaspow model shows a maximum percentage error up to 30%. We carried out further analysis of results among the drag models at different heights to generate a more comprehensive comparison of the performance of the FB HX with different drag models.

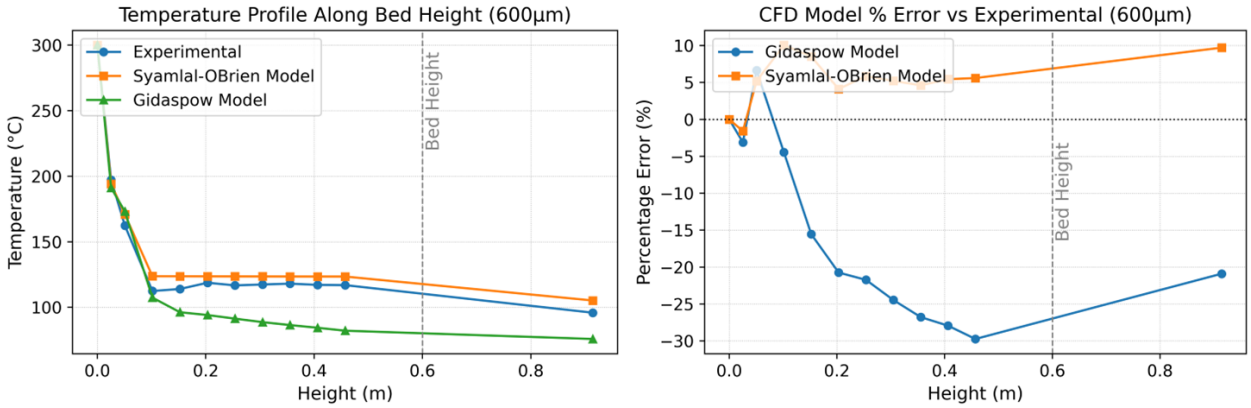

Figure 37. CFD model validation and percentage error with the experimental results

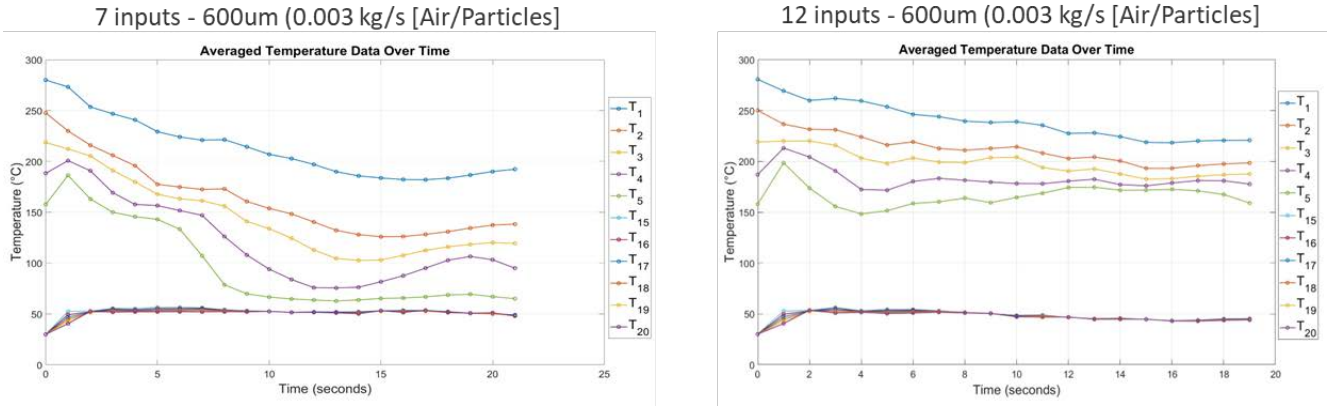

Figure 38. Average temperature values for models with 7 inputs and 12 inputs (both using the Syamlal-O'Brien drag model)

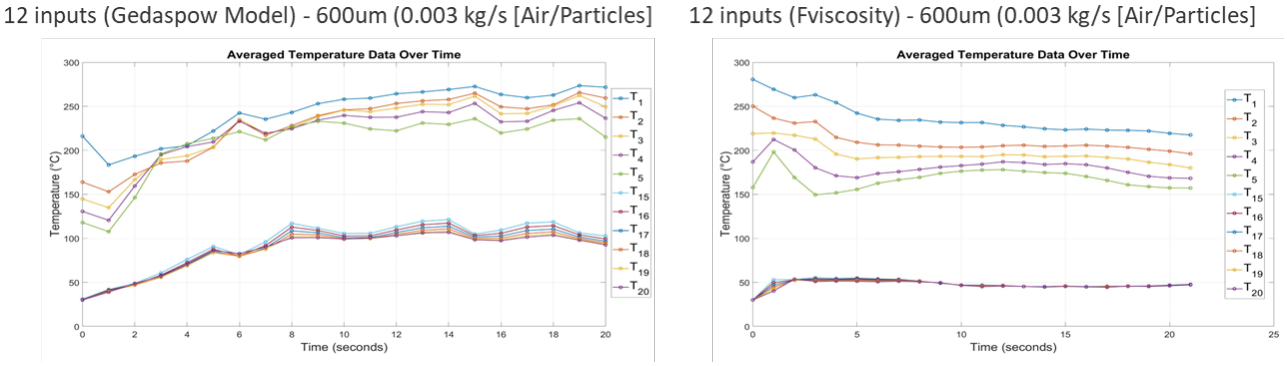

Figure 39. Average temperature values for 7 inputs (Gidaspow model) and 12 inputs (Syamlal-O'Brien model with frictional viscosity)

To understand the behavior of the fluid bed, we plotted the temperature and velocity along the height of the bed for the 600-µm particles from the initial simulations at 0.25-m bed height. The temperature plot is labelled with T_i, referring to the position of the plane monitoring the parameter. The position of planes is set up with reference to the air distributor. T_1 refers to the plane at 1-in. height from the distributor and so on. Figures 38 and 39 show plots for the spatially

averaged values of temperature at a given height position, averaged over a one-second time horizon as the simulations move forward. It can be observed from Figure 39 that the Gidaspow model shows different behavior. It is intended to study the momentum exchange behavior in more detail in context of direct-contact, counterflow FB HXs.

Similarly, the velocity plots shown in Figures 40 and 41 for 7 inputs, 12 inputs, and 12 inputs (frictional viscosity) are similar, whereas the Gidaspow model shows different behavior, with higher maximum velocity and a more uniform velocity distribution over the bed height. The velocity from the model using the Gidaspow correlation ranged from 0.1–0.9 m/s; however, for the rest of the simulations using the Syamlal-O'Brien correlation, the velocity ranges from 0.1–0.6 m/s.

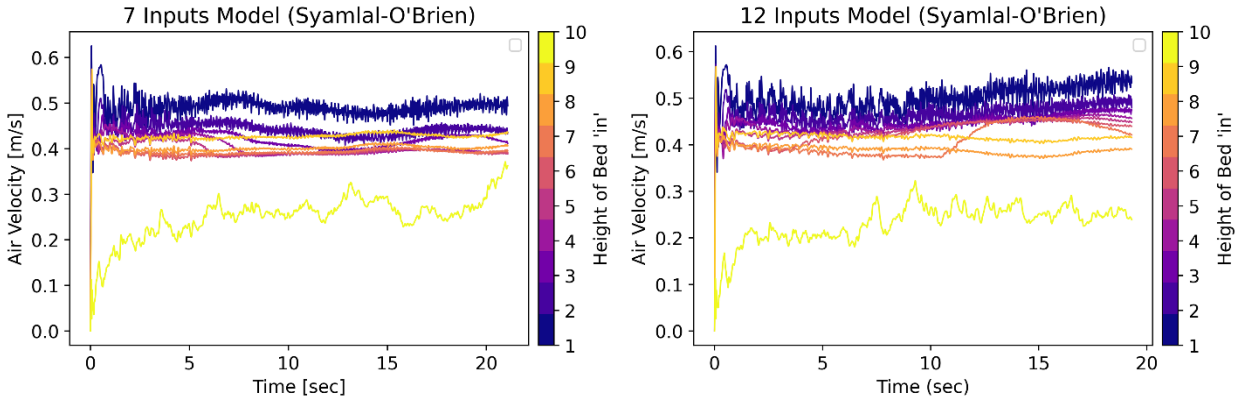

Figure 40. Velocity along the bed height for the 7-input and 12-input models

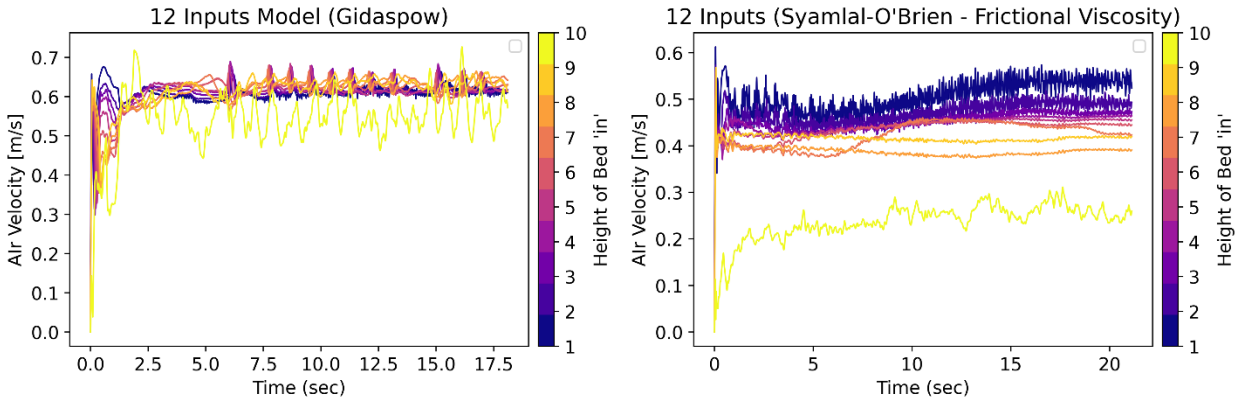

Figure 41. Velocity along the bed height for the 12-input (Gidaspow) model and the 12-input (Syamlal-O'Brien - frictional viscosity) model

Snapshots of the volume fraction contours and the temperature contours are shown in Figures 42 and 43, respectively. The snapshots were taken at approximately 15 seconds for all the presented simulations. The data was obtained at a fixed time for consistency in representing the CFD results.

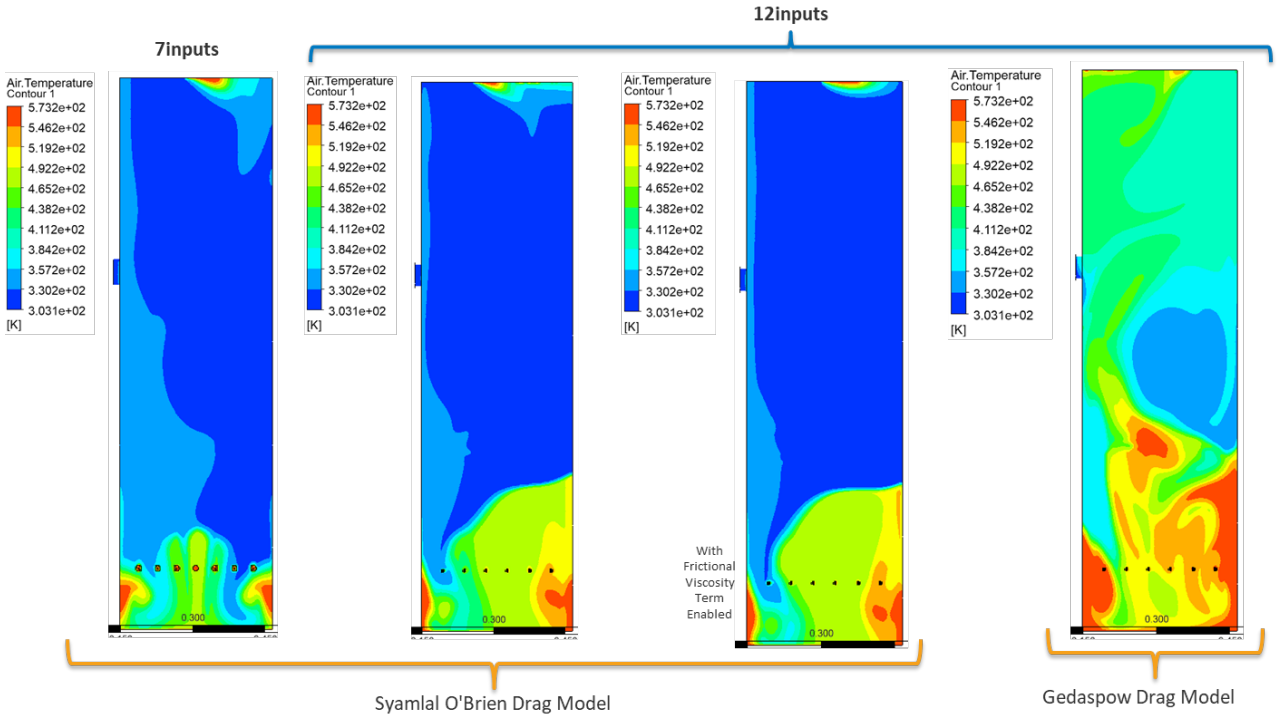

Figure 42. Temperature contours on the plane at 15 seconds

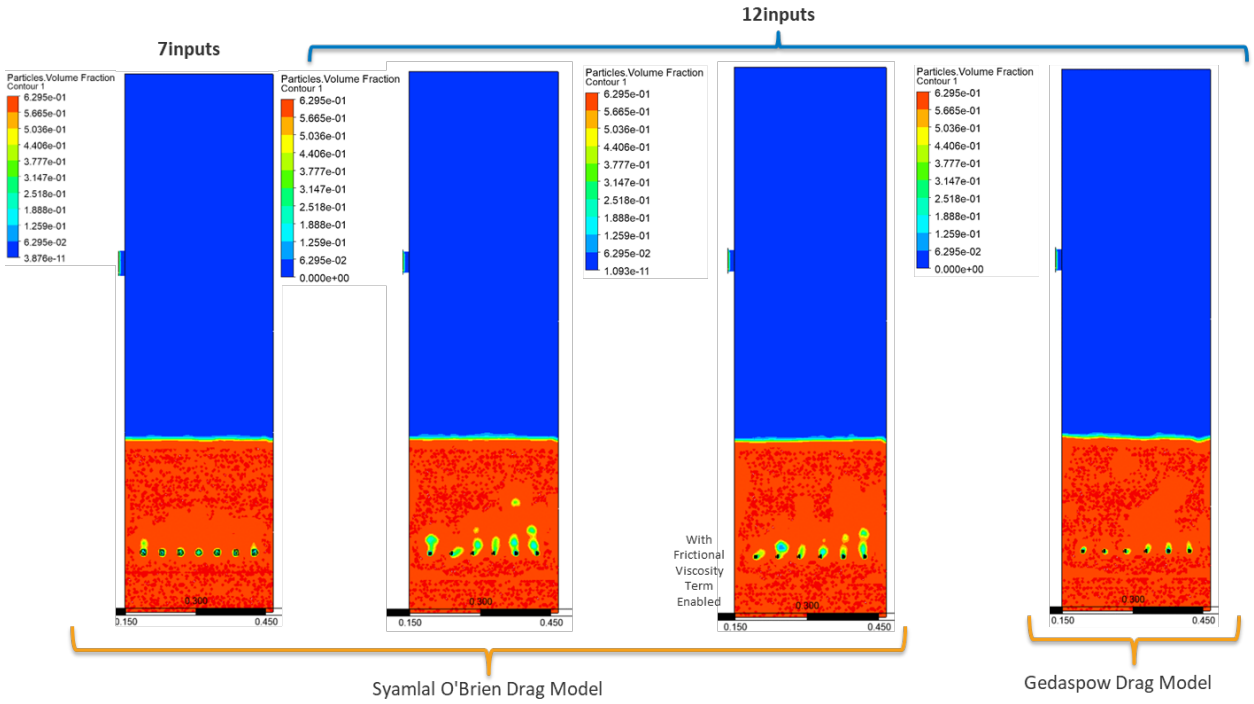

Figure 43. Volume fraction of particles contours on a plane at 15 seconds

Task 2 described P-PTES key components integrated in a system layout and identified FB HX as a major innovative development. We have developed a commercial-scale PFB HX conceptual

design and, based on the unique PFB HX operation principle, designed, fabricated, and tested a laboratory-scale PFB HX prototype. Test station was built with prototype FB HX and particle handling and control including screw feeder, pneumatic lift, and an L-Valve. Experiments have validated the PFB HX operation principles. Prototype development and testing demonstrated the first air/particle direct-contact HX by achieving air-side exit approach temperature <15°C. Modeling of FB HX provides in-depth understanding of the FB HX design, operation, and scaling-up paths. Both modeling and testing of the FB HX has laid the foundation for pilot demonstration and scaling-up of electro-thermal energy storage (ETES) technology using particle TES.

3 Task 3: Evaluate and Integrate Turbomachinery with Particle TES and CSP

Brayton Energy and the NLR team have identified turbomachinery requirements for achieving >55% PTES round-trip efficiency and have defined turbomachinery specifications, components, power capacities, and operating state parameters for integration with P-PTES and hybrid CSP-PTES. Brayton Energy has developed reversible turbomachinery for PTES and its cycle operation conditions. We have quantified the system benefits of reversing turbomachinery integrated within a P-PTES system and performed sensitivity analysis of operation conditions on system/component configuration and performance, including polytropic efficiency, design and technology readiness level, and a preliminary cost comparison.

A commercial-scale, 50-MW_e turbomachinery design developed by Brayton Energy is used as a baseline to provide operating parameters for sizing other components in the system. Turbomachinery performance has a significant impact on PTES design and performance, as shown in the Task 1 discussion. We anticipate that reversing turbomachinery will have significant cost advantages over an MS-PTES system.

3.1 Reversible Turbomachinery Design and Performance

This project leverages Brayton's design of a full-scale, 50-MW_e reversing turbomachine under the ARPA-E DAYS program, which leverages 10 years of PTES development, including collaboration with Google X (now Malta) on separate turbomachinery. The goal of reversing turbomachinery is to use a machine that can operate as both a compressor and a turbine to reduce turbomachinery costs and eliminate large valves and piping.

Figure 44 shows the layout of the Brayton Energy reversing turbomachinery for PTES with relative duct sizes. Motors/generators are split on both ends and are coaxial with turbines. Each machine has a single axis with counter-rotating blades based on aerodynamic designs for streaming air flow with minimum exergy losses.

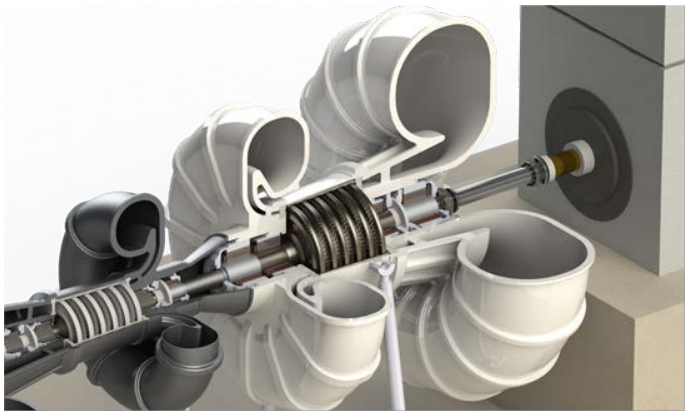

Figure 44. Schematic design of the Brayton Energy reversible turbomachinery for PTES from Brayton's ARPA-E DAYS project. The turbomachine requires large, thick-walled volutes to deliver and receive the flow to the heat sources, such as the NLR FB. This 50-MW_e machine was designed for 5-bar inlet pressure and 15-bar exit pressure.

Image from Brayton Energy Inc.

Turbomachinery aerodynamic analysis was the focus of Brayton's ARPA-E DAYS project. Polytropic efficiencies were estimated using empirical and 3D CFD modeling by Brayton and the Massachusetts Institute of Technology (MIT) Gas Turbine Lab, as listed in Table 7. The table lists the total-total polytropic efficiencies as well as the total-static efficiencies, which incorporate the inevitable decrements associated with the reversing inlet and exit diffusers. These values are used as targets for the NLR PTES program. The table also shows the sensitivity in the round-trip efficiency to small variations in each polytropic efficiency. These turbomachinery efficiencies are used in support of NLR's PTES modeling. The influence of these efficiencies on the round-trip efficiency was explored in sensitivity analyses. Table 7 also shows the impact of reducing each efficiency independently by 1%. It can be seen that the discharging machinery (i.e., the cold compressor and hot turbine) has the most significant influence on the round-trip efficiency.

Table 7. Polytropic Efficiency of the Turbine and Compressor of the Reversing Turbomachinery Developed by Brayton Energy and MIT

Parameters	Polytropic Efficiency, %		η_{RT} Sensitivity	
Machine	Total-total	Total-static	$\Delta\eta_{poly}$, %	$\Delta\eta_{RT}$, points %
Cold compressor	95.2	93.3	-1.0	0.50
Cold turbine	89.9	87.7	-1.0	0.26
Hot compressor	92.7	90.7	-1.0	0.26
Hot turbine	94,2	92.0	-1.0	0.49
Average	93.4	91.5		

Separate turbomachinery with two machines, including two compressors and two turbines, is considered to estimate and compare cost to the Brayton Energy reversing turbomachinery. Table 8 shows the operating conditions used to calculate the cost. The Brayton Energy reversing turbomachinery uses the exact same operating conditions as shown in Table 8, and thus the cost comparison between the separate and reversing turbomachinery is on the same basis.

Table 8. Operating Conditions of the Separate Turbomachinery

Parameters	Unit	Charging Compressor	Charging Turbine	Discharging Compressor	Discharging Turbine
Pressure ratio	-	3.16	3.08	3	2.93
Inlet Temperature	°C	544.85	18.85	-26.15	811.85
Outlet Temperature	°C	836.85	-51.15	78.85	569.85
Inlet Pressure	MPa	0.5	1.51	0.5	1.46
Outlet Pressure	MPa	1.54	0.49	1.5	0.5
Isentropic efficiency	-	0.9	0.9	0.9	0.9
Mass flow rate	kg/s	182	182	296.7	296.7

The thermodynamic efficiencies are not necessarily different for the separate and reversing turbomachinery if their isentropic efficiencies are the same, as the separate turbomachinery can

be designed at the same operating conditions of the reversing one. The mechanical efficiencies can change slightly due to the different configurations, but that should not be significant. In terms of the effects of the turbine and compressor polytropic efficiencies on the overall system performance, we compared the Brayton reversing turbomachinery and the separate turbomachinery. As shown in Table 9, the change in the polytropic efficiencies of the turbines and compressors for both configurations does not significantly affect overall efficiency. In addition, the overall system efficiency difference between the baselines for both configurations is well within the 5% requirement presented in Table 10.

Table 9. Performance Comparison in Terms of the Effects of Turbine and Compressor Polytropic Efficiencies on Overall System Efficiency

Parameters	Baseline	Change Applied	Overall Efficiency Change
Brayton Energy Reversing Turbomachinery Sensitivity Analysis			
Discharging compressor poly eff.	92.0%	-1.0%	-0.81%
Charging compressor poly eff.	91.0%	-1.0%	-0.47%
Discharging turbine poly eff.	92.0%	-1.0%	-0.79%
Charging turbine poly eff.	91.0%	-1.0%	-0.44%
Separate Turbomachinery Performance Sensitivity Analysis			
Discharging compressor poly eff.	92.0%	-1.0%	-0.50%
Charging compressor poly eff.	91.0%	-1.0%	-1.06%
Discharging turbine poly eff.	92.0%	-1.0%	-0.94%
Charging turbine poly eff.	91.0%	-1.0%	-0.17%

The correlations and coefficients used to estimate the separate compressor and turbine costs for the P-PTES system are from Valero and are shown in Equations (24) and (25)[16] . In addition, the Chemical Engineering Plant Cost Index (CEPCI) is used to convert the cost from 1994 to 2022.

$$Z_{AC} = \frac{CEPCI_{2022}}{CEPCI_{1994}}\left(\frac{39.5\dot{m}_a}{0.92-\eta_{AC,isen}}\right)\left(\frac{P_1}{P_2}\right)\ln\left(\frac{P_1}{P_2}\right) \tag{24}$$

$$Z_{GT} = \frac{CEPCI_{2022}}{CEPCI_{1994}}\left(\frac{266.3\dot{m}_a}{0.92-\eta_{AC,isen}}\right)\ln\left(\frac{P_4}{P_5}\right)[1+EXP(0.036T_4-54.4)\,] \tag{25}$$

where Z_{AC} and Z_{GT} are the cost estimates of the compressor and gas turbine, respectively; $\eta_{AC,isen}$ is the isentropic efficiency of the compressor; and $\dot{m}_a$ is the mass flow rate of air. Table 10 shows the cost estimation results. The discharging turbine has a significantly higher cost than other machines, as it operates at the highest temperature with the largest air mass flow rate. The total specific reversing turbomachinery cost from Brayton Energy can be \$450/kW_e less than the cost of the separate turbomachinery, which allows the P-PTES system to achieve low power system cost.

Table 10. Cost Estimation and Performance Comparison Between Brayton Reversible and Separate Turbomachinery

Parameters	Units	Brayton Reversible Turbomachinery for the PUMP System	Separate Turbomachinery Cost Estimation
Total power capacity	MW_e	50	
Air mass flow rate	kg/s	296.7 (Hot Side)/182 (Cold Side)	
Isentropic efficiency of C/T	%	90	
$CEPCI_{1994}$	kPa	381.1	
$CEPCI_{2022}$	%	813	
Charging compressor specific cost	$/$kW_e$	-	71.50
Charging turbine specific cost	$/$kW_e$	-	129.18
Discharging compressor specific cost	$/$kW_e$	-	95.27
Discharging turbine specific cost	$/$kW_e$	-	196.93
Total specific cost	$/$kW_e$	46.87	492.87
Charging Coefficient of Performance (COP) basis	-	2.92	3.00
Discharging efficiency basis	%	21.2	21.01
Overall efficiency basis	%	61.7	63.1

3.2 Cost Estimation and Comparison with Separate Charge/Discharge Turbines

Brayton Energy completed an analysis of the aero geometry derived from its ARPA-E DAYS program and derived turbomachinery costs from a bill of materials (BOM) including both materials and fabrication. The turbomachinery parts were analyzed through thermal-mechanical reliability, and the alloy selections were derived from stress/life cycle analysis. Table 10 shows the BOM and cost breakdown from a cost model prepared by Brayton Energy that was obtained from a engineering consulting firm working with Brayton engineers. The specific cost of the turbomachinery is \$2.343M/50 MW = \$47/kW_e. This shows a significant cost advantage compared to other types of turbines and can be far less than \$100/kW because the counter-rotating reversible turbomachinery configuration saves stators and can work at suitable temperatures without excess blade cooling.

Brayton's scope of work in this project included preparing a cost model for the turbomachinery and system. The results of the cost modeling are summarized in Table 11. This preliminary cost roll-up leaves placeholders for the NLR FB and lock hopper systems. The results presented in Table 11 are derived from a comprehensive Excel workbook delivered to NLR. This cost analysis builds from the BOM for the DAYS turbomachinery and third-party manufacturing reviews by prospective manufacturers.

Additionally, Brayton provided a comparative cost analysis for the so-called state-of-the-art commercial system. Because no such plant has been built, nor have realistic costs been published, Brayton based this work on their comprehensive body of work performed on Google X's early Malta initiative (2014–2019). In this lengthy study, Brayton designed and manufactured HX test articles for molten nitrate salt, hexane cold storage, and recuperators. The turbomachinery designs were the result of detailed aerodynamic, thermal, structural, and mechanical modeling. An attempt was made to apply similar cost forecasting methods for the competing turbomachines, although alloy and labor costs may differ, due to the periods of analysis (2018 versus 2021/2022). The results of the Google X analysis are provided in the cost workbook delivered by Brayton to NLR, for comparison to the proposed reversing turbomachine system with the NLR particle TES.

The results in Table 11 indicate that the PUMP system can significantly reduce the cost of energy capacity (storage costs) and the cost of power capacity (turbomachinery costs).

Table 11. Preliminary Cost Roll-up, Listing Portions Analyzed by Brayton

Parameters	Units	Malta	Brayton Turbomachine	Notes
Power	MW_e	100	50	Brayton cycle data
Duration	h	10	10	
Temperature Difference (DT)	K	290	276	To be updated in the PUMP project
Pressure ratio	-	5.66	3.5	
Turbomachinery rotor and stator count	-	52	22	
Number of turbomachines	-	2	1	
Specific cost (Malta scale)	$/$kW_e$	317.4	46.9	
Piping and ducting (Malta scale)	$/$kW_e$	$141.6	$70.8	
TOTAL Turb & ducting	$/$kW_e$	$459	$118	

Storage costs are reduced primarily because of the low cost of silica sand ($0.93/kWh) compared to liquid storage media, e.g., nitrate salt ($4.92/kWh) and ethanol water mix ($7.47/kWh).

The power capacity cost comparison in Table 11 is not yet complete, as costs of the FB HXs, heat rejection equipment, and ancillary equipment (such as particle transport systems) have yet to be estimated for this system design.

Task 3 evaluated PTES turbomachinery options and compared them with using or modifying power generation at existing CSP plants. System configurations and operational conditions were established based on the reversible turbomachinery developed by Brayton Energy, Comparison of the reversible turbomachinery vs. separate turbomachinery on the techno-economic potential of the system indicating the promising cost and performance benefits from the reversible turbomachinery. However, integration with sand TES and FB HX is not limited to a single power cycle or turbomachinery. The sand TES system can be flexible to serve the needs of thermal

energy storage for any heat storage systems, including cold and hot storage of industry process heat, PTES, single or combined cycles, or Carnot batteries.

4 Task 4: Develop a P-PTES Modeling Tool for Hybridizing PTES With CSP

Task 4 extended the stand-alone P-PTES into a hybridized CSP-PTES system to expand charge energy sources and share storage and a thermal power conversion subsystem. Various hybridization configurations and their performance were studied based on the thermodynamic modeling tools developed in Task 1.

4.1 Hybridization Approaches

PTES and CSP systems have several components in common, such as TES, power cycle, HXs, heat rejection systems, generators, and grid connections. Integrating PTES and CSP may confer advantages such as improved efficiency, reduced component cost, increased energy density, and the possibility for the plant to provide several energy management services and therefore "stack" revenue streams [4] These advantages must be weighed against the additional complexity of designing, constructing, and operating such a hybrid plant. Furthermore, a hybrid CSP-PTES has more geographical constraints than a stand-alone PTES system. There are numerous ways in which these systems can be hybridized. Four categories are:

1. Use a heat pump in a solar thermal system to improve performance or functionality, e.g.:
    A. Upgrade solar heat to higher temperatures to enable higher energy densities and efficiencies of the discharging system.
    B. Create cold storage with a refrigerator and generate electricity by running a heat engine between the solar heat and the cold storage.
    C. Combine both A and B. This system could also deliver heat and cold to thermal loads [17] .
2. Support a PTES system with solar heat:
    A. Increase the temperature of the heat delivered by the heat pump by adding solar heat; see Section 4.1.1.
    B. Simplify the thermal storage system (or reduce storage volumes) by adding solar heat rather than storing energy.
3. Share the hot storage charged by both CSP and PTES, which can operate somewhat independently; see Section 4.1.2.
4. Collocate stand-alone systems. A colocated system may benefit from grid infrastructure, permitting, shared operational staff, and so on.

Previous work investigated the thermodynamic limits of hybrid systems such as 1A–1C and found that these systems have no efficiency advantages when compared with either stand-alone PTES or a stand-alone CSP system [4] That is, the maximum efficiency of a hybrid system when considering the total energy input (electricity plus the exergetic value of solar heat) is the same as the maximum efficiency of stand-alone PTES. Therefore, to achieve competitive technology, hybrid CSP-PTES must achieve economic improvements such as reducing capital investment (by sharing equipment) or enabling the plant to earn revenue from different sources (such as renewable electricity generation and electricity storage).

A concept proposed by Benato [18]upgraded the temperature from a heat pump using an electrical heater. The author described how this system could achieve higher temperatures at lower pressure ratios and therefore reduce the capital cost. The electric-to-electric round-trip efficiency was >9% for maximum temperatures above 750°C. This low round-trip efficiency is partly due to the "unbalanced" storage; the hot storage capacity is increased, but the cold storage capacity is not. Therefore, during discharge, the cold storage is depleted before the hot storage, and the system has a surplus of energy. This extra hot energy can be exploited by either using it directly in a thermal process or converting it to electricity using a bottoming power cycle. One study that used an organic Rankine cycle estimated an electric-to-electric round-trip efficiency of ~47% with maximum temperatures of over 1,000°C [19].

Additional thermal energy could be provided by CSP rather than an electric heater, as investigated by Petrollese et al. in [20]who considered an argon-based Joule-Brayton PTES coupled with packed bed TES. (Argon is a preferable working fluid for packed bed PTES due to its high ratio of specific heat capacities, whereas nitrogen or helium are preferable for liquid storage PTES due to their high conductivity, which improves heat transfer (Farres Antunez, 2019)) The design proposed by [20] could operate independently as PTES, a CSP system, or a hybrid CSP-PTES system where CSP increases the temperature generated by the heat pump. The authors varied the pressure ratio and showed that increasing the pressure ratio increased the second-law round-trip efficiency of the CSP-PTES hybrid: Higher pressure ratios effectively reduced the temperature of rejected heat and led to $\eta_{RT,2} > 60\%$ for a maximum solar temperature of 1,000 K. In subsequent work, the same group investigated the performance of this design under variable solar conditions [22].

Other concepts have proposed integrating PTES into advanced CSP power cycles. For example, supercritical carbon dioxide (sCO_2) recompression cycles use an additional compressor to facilitate efficient recuperation within the cycle [23]. The recompression occurs to gaseous sCO_2 and thus contributes notably to the cycle work input. An innovation proposed in [24] used PTES to generate and store medium-temperature thermal energy in off-peak times. This stored energy was then used to facilitate recuperation rather than using recompressor. A similar concept was described in [25] for a novel hybrid Rankine-Brayton cycle using a propane working fluid. A heat pump was used to create the thermal energy needed for recuperation, and the proposed concept was found to be feasible in the Spanish electricity market under some scenarios.

In this project, two hybrid CSP-PTES systems, "solar top-up" and "dual-mode configuration," are investigated and described below:

- In the "solar top-up" system, solar heat is used to increase the temperatures that are delivered by the Carnot battery charging phase (Category 2 above). The system is then discharged via a topping gas cycle and a bottoming steam cycle to most effectively use all the thermal energy added to the system.

- The "dual-mode configuration" system has two modes of operation: It can provide both renewable power generation (via CSP) and electricity storage services (via PTES) (Category 3 above). Major components are shared between the two systems, thereby reducing costs compared to two stand-alone devices.

A key design feature of the concepts is the use of particle TES. Particles have been developed as a storage material for CSP applications [26,27]. Silica particles have low capital costs and can be operated over a wide temperature range [28]. The particles are stored in insulated concrete silos and are transferred into the containers using insulated skip hoists adapted from the mining industry [29]. Heat is exchanged between particles and the power systems by using PFB HXs[12] Previous work has characterized particle properties, developed handling technologies, and considered economic impacts [30]

Two hybrid concepts that potentially reduce cost and increase value are described in more detail here and are based on a Category 2 system ("solar top-up cycle") and a Category 3 system ("dual-mode cycle").

4.1.1 Solar Top-Up Cycle

Existing heat pumps typically operate at less than 150°C, although historically, this has been due to the lack of a market for higher temperatures. Compressors in gas turbines output gas in the range of 400°C–500°C, which indicates what temperatures a high-temperature heat pump using an existing gas compressor could reach. Previous work has shown that Joule-Brayton Carnot battery round-trip efficiency is improved by maximizing the temperature difference between the hot and cold storage [4,31,32], due to increasing the heat engine efficiency at the expense of reducing the heat pump coefficient of performance. Deployed CSP systems generate temperatures up to 565°C, and higher temperatures in excess of 1,000°C are possible using next-generation technologies under development. CSP provides one way to increase the temperature of hot thermal storage without requiring the development of new heat pump compressor technology.

Figure 45 illustrates a hybrid CSP-PTES system that uses CSP to top up the thermal energy generated by a heat pump. The charging cycle operates in a similar way to the PTES heat pump, except that after the hot FB HX, the hot particles are heated further in a particle receiver by solar irradiance. Cold particle storage is also created by the heat pump. Compared to the PTES concept, the energy capacity of the hot storage is increased and no longer "balances" the energy content of the cold storage. Therefore, the discharging system uses both a gas turbine and a bottoming steam turbine cycle to exploit excess thermal energy. To discharge the system, a Brayton heat engine extracts power from between the hot and cold storage. This waste heat is available at relatively high temperatures and is used to power a bottoming steam cycle, as shown in Figure 45.

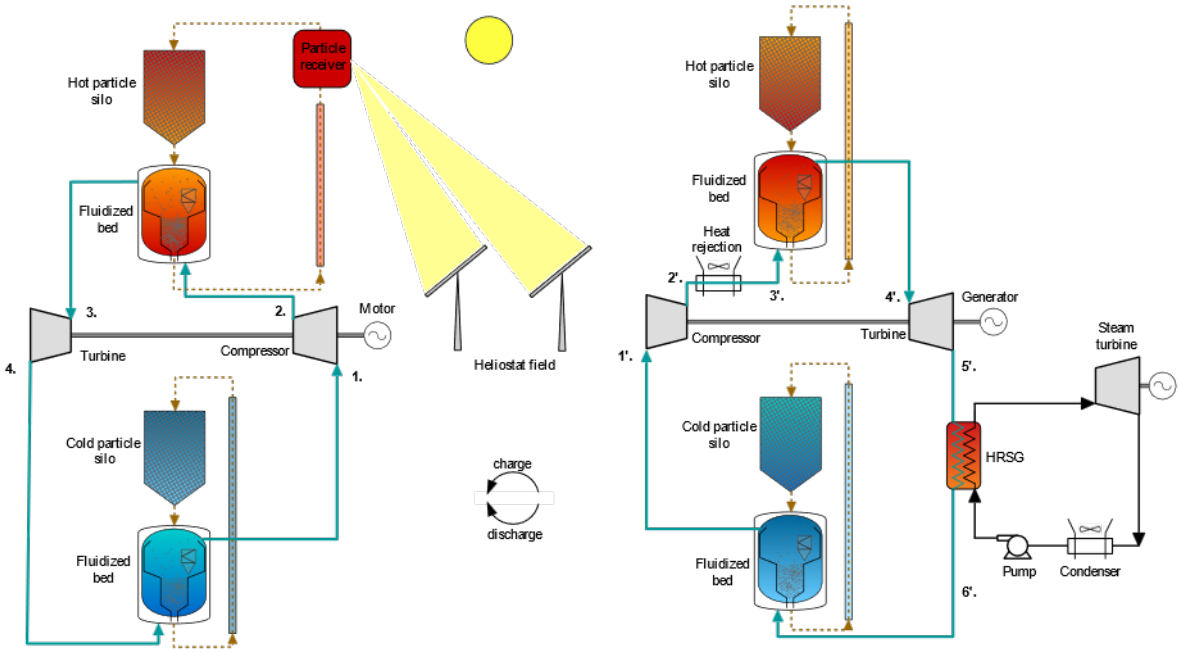

Figure 45. Schematic of the solar top-up hybrid cycle. (Left) During charge, particles are first heated by a heat pump and then solar heat. (Right) The discharge cycle includes a bottoming steam Rankine cycle to make use of excess heat.

Fully charging this system requires both the heat pump and CSP system to have operated—i.e., electricity prices and solar availability have to be favorable for both of the systems to charge. This may not be a problem in locations with a high penetration of solar photovoltaics, such as California, where low electricity prices at off-peak hours coincide with high solar availability. The heat pump and CSP do not have to operate simultaneously but instead could charge at different times, as long as the partially heated particles can be stored. However, the heat pump must operate first to create the right inlet temperature for the CSP field. When discharging the system, the Joule-Brayton heat engine and steam cycle can operate simultaneously to create a larger power output compared to what a stand-alone PTES could achieve. It is also possible to add dispatch flexibility by storing the Brayton cycle's waste heat and operating the steam cycle at another time.

The round-trip efficiency definition in Equation 26 is modified for hybrid cycles to account for the exergetic value (available work) of the solar thermal energy ΔB_s, so that the second-law round-trip efficiency η_{RT} is given by:

$$\eta_{\mathrm{RT},2} = \frac{W_{\mathrm{out}}^{\mathrm{dis}}}{W_{\mathrm{in}}^{\mathrm{chg}} + \Delta B_s} \tag{26}$$

where $\Delta B_s = \Delta Q_s - T_o \Delta S_s$, in which ΔQ_s is the solar heat addition, ΔS_s is the entropy change, and T_o is the ambient temperature.

4.1.2 Dual-Mode Hybrid Cycle

The objective of this configuration is to design a system that can operate independently as a PTES system or a CSP system while sharing several components. Such a system can operate flexibly at reduced cost compared to independent stand-alone systems.

If the CSP and PTES both deliver the same maximum temperature, then the hot thermal storage can be shared between the systems, as long as there is sufficient storage capacity. When the hot storage has been charged by the Carnot Battery, cold storage will have been created, and the system can discharge as a conventional particle Carnot Battery, as illustrated in Figure 4. When the system has been charged by CSP, only hot storage is available. Although this could be used to power a conventional CSP power cycle (such as a steam cycle), the PTES heat engine can be configured to operate using only hot storage, meaning that the same HXs, compressors, and turbines are shared between the CSP discharging mode and PTES discharging mode. To minimize plant complexity and avoid the need for additional piping and valves, during discharge, the cycle working fluid should pass through the same sequence of components in both CSP mode and PTES discharging mode. A heat engine layout that achieves this is shown in Figure 46.

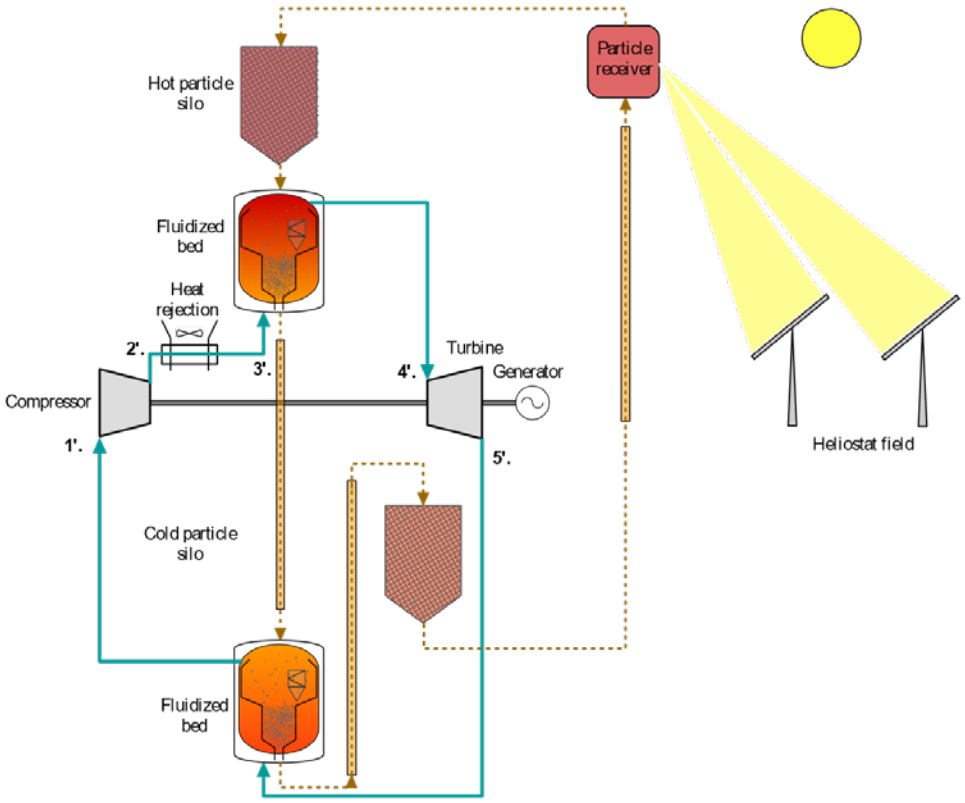

Figure 46. Schematic illustrating a solar thermal heat engine using the same components as the Carnot Battery

The CSP-mode heat engine operates at different operating conditions than the PTES-mode heat engine: Because no cold storage is available, heat is rejected to the environment, and as a result, the discharging compressor inlet temperature is hotter than in PTES mode. Increasing the

compressor inlet temperature requires the off-design performance of the turbomachinery to be considered [33–35] . Because this is a closed cycle, the pressure ratios of the compressor and turbine must be roughly equal. By varying the system pressure, it is possible to find a solution whereby the compressor inlet temperature is increased while the pressure ratios are matched [33–35]. This off-design operation compromises the CSP-mode efficiency to a small extent.

Another feature of the CSP-mode heat engine is the constraint that the working fluid must follow the same sequence of components as in PTES mode. As a result, after the turbine, the working fluid enters the "cold" FB HX, which now operates as a recuperator: Cool particles leaving the hot FB HX are transferred to the cold FB HX, where they are heated by the hot turbine exhaust, before being heated to maximum temperature in the solar receiver. This arrangement requires an extra particle lift to move particles from the hot FB HX to the cold FB HX. The particles now provide recuperation from one side of the cycle to the other, which reduces the temperature range over which solar heat is added to the cycle, therefore improving the heat engine efficiency.

The performance of the system can therefore be defined in terms of the round-trip efficiency η_{RT} of the PTES device (Equation 26) and the heat engine efficiency of the CSP power cycle η_{HE}:

$$\eta_{HE} = \frac{W_{\text{out}}^{\text{dis}}}{Q_{\text{solar}}} \tag{27}$$

where Q_{solar} is the CSP heat absorption by the particle receiver.

4.2 Hybridization Design Modeling

To assess performance, we used a simple thermodynamic model, using the same approach as described in Section 1.1.3, which describes how compressors, expanders, PFB HXs, fans, and pumps are represented. Section 1.1.3 sets out how the thermodynamic state at each point in a PTES cycle is calculated, and how these are used to calculate the energy balance and metrics such as the round-trip efficiency. A similar approach is used for hybrid CSP-PTES systems.[10]

Table 12. Nominal Design Inputs Used for Calculations, Unless Otherwise Stated

Parameter	Units	Value
Gas cycle working fluid	-	Nitrogen
Turbomachinery polytropic efficiency	%	90
Motor-generator efficiency	%	98
Fan efficiency	%	70
Hot HX approach temperature	K	10
Cold HX approach temperature	K	10
Heat rejection approach temperature	K	4
Hot HX pressure loss	%	2.5
Cold HX pressure loss	%	2.5
Heat rejection pressure loss	%	1.0
Charge compressor inlet pressure	bar	5
Steam cycle pump efficiency	%	70
Steam cycle turbine efficiency	%	80
Steam cycle boiler approach temperature	K	25
Steam cycle boiler pressure loss	%	5
Steam cycle maximum pressure	bar	100
Steam cycle maximum temperature	K	873

For the solar top-up hybrid cycle, we modeled a subcritical steam turbine cycle, which comprises a pump, boiler, turbine, and heat rejection equipment. These components were also modeled using polytropic efficiencies, approach temperatures, and pressure loss factors, as detailed in Table 12, and steam properties were calculated using the CoolProp software package.

4.2.1 Solar Top-Up Cycle

An illustrative temperature-entropy diagram of a solar top-up cycle is shown in Figure 47. The heat pump heats particles to a temperature of $T_2 = 750$ K, which is similar to the outlet temperature of gas compressors in simple gas turbine cycles. The particle temperature is then upgraded to $T_s = 1{,}100$ K using solar heat. This particular example has a second-law round-trip efficiency of $\eta_{RT,2} = 61.7\%$ and a specific work output of 301 kJ/kg, 75% of which is produced by the gas cycle, as shown in Table 13.

We compared this nominal design to two stand-alone PTES designs with maximum temperatures of $T_2 = 750$ K and $T_2 = 1{,}100$ K. A stand-alone PTES with $T_2 = 750$ K has a notably lower round-trip efficiency (40.1%) and specific work output (88 kJ/kg) than the solar top-up cycle. Better performance is achieved by increasing the heat pump temperature to $T_2 = 1{,}100$ K, in which case $\eta_{RT} = 60.8\%$. This value is very similar to the solar top-up cycle (it should be noted that neither of these cycles has been optimized) and illustrates that the less complex PTES could be preferable to the hybrid cycle. However, it is notable that the solar top-up cycle generates significantly more work than either of the PTES designs by virtue of the solar heat addition and

bottoming steam cycle. This may help reduce the capital cost per unit power output. Therefore, the hybrid solar top-up cycle is a viable option when power output is a priority, or when solar heat can generate higher temperatures than available compression technology.

Table 13. Comparison of a Solar Top-Up Cycle With Two PTES Designs

Parameters	Units	Solar Top-up	PTES T_2 = 750 K	PTES T_2 = 1,100 K
T_1	K	450	450	800
T_2	K	750	750	1,100
T_s	K	1,100	-	-
Second-law round-trip efficiency	%	61.7	40.7	60.8
Gas cycle specific work	kJ/kg	225.1	88.1	219.3
Steam cycle specific work	kJ/kg	76.2	-	-
Total specific work	kJ/kg	301.3	88.1	219.3

The results in Table 13 indicate that the majority of the power delivered by the hybrid system comes from the Brayton cycle, but that the steam cycle provides an important contribution—about 25%–50% of the total. Without the steam cycle, the system would consume more power during charge than it produces during discharge. Although this is normal for pure electricity storage devices, it does not represent an effective use of solar energy. Therefore, the bottoming steam cycle is necessary to improve the prospects of this system.

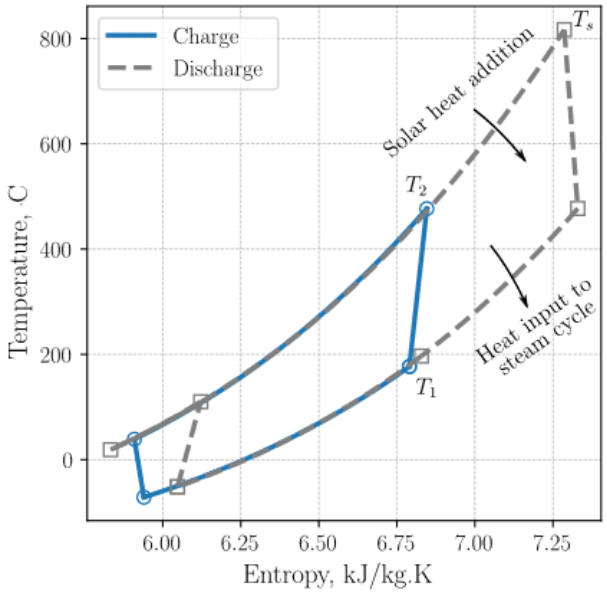

Figure 47. Temperature-entropy diagram for a hybrid CSP-PTES system. The PTES heat pump has a maximum temperature T_2 of 750 K and a compressor inlet temperature T_1 of 450 K. The solar heat is added up to T_s = 1,100 K. The waste heat during discharge is used to power a bottoming steam cycle.

The round-trip efficiency depends on numerous design parameters, such as the pressure ratio, maximum heat pump temperature T_2, and solar heat addition temperature T_s. Figure 48 and

Figure 49 show the second-law round-trip efficiency and specific work output for a range of pressure ratios and solar temperatures. Two values of T_2 are considered: $T_2 = 750$ K represents cycles that could be developed by modifying available gas compressors, and $T_2 = 1{,}100$ K represents cycles that would require specific development of high-temperature compressors. For the round-trip efficiency, an optimal pressure ratio exists and arises for the same reasons as in stand-alone PTES: a trade-off between exergy losses in the HXs and turbomachinery [36] The specific work output increases with the pressure ratio, so a trade-off exists between maximizing efficiency and power output, as is typical with gas cycles. Increasing the solar temperature intuitively leads to higher round-trip efficiencies, although there are diminishing returns as the temperature becomes very high. Particle receivers are being developed to produce temperatures of 1,100 K, and a solar top-up cycle using such a receiver reaches $\eta_{RT,2} > 60\%$.

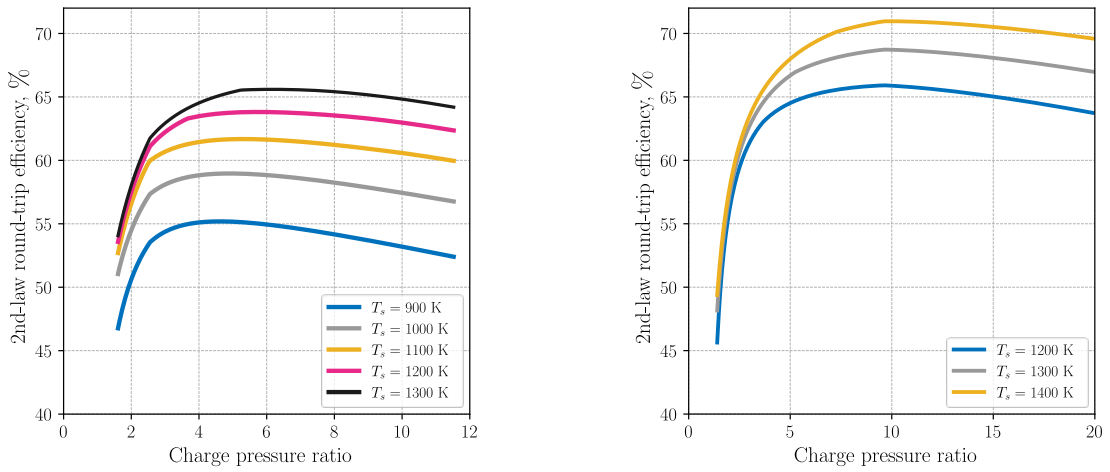

(a) Maximum PTES temperature is 750 K (b) Maximum PTES temperature is 1,100 K

Figure 48. Round-trip efficiency of a solar top-up system as a function of pressure ratio and solar heat addition temperature

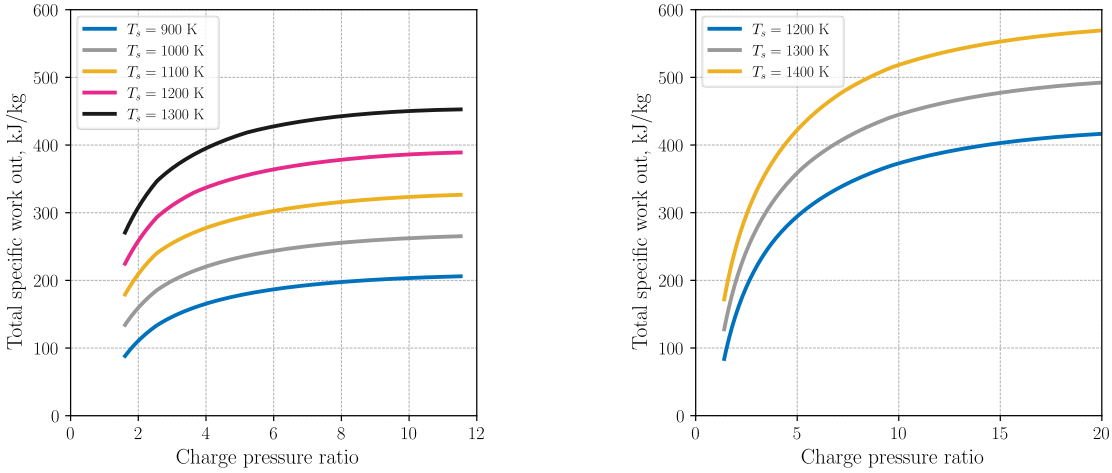

(a) Maximum PTES temperature is 750 K (b) Maximum PTES temperature is 1,100 K

Figure 49. Total specific work output of a solar top-up system as a function of pressure ratio and solar heat addition temperature

Developing solar receivers that can generate higher temperatures can increase the round-trip efficiency further. For example, Figure 48(b) shows the impact of solar temperatures up to 1,400 K for a system with $T_2 = 1{,}100$ K; in this case, efficiencies over 70% can be achieved. Produced results are comparable to those in [20] despite differences in component assumptions and cycle design. For instance, the proposed design includes a bottoming steam cycle to maximize efficiency and power output, whereas the system in [20]did not. The high efficiencies obtained in [20] without a bottoming cycle are most likely attributable to the use of packed bed TES, which can achieve very small approach temperatures. Further work is required to test realistic approach temperatures in FB HXs to see whether the assumed 10 K value can be reduced.

These results are all generated, assuming the FB HXs have approach temperatures of 10 K and pressure losses of 2.5%. Reducing these sources of loss can also significantly increase the performance of the hybrid system.

4.2.2 Dual-Mode Hybrid Cycle

The dual-mode hybrid cycle uses the same set of components (turbomachinery, thermal storage, and HXs) to operate in two different modes: (1) PTES mode and (2) CSP mode. In PTES mode, the system operates the same as a stand-alone PTES, as described in Section 1.1.3: Electricity input drives a heat pump to create hot and cold particle storage. Later, a heat engine runs between the two thermal reservoirs.

In CSP mode, solar thermal energy is used to charge the hot storage to the same temperature as the heat pump ($T_{solar} = T_2$), but sub-ambient cold storage is not created. As a result, the discharge cycle differs slightly from the PTES-mode discharge cycle, as the compressor inlet temperature is warmer and particles are used to recuperate heat within the cycle. The particles and working fluid pass through the components in the same sequence as in PTES mode. Unlike PTES mode, where there are two sets of particles associated with either the hot storage or cold storage, in CSP mode, the particles travel in a continuous loop. The particle temperatures for PTES mode and CSP mode are compared in Table 14. The particles initially leave the particle

receiver having been heated to T_{solar} and are then cooled to just above ambient temperature in the hot FB HX, thereby transferring their heat to the power cycle. The particles are then transferred to the cold FB HX, where they are heated by the hot gas from the turbine exhaust (see Figure 46). This recuperates heat from the thermal cycle, which helps improve its efficiency. The particles then return to the particle receiver to be heated by solar energy.

In CSP mode, the compressor inlet temperature is close to the ambient temperature due to the lack of cold storage, and is therefore considerably warmer than the inlet temperature during PTES mode (which is at sub-ambient temperatures), as illustrated in Table 14 and the temperature-entropy diagrams of Figure 50. We assume that the components are designed for PTES-mode conditions. Therefore, in CSP mode, the compressor operates at off-design conditions. We also assume that the compressor and turbine are on the same shaft and rotate at a constant speed, and that the closed gas cycle requires compressor and turbine pressure ratios to be roughly equal. The hot compressor inlet therefore requires careful management of the CSP-mode power cycle. Previous work in [37] described how these operating constraints can be met while varying the compressor inlet temperature. A strategy known as "inventory control" is employed, whereby the mass of gas in the cycle is varied along with the compressor inlet pressure. These two parameters are varied to keep the volumetric flow through the turbomachines roughly constant, which keeps the turbomachine pressure ratio and efficiency close to the design value. As described in [37] it is possible to adjust the compressor inlet pressure and find an operating point with matched pressure ratios in the compressor and turbine. For the example in Table 14, the compressor inlet pressure reduces, and the cycle pressure ratio increases to accommodate the increased compressor inlet temperature. In this work, the design pressure ratio is set by PTES mode, while an off-design pressure ratio is obtained in CSP mode.

Table 14. Comparison of Temperatures Around the Dual-Mode Cycle in PTES Mode and CSP Mode

Parameters	Units	PTES Mode	CSP Mode
T_1	°C	-17.7	39.0
T_2	°C	110.4	216.2
T_3	°C	19.0	19.0
T_4	°C	807.0	817.0
T_5	°C	547.0	39.0
$T_{in,\ hot\ FBHX}$	°C	817.0	827.0
$T_{out,\ hot\ FBHX}$	°C	29.0	29.0
$T_{in,\ cold\ FBHX}$	°C	-27.7	29.0
$T_{out,\ cold\ FBHX}$	°C	537.0	526.1
T_{solar}	°C	-	827.0
Compressor inlet pressure	bar	5.0	4.1
Expander pressure ratio	-	3.3	3.6
Efficiency	%	59.8	39.1
Specific work output	kJ/kg	164.3	136.4

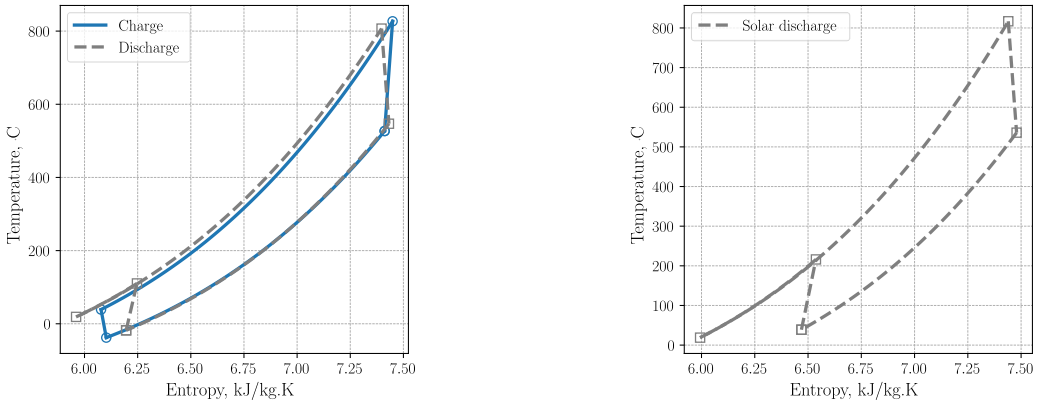

(a) PTES mode (b) CSP mode

Figure 50. Temperature-entropy diagrams of the dual-mode hybrid cycle

PTES mode and CSP mode achieve optimal performance at different operating conditions, and this therefore requires a trade-off between the two modes. For example, Figure 51 illustrates the trade-off between cycle efficiency and specific work output, with the PTES charge pressure ratio being varied along the curves. (The PTES pressure ratio is effectively the design pressure ratio. The CSP-mode performance is then calculated having found the off-design pressure ratio that enables operation.) The figure shows that the efficiency and specific work are optimized at different charge pressure ratios. Furthermore, the optimal PTES-mode round-trip efficiency occurs at a different pressure ratio than the optimal CSP-mode heat engine efficiency—and this is also true for the specific work output.

Choosing a design point will depend on the priorities of individual designs. But it is notable that the curves for CSP mode are relatively steep: Choosing a pressure ratio slightly different to the optimal value leads to a low efficiency and power output. On the other hand, PTES-mode curves have large, flat sections, suggesting that small reductions in PTES-mode performance should be made to achieve reasonable CSP-mode performance. One example is illustrated in Figure 51: A design pressure ratio is chosen to provide the best compromise in efficiency and work output for CSP mode, as shown by the square markers. The corresponding PTES-mode performance for that pressure ratio is shown by circle markers. (This "optimal" pressure ratio is 2.2 for T_2 = 750 K and 2.9 for T_2 = 1,100 K). PTES-mode performance could be improved by increasing the pressure ratio further, but this would lead to a rapid reduction in CSP-mode performance due to the steep curve shapes.

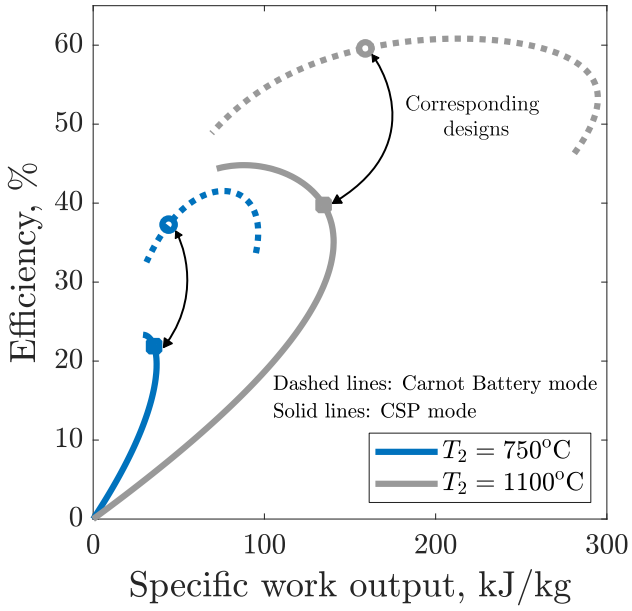

Figure 51. Efficiency and work output of the dual-mode system for two values of T_2. T_{solar} is equal to T_2. The pressure ratio is varied along the curves. The efficiency is the heat engine efficiency for CSP mode and the round-trip efficiency for PTES mode. An optimal pressure ratio is chosen for CSP mode (square markers), and the corresponding PTES-mode performance is indicated at that pressure ratio. Dashed lines show the PTES round-trip efficiency. Solid lines show the CSP heat engine efficiency.

CSP-mode performance is improved by modifying the cycle design. For instance, multiple intercooled discharge compressions reduce the total compression work and therefore increase the efficiency and power output, as explored in [37] . However, this design increases complexity and cost and reduces PTES-mode performance. Another design change is to allow the particle receiver to heat the particles to higher temperatures than the heat pump—i.e., $T_{solar} > T_2$. This solution is feasible because the storage particles can be operated over a large temperature range. In this design, the CSP-mode turbine has a hotter inlet temperature (T_s) than the design inlet temperature, T_2. The inventory control method is used to find a cycle pressure that ensures the compressor and turbine pressure ratios are matched.

The impact of increasing T_2 on system performance is shown in Figure 52. For each value of T_{solar}, T_2 is held constant at either 750 K or 1,100 K, while the design pressure ratio is varied to optimize the CSP-mode performance, as described above. Therefore, in this analysis, PTES-mode performance also varies as a function of this chosen pressure ratio. In this case, Figure 52 shows that increasing T_{solar} improves the efficiency and specific work output of both CSP mode and PTES mode, although PTES-mode results do not vary substantially.

Operating the turbomachinery at off-design conditions in PTES mode may reduce system lifetime and increase maintenance costs. Figure 53(a) shows the design pressure ratio in dashed lines for each value of T_{solar}. The off-design pressure ratio for CSP mode is shown via solid lines, and it can be seen that increasing T_{solar} leads to a larger difference between the design and off-design values. The turbomachinery efficiency is also compromised by off-design operation. Off-design values are provided in Figure 53(b) (the design efficiency is 90%). Compressor

efficiency is the most severely affected and reduces as T_{solar} increases. The turbine efficiency shows a more complex trend.

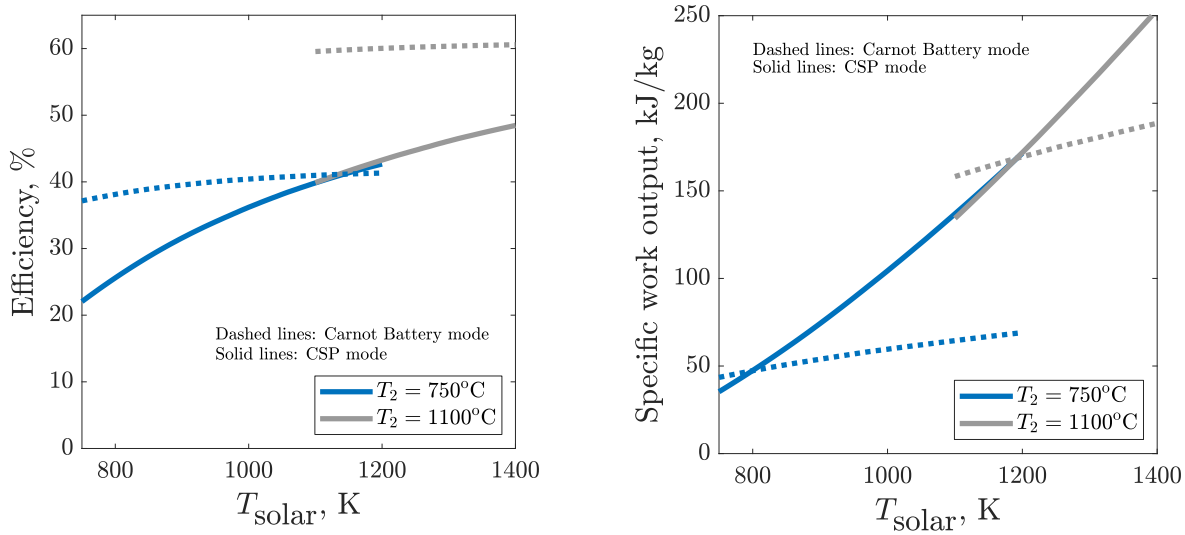

(a) Efficiency (b) Specific work output

Figure 52. Efficiency and work output as a function of T_{solar}. For each T_{solar}, an optimal pressure ratio is chosen, and this affects the performance of the PTES, which is also shown.

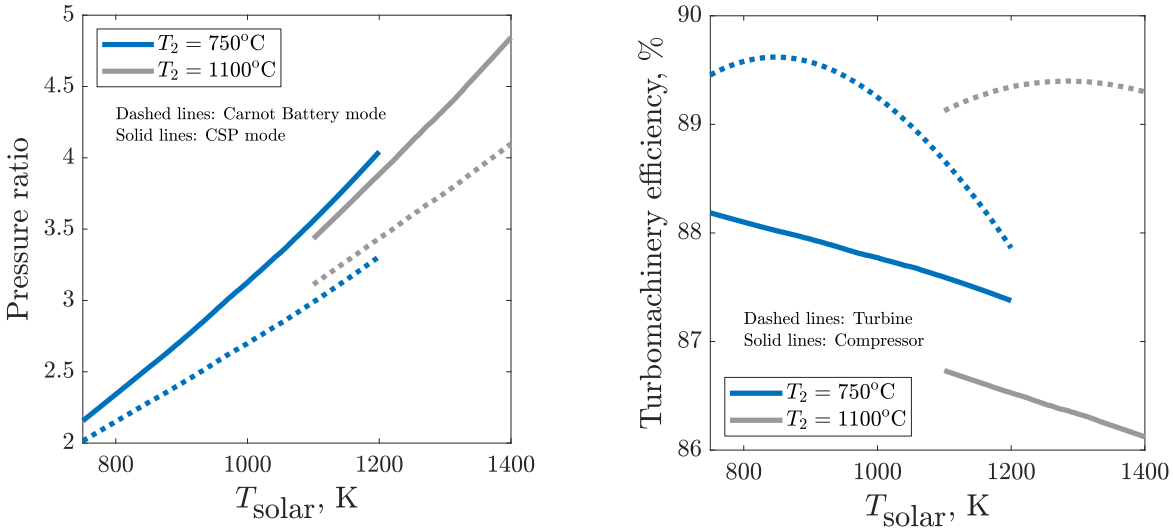

(a) Pressure ratio (b) Turbomachinery efficiency

Figure 53. Pressure ratio and turbomachinery efficiency as a function of T_{solar}.

A sensitivity analysis of the hybrid CSP-PTES system indicates that the sensitivities of CSP operation conditions affect the overall system operation and balance of hot side and cold side stored energy. The results guide system integration and selection of hybridization configuration for performance and cost optimization.

4.3 Modelon-Modelica Modeling of PTES Key Components To Simulate System Performance and Operation

Steady-state modeling helps inform the high-level design and performance of the hybridized and stand-alone PTES systems that have been detailed in this report thus far. To this end, we have built transient component and system models in the Modelon Impact software using Modelica modeling language. Modelica is an object-oriented system modeling language that allows component models to be easily rearranged and reused to model different system configurations. This is useful for the project tasks, as it enables us to explore different system configurations and leverage prior component modeling work.

4.3.1 Component Model Development

We have developed a Modelon-Modelica-based modeling tool to support the stand-alone P-PTES and hybrid CSP-PTES designs. The modeling tool was expanded from a prior particle TES system model developed by the project team. It includes key component modules of particle TES, PFB HX, and so on, and simulates storage system design and performance for PTES and hybrid CSP-PTES. Figure 54 shows the component models and program structure of PTES system integration. The modeling tool consists of four component model modules: particle TES, PFB HX, reversible turbomachinery, and solar receiver. Some of these component models leveraged past work and used similar modeling and validation approaches from prior projects. However, unlike the Modelica model development in other projects, the PUMP modeling tool emphasizes CSP-PTES system hybridization, annual operation, and design optimization.

The first step was to develop and validate the library of key components. This work leverages relevant projects, including Brayton's existing turbomachinery modeling approaches, NLR SETO PTES, and the ARPA-E DAYS project ENDURING system Modelon model.

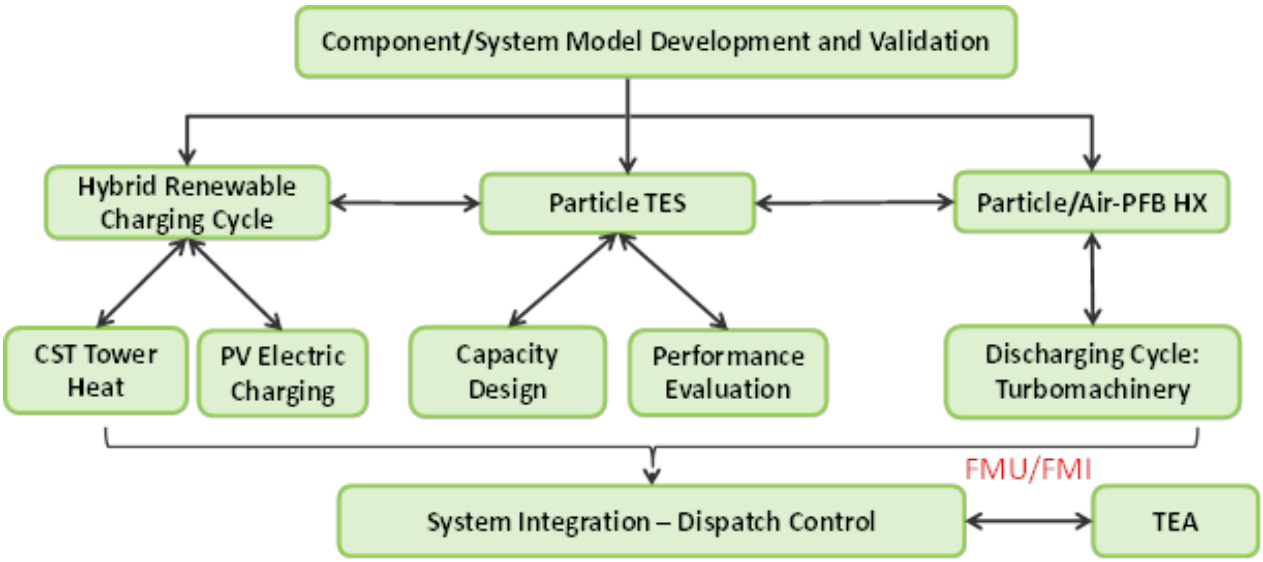

Figure 54. Block diagram of Modelon-Modelica component and system model development

In Figure 54, FMU and FMI stand for functional module unit and functional module interface, respectively. They provide representative performance models and interfaces for integrated

system modeling. Currently, the system performance model in Modelon is separate from the TEA model in MATLAB, besides the thermodynamic cycle model performed in MATLAB.

Table 15 lists the components along with a snapshot of the Modelon Impact-based model, a brief mathematical description of the model, the high-fidelity model or data source that serves as the benchmark against which the Modelon Impact-based models are validated, and the specific metric of comparison for validation. The specific metrics for each component were chosen to represent key outputs of the model that impact overall system performance. The four major component models of the PTES cycle (particle storage, PFB HX, compressor, and turbine/expander) have been validated against high-fidelity models on key metrics. A simple particle receiver model (based on receiver performance correlations from prior DOE-funded projects) was also built as part of a concurrent project. These component models were then used to create the integrated system model along with miscellaneous components (e.g., valves, skip hoist, piping) in Modelon Impact.

Table 15. Key Component Models Developed in Modelon Impact and Validation Plan

Component	Modelon Impact Model	Mathematical Description	Benchmark/ Metric
1. Particle storage silo	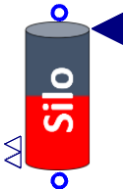	Homogeneous tank model with transient thermal resistance network	FEA/particle temperature over time
2. Reversible PFB HX	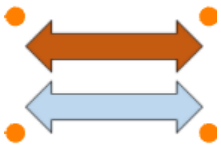	Approach temperatures or counter-flow heat exchanger model, Ergun equation and correlations for gas-phase pressure drop	CFD/bed pressure drop and gas-phase exit temperature
3. and 4. Reversible turbomachinery	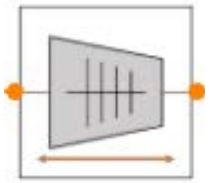	Simple turbine/compressor model with constant isentropic mechanical efficiencies	Brayton data/gas cycle state points and power output
5. Particle solar receiver	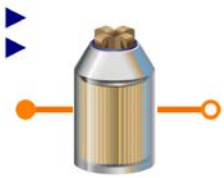	0D, flat-plate receiver with correction correlations from prior DOE projects	SolarPILOT™ Solar field and receiver analysis

Some of the component models in Table 15 have been validated against high-fidelity Finite Element Analysis (FEA) and CFD model or testing data and described in the ARPA-E ENDURING project[13]. Here, we leveraged the existing component models with updated operation conditions and added a particle solar receiver model.

4.3.2 Stand-Alone and Hybrid Modelon/Modelica Model Overview

We built both a stand-alone PTES system model and a hybridized CSP-PTES system model using the dual/parallel charging configuration. In the chosen CSP-PTES configuration, shown in Figure 55, the system can asynchronously or simultaneously charge the hot side of the TES using input electricity or the solar receiver. The system can discharge using the standard PTES heat engine or, if no cold storage is available, through a traditional thermal power cycle. The additional charging and discharging options required a more sophisticated controller to be developed (see Section 4.2). The system model also required an alternative option for discharging without cold storage. The hybrid model currently includes an air-air HX to extract thermal energy from the air working fluid using ambient air, mimicking a power cycle. The system model can then convert the thermal energy extracted to electrical energy through an efficiency parameter. Additional fidelity in the discharging power cycle performance and behavior can be added as information becomes available.

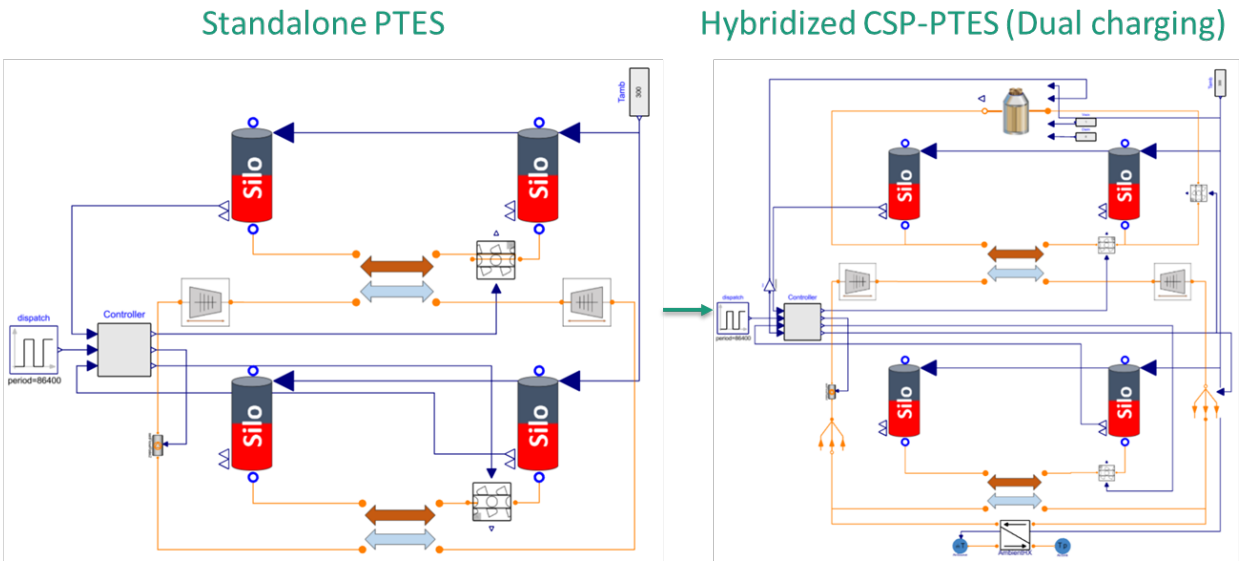

Figure 55. Stand-alone versus hybridized CSP-PTES (dual charging) Modelon Impact models

4.3.3 Hybrid Supervisory Controller

These system models require system control unique to the stand-alone and hybridized systems that operate the components (e.g., turn skip hoists on and off) based on a dispatch signal and other system state points. The dispatch signal is a time-varying signal defined by the user and can be informed by a separate dispatch optimization study or grid prices. The controller designed in Figure 56 reflects the integration of a concentrated solar particle receiver module into the PUMP system. The receiver module is operated based on the solar flux direct normal irradiation (DNI) data in the model and the availability of particle storage governed by the silo levels. Based on adequate DNI data, the controller will govern the mass flow rates through the solar receiver module.

The controller determines whether storage levels are congruent with the dispatch signal, and if the desired dispatch signal is met, the controller sets particle and air mass flow rates. The mass

flow rates are currently based on the controller's nominal charging and discharging parameters, defined by the user.

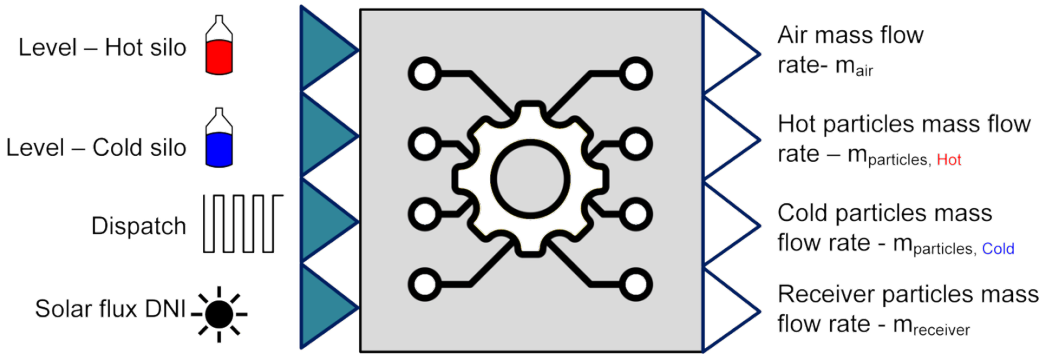

Figure 56. Controller design with inputs (on left) and outputs (on right). The controller regulates the flow rate and module operation based on DNI conditions, levels of silos, and dispatch signals.

4.3.4 System Modeling of CSP-PTES System in Modelica/Modelon

The hybrid system model was tested to ensure it could operate in all the various modes, meaning that the same system model can simulate different modes with simple changes to controller signals (e.g., mass flow rates/direction, valve positions). Figure 57 shows the hybrid system operating in parallel charging mode, where both electricity and thermal energy are being added to the system.

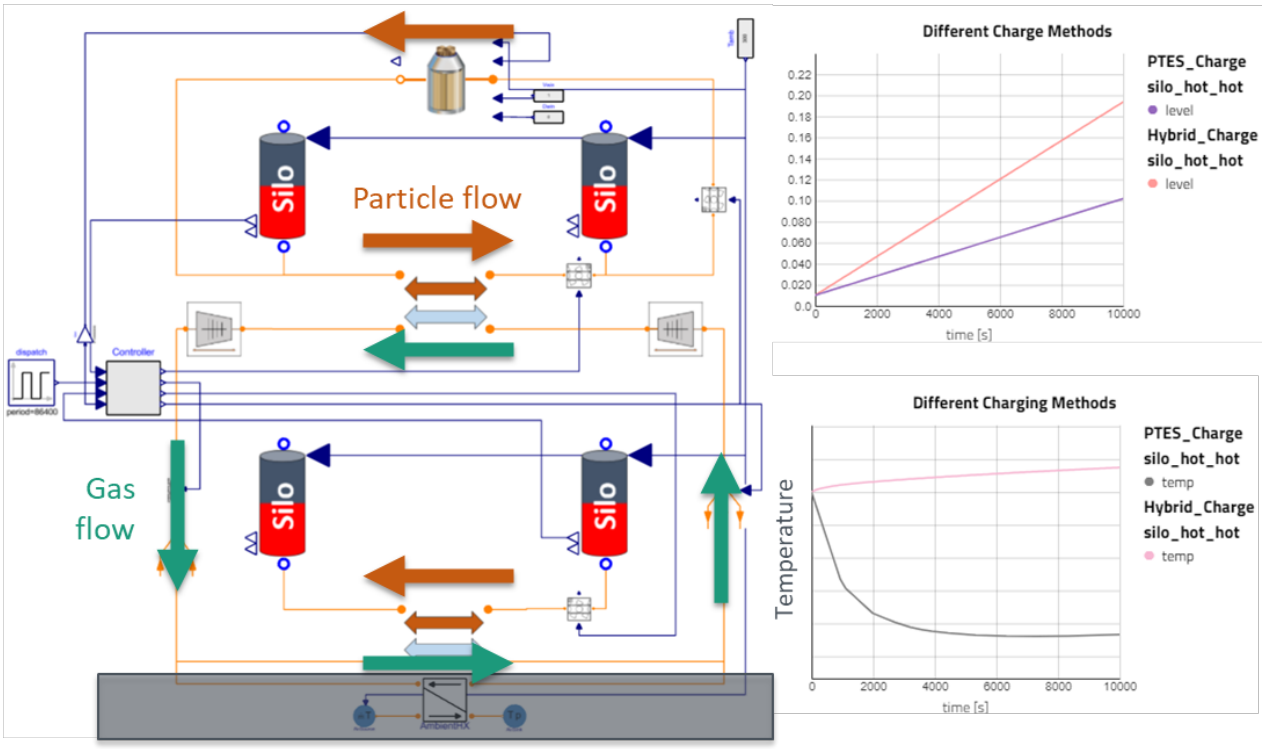

Figure 57. Hybrid CSP-PTES operating in parallel charging mode. Results on the right include results from parallel charging mode and stand-alone PTES charging mode (i.e., no solar thermal).

The plots on the right of Figure 57 show outputs for the parallel/dual charging operation compared to the stand-alone PTES charging mode. The top figure shows that the hot side hot silo is being filled faster in parallel charging mode than in stand-alone mode due to particles flowing through both the hot side HX and the solar receiver. Parallel charging does create an imbalance in the quantity of hot storage versus cold storage in the PTES cycle. Therefore, the integrated system model has the ability to discharge solely from the hot storage silos through a separate thermal power cycle to rebalance the hot and cold sides. This discharging process is less efficient than discharging using the PTES cycle because the cold sink is now an ambient condition; this operating mode is demonstrated in Figure 58.

At the particle mass flow rates used in the test example in Figure 58, the solar receiver initially outputs higher temperatures than the heat pump, and this leads to different hot side hot storage temperatures (lower-right figure). This discrepancy can be resolved by implementing component-level controllers to ensure that design points are maintained, meaning each charge pathway should yield a similar temperature into the hot side hot silo. In this example, this could be done by increasing the flow of particles through the receiver to match the outlet temperature of the heat pump or throttling the particle flow rate through the hot side HX to increase its outlet temperature to match the receiver outlet temperature.

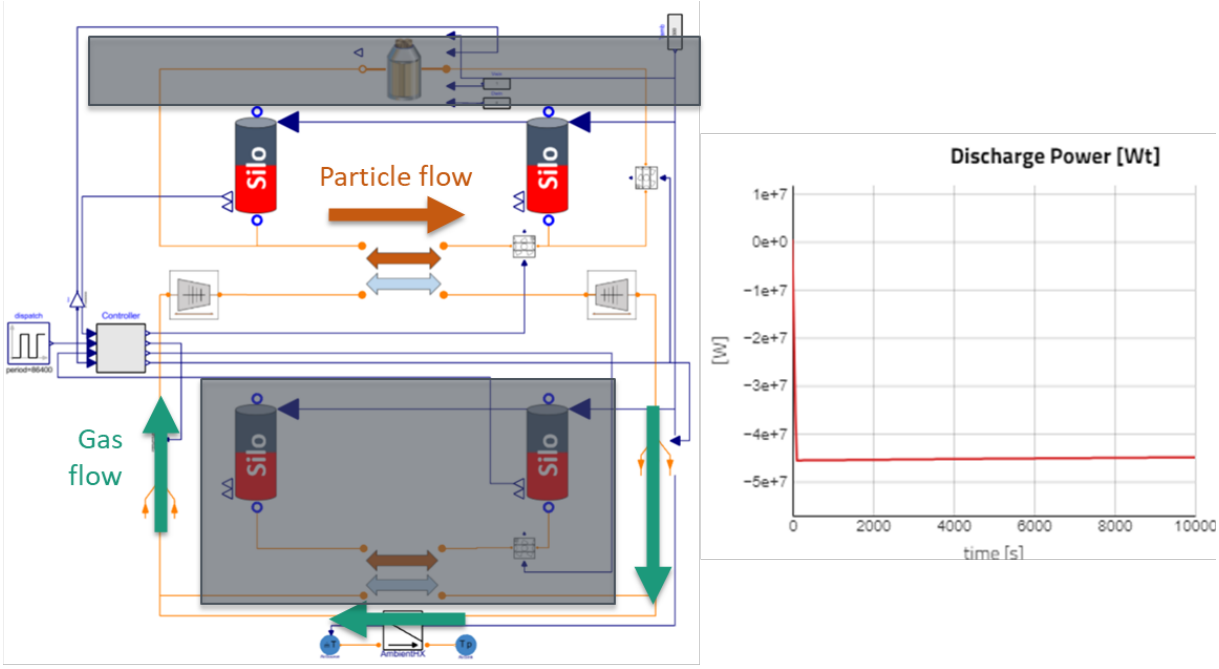

Figure 58. Hybrid CSP-PTES system model operating in hot side stand-alone discharge

4.3.5 Feedback Control Modeling and Charging/Discharging Behaviors

A feedback controller was implemented to control the exit temperature of the particles in the solar receiver by varying the mass flow rate from the receiver such that the particles entering the hot side's hot silo are at the same temperature as those being heated by the heat pump cycle. The feedback controller uses the traditional proportional-integral-derivative (PID) controller, which uses proportional, integral, and derivative action to provide the set output. A block diagram of the standard PID controller is shown in Figure 59.

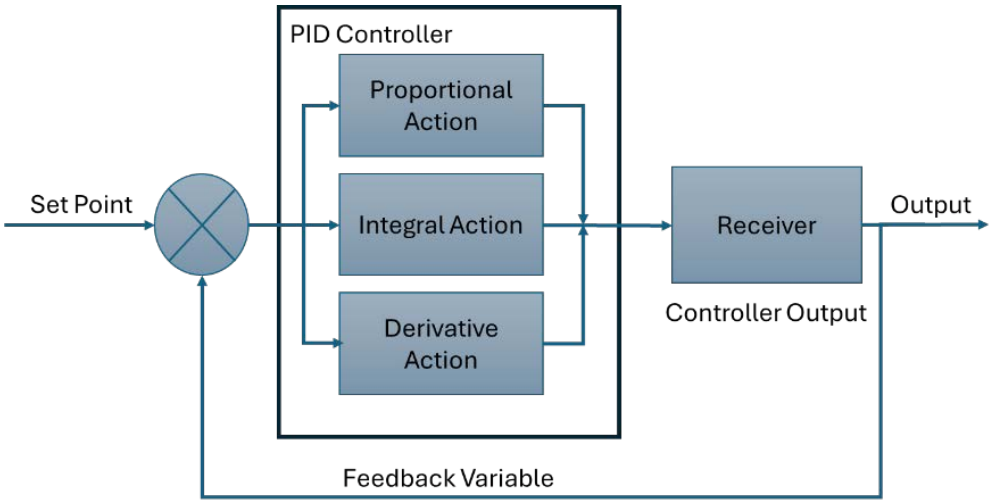

Figure 59. PID controller block diagram

The feedback controller is added to the existing system architecture such that it controls the mass flow rate to the skip hoist that provides the particles to the receiver. Figure 60 shows the feedback controller in addition to the receiver.

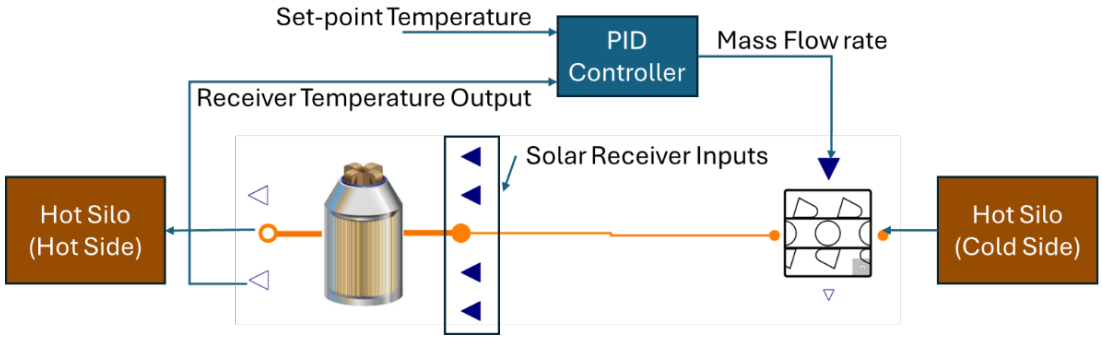

Figure 60. Feedback control loop with skip hoist

The addition of the feedback controller enabled the system to control the exit temperature of the particles from the receiver, enabling a more stable charging phase of the system. After a certain threshold value, the fluctuation in the solar heat flux will not affect the intended charging or discharging time of the system. The PID controller requires the input parameters, including the gain k, time constant for integral block T_i, and time constant for derivative block T_d. One way to identify these parameters is through trial and error until the desired results are achieved, but Modelon Impact provides an autotuner for the PID controller to obtain these parameters. The autotune obtains the parameters based on a relay experiment. It then uses the Approximate M-Constrained Integral Gain Optimization (AMIGO) tuning rules to obtain the control parameters [1]. The autotune is connected the same way as the PID controller, as shown in Figure 60, and can be connected to a single input and single output process. We start the experiment by ensuring that the process is in a steady-state condition. The experiment is then followed by a verification step to obtain the PID parameters. Once these parameters are identified, the autotune is replaced with the PID controller with the input parameter values obtained. The PID might need to be autotuned every time for a different system scale. The hybrid system with the receiver and feedback controller is shown in Figure 61.

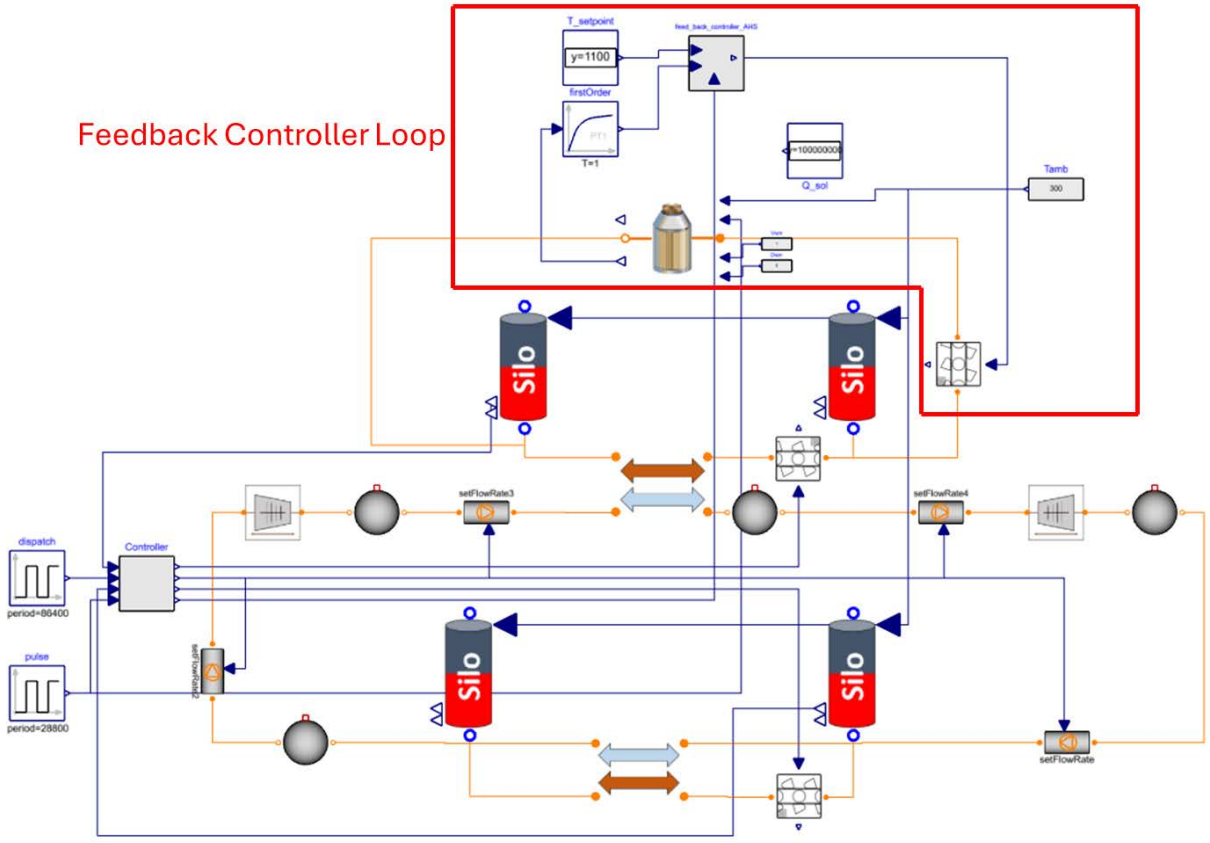

Figure 61. System design with feedback control loop

The feedback controller loop is highlighted with the red block. The results obtained are shown in Figure 62. Figure 62(a) and (c) show the dispatch signal and notional solar radiation signal sent to the system controller and receiver. Figure 62(d) and (c) show the receiver output temperature controlled by the feedback controller and the adjusted mass flow rate going through the receiver accordingly. Figure 62 shows that when the dispatch signal is at 1 and the system is charging, the feedback controller controls the receiver temperature to 1,100 K, which is the provided set point to the controller. The mass flow rate from the receiver is also adjusted according to the temperature and drops to minimum value when the dispatch is at -1—meaning the dispatch signal desires the system to discharge. The minimum mass flow rate value is set to 1e-6 kg/s to avoid unwanted system fluctuations and/or numerical instability due to divide-by-zero errors.

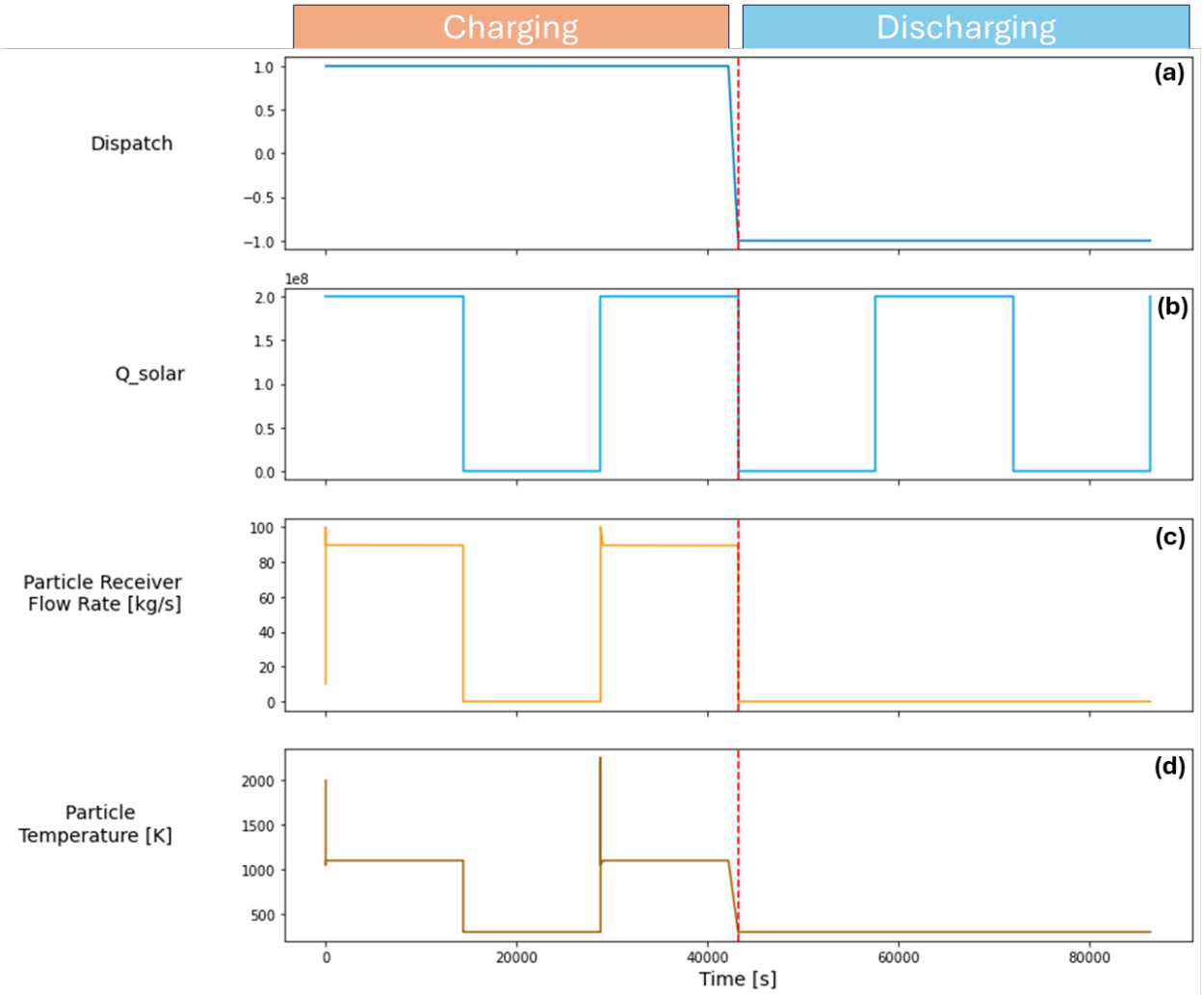

Figure 62. System outputs: (a) dispatch signal, (b) CSP (Q_solar) input, (c) temperature output from the solar receiver, and (d) mass flow rate from the solar receiver

Figure 63 below shows the comparison between the receiver output temperature and the mass flow rate from the receiver. Figure 63 shows that the temperature is higher depending on the solar radiation (Q_sol) input and a notional, fixed mass flow rate of 100 kg/s set by the hybrid system controller.

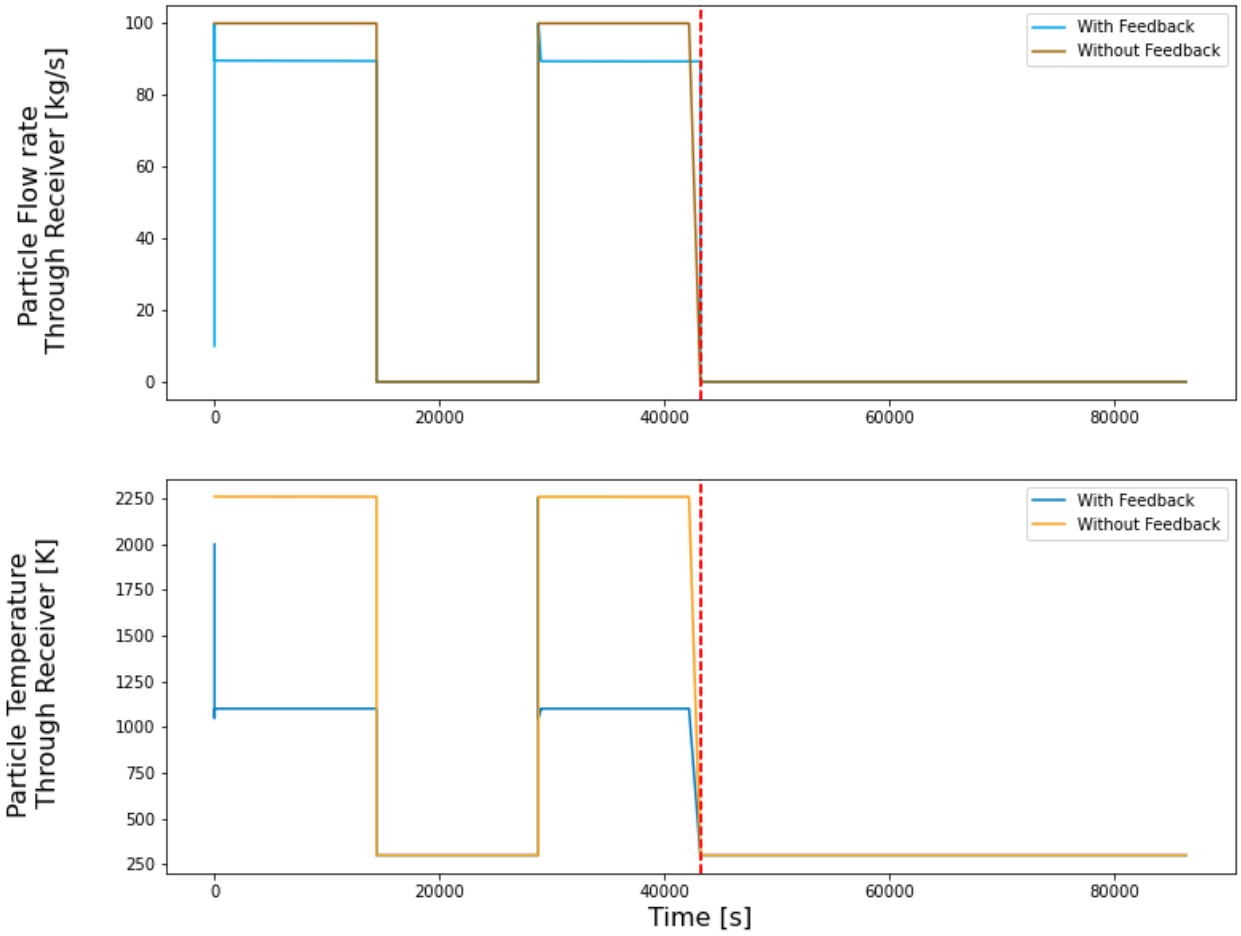

Figure 63. Comparison of system outputs with and without feedback control loop

4.3.6 Open Cycle Integration

The hot and cold side tank levels are plotted in Figure 64 to show the system behavior during the charging and the discharging process. The graphs are obtained from the system shown in Figure 61.

Figure 64 shows the imbalance between the hot and cold side tank levels and their rate of charge/discharge. The parallel charging configuration (i.e., simultaneous PTES and CSP charging) leads to this imbalance. The PTES system charges the hot and cold side equally, but the CSP system only charges the hot side. Therefore, during discharge, when only the PTES system is operating, the cold side is fully discharged before the hot side. To address this problem, an open cycle has been added to the system so that the hot side can continue to discharge completely through the open cycle while leaving the cold side in standby. This discharge state has a lower discharge efficiency because the heat sink in the open cycle is now in an ambient condition as opposed to the sub-ambient temperatures of the cold side. The difference in cold and hot storage capacities makes it necessary to rebalance the hot and cold storages of the system in power generation mode.

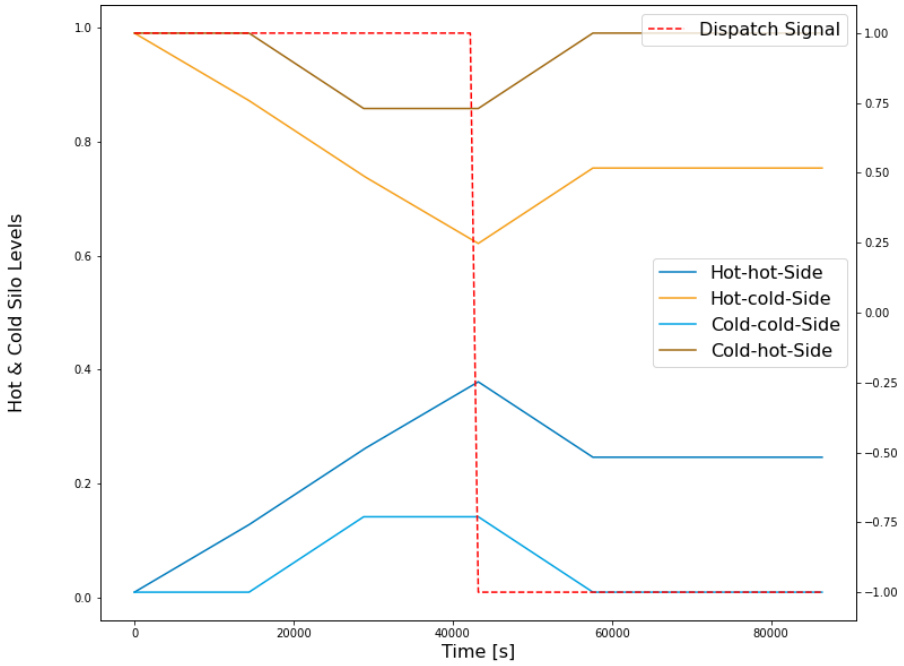

Figure 64. Hot and cold side silo levels during charging and discharging process

In summary, Task 4 developed two hybrid CSP-PTES configurations using the particle TES and compared the performance and operation modes for these two configurations. The potential benefits of hybridizing CSP-PTES were explored with storage cycle efficiency analysis. The team also developed Modelon-Modelica system models and control algorithms based on transient simulations.

5 Task 5: TEA and Technology Transition

With the FB HX feasibility proven in Section 2 and system integration discussed in prior sections, Task 5 focuses on the remaining issues related to P-PTES system operation and techno-economic assessment. We evaluated the risk of cold storage using sand with ambient moisture and recommended a method of moisture removal to avoid freezing sand at sub-ambient conditions. We developed a comprehensive TEA incorporating component cost functions and applied it to analyze the LCOS of the P-PTES technology.

5.1 Investigate Methods to Remove Moisture or Water Content from Gas/Particles

The results in prior sections presume that the particle media is used not only for hot storage, but also for cold storage. This is believed to be an advantage of the P-PTES system, as it eliminates the need for expensive and/or hazardous cold storage media. However, to enable this approach, the air used as the working fluid needs to be preconditioned to remove its moisture content before going into the power generation turbomachinery and PTES systems. In addition, the humidity of the working fluid air during operation needs to be at a certain level to avoid freezing at the cold side low-temperature end, which can be as low as -30°C. Adsorption methods were considered to remove the moisture content. The moist air flows over a hygroscopic material and is dried as the molecules of liquid or gases adhere onto the surfaces of the hygroscopic material. Figure 65 illustrates this process using a desiccant wheel to dry air. The desiccant is then recovered by regenerative hot air at 70°C for the next cycle.

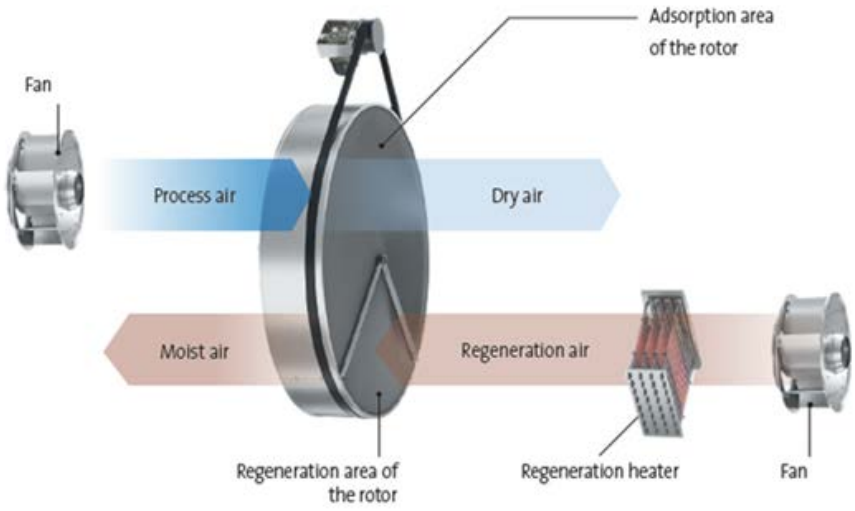

Figure 65. Desiccant drying principle

Table 16 shows the technical and operation specifications of a desiccant dryer sample product used to precondition air and maintain air humidity during operation. The advantage of a desiccant dryer is that it is a pure physical process that does not need a large pressure head to pass through the device. However, the desiccant regenerative process consumes a large amount of electric power, especially in the preconditioning stage.

Table 16. Technical Specifications of a Desiccant Dryer Product from Condair Group as the Moisture Removal Device Design Basis

Parameters	Units	Value of Sample Product
Drying capacity at 20°C, 60% relative humidity	kg/h	182
Nominal process air volume	m^3/h	27,900
Nominal regeneration air volume	m^3/h	6,980
Temperature/humidity range	-	-30°C–40°C, 0%–100% relative humidity
Total electrical load	kW	309
Process air static pressure	Pa	400
Regeneration air static pressure	Pa	250

In the air preconditioning process shown in Figure 66(a), ambient air at 15°C is passed through the desiccant dryer and is stored in a working fluid air inventory tank, which is assumed to be large enough to support system operation for up to 30 minutes. The total amount of air in inventory is 534,060 kg. This requires the desiccant dryer to operate for 2.834 h to fully fill the air inventory tank. The total electric power consumed in the preconditioning process is 2.834 MWh. This is an acceptable energy requirement, as the preconditioning process is only required to be performed once (in the initialization of the system).

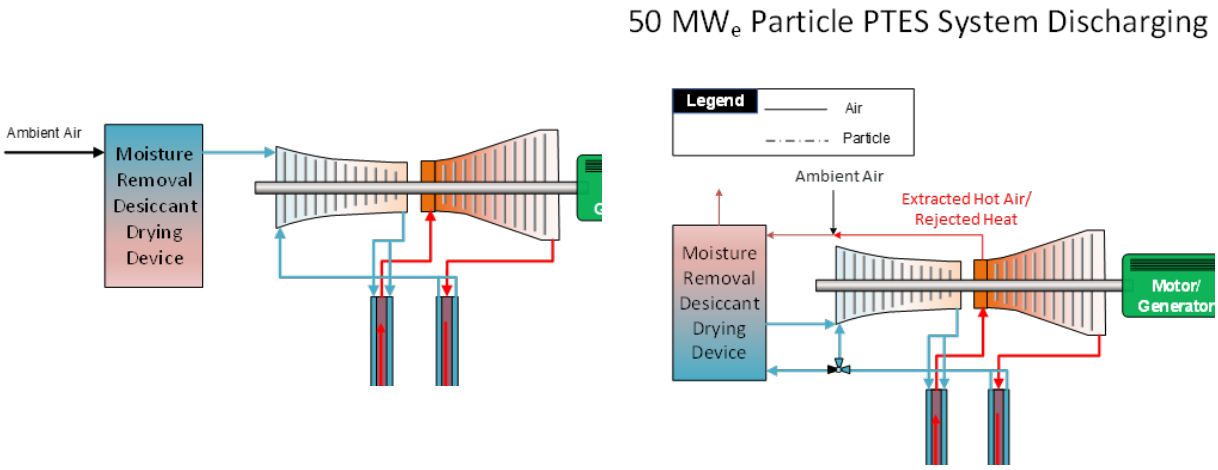

(a) Air preconditioning process (b) Air humidity maintenance process

Figure 66. Moisture removal processes

Based on the temperature range of process air passing through the desiccant shown in Table 16, the only applicable location to remove moisture from the air during operation is between the cold side PFB HX outlet and the compressor inlet in the discharging process. The process air temperature at this location is -31.5°C. Given the desiccant dryer's capacity, the partial air flow is bypassed for moisture removal. The dry air then goes back and is mixed with the rest. This process continues until the required air humidity is reached. To save energy in the air humidity

maintenance process, the hot air extracted from the hot side PFB HX outlet at a temperature of 816.85°C is mixed with ambient air at a temperature of 15°C to provide the regenerative air at 70°C to recover the desiccant. This process is shown in Figure 66(b).

Table 17 shows the temperatures and flow rates of the extracted hot air and ambient air to provide the regenerative air. It needs to be mentioned that the extracted hot air should be made up to maintain the required air inventory. Another option is to use the rejected heat in the power cycle to recover desiccant, which depends on the design of power system.

Table 17. Operating Conditions of Air Humidity Maintenance Process

Parameters	Units	Value
Process air temperature	°C	-31.5
Extracted air mass flow rate at hot side PFB outlet	kg/s	4.71
Extracted air temperature at hot side PFB outlet	°C	816.85
Required ambient air mass flow rate mixing with extracted air	kg/s	3.183
Ambient air temperature	°C	15
Desiccant regenerative temperature	°C	70

5.2 Identify Cost Correlations for Equipment Used in P-PTES

We developed an economic model to evaluate the capital cost and LCOS. The component costs described here provide the inputs used in the techno-economic comparisons in Task 1. Due to numerous uncertainties and assumptions, we applied a Monte Carlo sampling method, which enables uncertainty quantification. The economic model follows the method described in [4], in which several cost correlations are gathered for each component. The probabilistic sampling approach evaluates the total capital cost numerous times—each time randomly choosing which correlations are used. After thousands of samples, a smooth cost distribution is obtained, from which statistics such as the mean and standard deviation are obtained. This method, and the correlations explicitly described in the Supplementary Information of [4], are used to evaluate the capital cost of MS-PTES. It should be noted that these correlations were developed at different points in time. Therefore, the cost estimates are scaled to 2023 values using the Chemical Engineering Cost Indices. (The MS-PTES economic results presented in [4] used 2019 values, and this led to a cost increase of ~30% in this study.)

Cost correlations are not available for some of the novel components used in P-PTES. However, a detailed bottom-up cost estimation tool was developed as part of the ARPA-E-funded ENDURING project. The ENDURING concept is an energy storage device with electrically heated particle TES. The stored heat is then discharged through a modified combined cycle power plant. Cost models were developed for the PFB HXs, particle silos, skip hoists, lock hoppers, and pipelines, and detailed information is given in [37]. Correlations for how these costs depend on major design parameters were developed and are presented in Table 18. In this work, the cost of P-PTES is estimated using (1) the correlations in Table 18 for PFB HXs and storage systems and (2) the correlations from [4] for the turbomachinery, fans, heat rejection HX, motor, and generator. Note that [13] provided turbomachinery cost estimates based on combined cycle gas turbines, but these estimates are not used in this work. Due to this (and other

differences in the financial model), the results here cannot be directly compared to the economic results of the ENDURING system, because the goal of this work is to make a direct comparison between PTES systems that use either particle storage or molten salt storage.

The correlations in Table 18 do not inherently include an uncertainty term. Uncertainty is therefore estimated by assuming that these costs follow a normal distribution: The mean is given by the value in Table 18, and the standard deviation is assumed to be 40% of the mean—i.e., $\sigma/\mu = 0.4$. The probabilistic sampling approach randomly samples the probability distribution of each component to estimate its cost and thus creates a probability distribution of the total cost in the same manner as the MS-PTES system.

The capital cost C_{cap} is evaluated by summing the component costs and multiplying by a factor that accounts for contingency f_{cont}, such that:

$$C_{\mathrm{cap}} = f_{\mathrm{cont}} \sum C_{\mathrm{component}} \tag{28}$$

where f_{cont} is assumed to be in the 1.0–1.5 range. The capital cost may be decomposed into costs relating to the power systems C_P (\$/kW$_e$) and costs relating to the energy storage system C_E (\$/kWh$_e$). Turbomachinery, PFB HX, HXs, motor/generator, pumps, and fans all contribute to C_P, whereas storage containment, storage media, skip hoists, and lock hoppers contribute to C_E. The total capital cost can be represented as $C_{\mathrm{cap}} = (C_P + C_E \tau_{\mathrm{dis}}) \dot{W}_{\mathrm{dis}}$. This equation can be rewritten as the capital cost per unit energy capacity (\$/kWh):

$$\frac{C_{\mathrm{cap}}}{\tau_{\mathrm{dis}} \dot{W}_{\mathrm{dis}}} = \frac{C_P}{\tau_{\mathrm{dis}}} + C_E \tag{29}$$

which decreases asymptotically toward C_E for very large discharge durations. Therefore, C_E is an important parameter for long-duration electricity storage (LDES) systems, and large values of C_P may be permissible at large enough energy capacities. It should be noted that C_E itself may be a function of τ_{dis} as larger storage tanks achieve economies of scale.

The LCOS is a representation of the lifetime cost of the storage system, and accounts for operations and maintenance costs, $O\&M$, and electricity purchases. It is calculated using the formulation derived by ARPA-E [38], which allows some comparison with other LDES results:

$$LCOS = \left[C_E + C_P/\tau_{\mathrm{dis}} + \sum_{t=1}^{T} \frac{P_{el}(1/\eta_{RT} - 1) N_{\mathrm{cyc}} + \mathrm{O\&M}}{(1+r)^t} \right] \cdot \left[\sum_{t=1}^{T} \frac{N_{\mathrm{cyc}}}{(1+r)^t} \right]^{-1} \tag{30}$$

where O&M is the annual operations and maintenance cost (1%–5% of the total capital cost); P_{el} is the average price at which electricity is purchased (0.01–0.05 \$/kWh$_e$); N_{cyc} is the number of charge-discharge cycles per year (up to a maximum of 365); r is the discount rate, assumed to be in the range of 5%–15%; and T is the lifetime in years (35–25 y). Ranges are given for each of these parameters, as they are also randomly sampled by the Monte Carlo cost calculation method.

Table 18. Cost Correlations Used for P-PTES Components

System	Subsystem	Empirical Formulas	Notes
TES	Silo containment	$C_{silo} = 177{,}014\ M_{silo}^{0.27}$	M_{silo} is particle mass [metric tonnes] with a maximum size of 22,500 tonnes.
	Insulation material	$C_{insulation} = aT_p - b$ $a = 0.3477M_{silo} + 424.9$ $b = 79.47M_{silo} + 97{,}134.4$	M_{silo} is particle mass in metric tonnes. T_p is particle temperature in degrees Celsius.
	Media	$C_{media} = 35M_{silo}$	M_{silo} is particle mass in metric tonnes.
Skip Hoist	-	$C_{skip} = a\dot{m}_{\text{particle}} + b$ $a = 12.5H + 2219.9$ $b = 544.7H + 193458$	$\dot{m}_{\text{particle}}$is particle mass flow rate in kg/s. H is skip hoist height in m.
Hot Lock Hopper	Lock hopper	$C_{hot,loc} = 24.23M_{silo} + 551{,}314$	M_{silo} is particle mass in metric tonnes.
Cold Lock Hopper	Lock hopper	$C_{cold,loc} = 15.14M_{silo} + 423{,}929$	M_{silo} is particle mass in metric tonnes.
Hot PFB HX	Hot pressure vessel	$C_{FPV} = a\dot{Q}^2 + b\dot{Q} + c$ $a = 276.046p - 18.519$ $b = -149338.52p + 14976.11$ $c = 22346816.15p - 2567947.71$	$\dot{Q}$ is heat transferred in MW_{th}. p is pressure in bars.
	Hot HX	$C_{HX,hot} = 91.43\dot{Q}^2 - 4560\dot{Q} + 8.357 \times 10^5$	$\dot{Q}$ is heat transferred in MW_{th}.
	Hot cyclone	$C_{cyc,hot} = 7.18\dot{Q}^2$	$\dot{Q}$ is heat transferred in MW_{th}.
Cold PFB HX	Cold pressure vessel	$C_{FPV} = a\dot{Q}^2 + b\dot{Q} + c$ $a = 416.92p + 9.241$ $b = -177751.21p + 740.01$ $c = 21003554.51p - 429921.24$	$\dot{Q}$ is heat transferred in MW_{th}. p is pressure in bars.
	Cold HX	$C_{HX,cold} = 151.38\dot{Q}^2 - 5870\dot{Q} + 8.359 \times 10^5$	$\dot{Q}$ is heat transferred in MW_{th}.
	Cold cyclone	$C_{cyc,cold} = 20.858\dot{Q}^2 - 3623\dot{Q} + 4.9684 \times 10^5$	$\dot{Q}$ is heat transferred in MW_{th}.
PFB HX	Piping	$\frac{C_{piping}}{L} = a\dot{Q} + b$ $a = 34.854p + 109.78$ $b = 147.46p + 8345.5$	$\dot{Q}$ is heat transferred in MW_{th}. p is pressure in bars L is pipe length; here, $L = 10\ m$.

5.3 Predict System LCOS for Optimal Cycle Configurations

The parametric studies in Section 1 are used to inform an improved P-PTES design, which is compared to an optimal MS-PTES design from previous work. The design and performance of these systems are presented in Table 19.

The MS-PTES design is based on the results of a multi-objective optimization in[4] and corresponds to a nitrate molten salt design that minimized the LCOS (referred to as case N2 in [4]). This design used an HX effectiveness of 95.6%, which corresponds to average approach temperatures of 11.5°C, 3.8°C, and 15.1°C in the hot and cold HX and recuperator, respectively. This design did not maximize HX performance due to its strong influence on capital cost. The MS-PTES design has $\eta_{RT} = 56.7\%$ and LCOS = 0.171 ± 0.04 \$/kWh$_e$ for a discharge duration of 10 h.

The P-PTES design uses a 2.5°C approach temperature. The pressure ratio was varied to find the value that minimized the LCOS, which in this case is 4.3. The properties of silica particles and PFB HXs enable P-PTES to operate at higher maximum temperatures and lower approach temperatures than MS-PTES. This improved design has $\eta_{RT} = 66.1\%$ and $w_{\text{out}} = 229.8\ \text{kJ/kg}$ —double that of MS-PTES. A breakdown of exergy losses is shown in Figure 67, which shows that the P-PTES design reduces losses primarily in the turbomachinery and HXs. Heat rejection losses increase slightly because P-PTES rejects heat at a higher temperature than MS-PTES.

Table 19. Techno-Economic Performance of Improved Designs

Parameter		**MS-PTES**		**P-PTES**	
Approach temperature, $\boldsymbol{\Delta T}$	°C	-		2.5	
Effectiveness, $\boldsymbol{\varepsilon}$	%	95.6		-	
Pressure loss, $\boldsymbol{f_p}$	%	0.65		4.00	
Charge pressure ratio	-	3.2		4.3	
T_1	°C	320		447	
T_2	°C	570		827	
T_3	°C	334		34	
T_4	°C	43		-62	
T_5	°C	-40		447	
T_6	°C	27		-	
Round-trip efficiency	%	56.7		66.1	
Specific work output	kJ/kg	111.7		229.8	
Discharge power output	MW$_e$	100	100	100	100
Discharge duration	h	10	100	10	100
Hot storage volume	m^3	29,446	285,261	11,543	115,430
Cold storage volume	m^3	39,966	386,073	11,543	115,430
Capital cost	M\$	362 ± 90	717 ± 167	245 ± 55	379 ± 73
Power capital cost, $\boldsymbol{C_P}$	\$/kW$_e$	3103	3105	2048	2050
Energy capital cost, $\boldsymbol{C_E}$	\$/kWh$_e$	52	41	40	17
LCOS	\$/kWh$_e$	0.171 ± 0.04	0.265 ± 0.06	0.115 ± 0.03	0.144 ± 0.03

The improved technical performance of P-PTES translates to significant cost reductions: For a 10-h discharge duration, the capital cost is 32% lower than that of MS-PTES, while the LCOS is 0.115 ± 0.03 \$/kWh$_e$, which is a reduction of 32%. Cost reductions occur in the turbomachinery, HXs, and storage systems, as shown in Figure 68. These cost reductions arise due to a higher specific work output, which reduces the mass flow rate and therefore the size (and cost) of the turbomachinery and HXs. Direct-contact heat exchange in the PFB HXs enables high-efficiency heat transfer at low cost, which therefore leads to high round-trip efficiency. In turn, this helps reduce the size and cost of the charging components. Results indicate that a particle-based storage system is also considerably cheaper than a molten salt system. This is partly due to the lower material costs of particles, but also due to the larger operating temperature range, which increases energy density and substantially reduces storage volumes, as shown in Table 19.

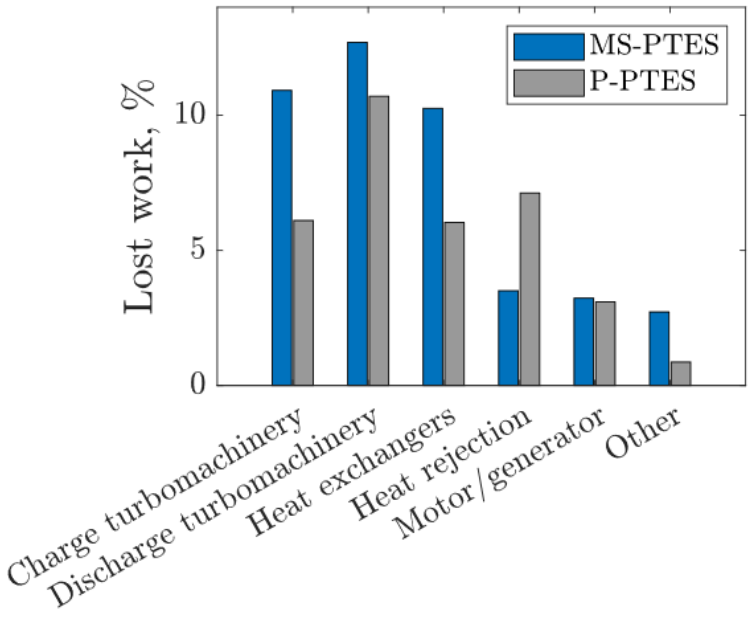

Figure 67. Distribution of exergy losses in each type of component for the improved MS-PTES and P-PTES designs

Results have so far been presented for systems with a discharge duration of 10 hours. However, PTES systems have low marginal costs of energy capacity—i.e., additional storage hours can be added at low cost, because TES materials have low capital costs, and because the energy capacity and power capacity are decoupled. Figure 69 illustrates the capital cost per unit energy capacity as a function of storage duration for the improved MS-PTES and P-PTES designs. The cost per unit energy $C_{cap} \,/\, \tau_{\mathrm{dis}}\dot{W}_{\mathrm{dis}}$ decreases with storage duration. Furthermore, $C_{cap} \,/\, \tau_{\mathrm{dis}}\dot{W}_{\mathrm{dis}}$ asymptotically approaches the cost of energy capacity C_E for long storage durations. At $\tau_{dis} = 100$ h, $C_{cap}/\tau_{\mathrm{dis}}\dot{W}_{\mathrm{dis}}$ = \$38/kWh$_e$, whereas C_E = \$17/kWh$_e$, which illustrates the smaller contribution from C_P at long storage durations and emphasizes the importance of developing systems with low values of C_E for LDES applications.

It should be noted that C_E decreases as τ_{dis} increases: For P-PTES, C_E reduces from \$40/kWh$_e$ to \$17/kWh$_e$ when τ_{dis} increases from 10 h to 100 h (see Table 5). This reduction is partly due to

economies of scale; for example, larger silos have lower costs per unit size than smaller silos. Moreover, at long storage durations, the required particle volume exceeds the maximum silo capacity, so multiple silos are required. For 100-h discharge duration, eight silos are required to store hot particles (and another eight are required for cold particles). Two more empty silos are constructed (one hot and one cold), which enables particles to be moved from one silo to another during the discharging process. Therefore, one-ninth of the silo inventory is empty. On the other hand, for 10-h discharge duration, only one hot silo and one cold silo are required to contain the particles, but an additional buffer silo helps particle transfer to completely empty a storage silo. Thus, the buffer silo inventory is one-half, which indicates that capital is invested more efficiently at long discharge durations. This observation is also true for MS-PTES, which demonstrates a reduction in C_E from \$51/kWh$_e$ to \$41/kWh$_e$.

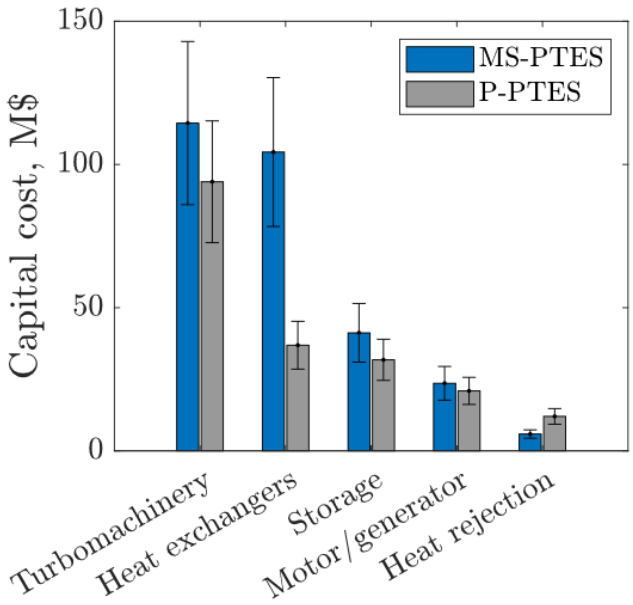

Figure 68. Distribution of capital costs for each type of component for the improved MS-PTES and P-PTES designs with 10-h discharge duration. Error bars correspond to one standard deviation.

For comparison, Figure 69 shows cost estimates for lithium-ion batteries based on values in NLR's 2023 Annual Technology Baseline [39], which uses a variety of source data [40]. To account for rapidly decreasing lithium-ion cell prices in 2023–2024 [41], the costs taken from the Annual Technology Baseline reflect 2030 prices and consider the moderate to advanced cost estimates. Therefore, C_P = \$184/kW$_e$–\$317/kW$_e$ and C_E =\$199/kWh$_e$–\$246/kWh$_e$. (Note that these values are higher than sometimes quoted costs in the range of \$50/kWh$_e$–\$100/kWh$_e$, as those costs only reflect the battery cells, which must then be packaged into battery packs and installed, leading to increased total costs.) Also shown in Figure 69 is an aggressive cost prediction for lithium-ion of \$100/kWh$_e$. Both MS-PTES and P-PTES can outcompete current lithium-ion prices for long discharge durations. The crossover point occurs at a lower τ_{dis} for P-PTES (8 h) than for MS-PTES (13 h), but for $\tau_{\mathrm{dis}} > 50$ h, both MS-PTES and P-PTES are less than half of lithium-ion costs. At $\tau_{\mathrm{dis}} = 100$ h, P-PTES costs are nearly half of MS-PTES (\$38/kWh$_e$ compared to \$72/kWh$_e$), which emphasizes the significant advancements that particle thermal storage can provide. Therefore, even in scenarios where lithium-ion costs are reduced to

$100/kWh_e$, P-PTES systems can provide significant cost reductions, whereas MS-PTES cost reductions may be viewed as only a marginal improvement over lithium-ion.

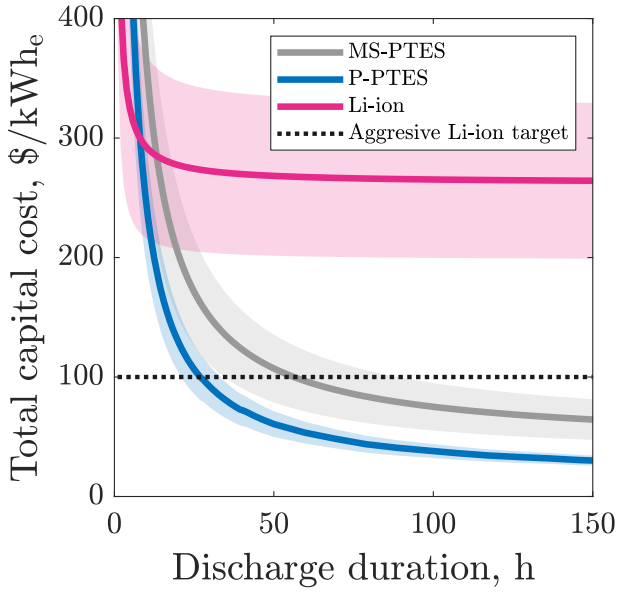

Figure 69. Total capital cost as a function of storage duration. Capital cost is divided by total electrical energy output per cycle. Shaded areas represent one standard deviation.

In summary, Figure 69 indicates the competitive costs of P-PTES systems. P-PTES has lower capital costs than MS-PTES for all discharge durations: By reducing the cost of storage containment and media—and by reducing the cost of HXs—P-PTES costs are approximately half those of MS-PTES. Furthermore, P-PTES achieves lower costs than lithium-ion batteries for discharge durations over 10 h, and outcompetes aggressive lithium-ion predictions for durations greater than 27 h.

Task 5 studied the risks of using sand TES for cold storage on moisture control for sub-zero operation. A thorough TEA was performed on component cost functions to illustrate scenarios for the PUMP system to support long duration energy storage.

Project Outcomes

Summary of Technology Achievements

- Developed system configurations and corresponding modeling tools for PTES thermodynamic cycle analysis and high-temperature (>1,000°C) particle-based TES and CSP integration for high-efficiency (>55%) long-duration energy storage (>10 hours).
- Investigated key components of particle TES—storage containment, particle handling, and HXs—to enable cost-effective hot side and cold side TES of a PTES system.
- Studied the sensitivity of storage cycle efficiency with respect to process design points and operation conditions to define component requirements and sizing, and paved the way for bottom-up cost analysis.
- Validated PFB HX operation principles via prototype development and testing, and demonstrated the first air/particle direct-contact HX by achieving an air-side exit approach temperature of <15°C.
- Laid the foundation for pilot demonstration and scale-up of electrothermal energy storage technology using particle TES.
- Published papers, a book chapter, an awarded patent, and new patent applications to disseminate the learning from research and development.
- Conducted industry outreach aimed at broad applications of particle TES for CSP, electrothermal energy storage, industrial process heat, and nuclear energy integration:
    - Particle TES has the potential to achieve **grid-scale energy storage** at a fraction of the cost of conventional chemical battery technologies.
    - The ability to provide **baseload power for several days** allows for continued grid integration of intermittent renewable sources.
    - Particle TES has siting flexibility and the potential to leverage the infrastructure of coal- and gas-fired power plants for reduced capital cost.

A. Journal Articles

1. Jeong, S. Y., Hirschey, J., Shah, M. P., Gifford, J., Martinek, J., and Ma, Z., 2025, "Particle Handling in Particle-Based Pumped Thermal Energy Storage," Journal of Energy Resources Technology, Part A: Sustainable and Renewable Energy, **1**(5).
2. Ma, Z., X. Wang, P. Davenport, J. Gifford, and J. Martinek. 2022. "Preliminary Component Design and Cost Estimation of a Novel Electric-Thermal Energy Storage System Using Solid Particles." *Journal of Solar Energy Engineering* 144 (3): 030901. https://doi.org/10.1115/1.4053256.
3. McTigue, J., J. Hirschey, and Z. Ma. 2025. "Advancing Pumped Thermal Energy Storage Performance and Cost Using Silica Storage Media." *Applied Energy* 387, 125567. https://doi.org/10.1016/j.apenergy.2025.125567.
4. McTigue, J., and Z. Ma. 2025. "Analysis of Pumped Thermal Energy Storage Using Particle Media Integrated With Concentrating Solar Power." *Solar Energy* 292, 113436. https://doi.org/10.1016/j.solener.2025.113436.

B. Papers (Manuscripts in Preparation)

1. Z. Ma, J. Martinek, J. McTigue, C. Turchi, C. Ho, J. Sment, (2022), "Thermal Energy Storage for Energy Decarbonization," to *Annual Heat Transfer Review*, edited by Prof. Zhuomin Zhang, Begell House.
2. Hirschey, J., S. Jeong, U. Patel, J. McTigue, M. Shah, and Z. Ma. "Demonstration of a Counterflow Direct Contact Solid-Gas Heat Exchanger for Particle-Based Thermal Energy Storage." *Drafted.*
3. Mubashar Ashraf, M., J. Gifford, M. Shah, S. Jeong, J. Martinek, J. Hirschey, and Z. Ma. "Computational Fluid Dynamic Modeling of Direct-Contact, Counter-Flow Fluid Bed Heat Exchanger: Validation and Sensitivity." *Draft in progress.*
4. Mubashar Ashraf, M., J. Gifford, M. Shah, and Z. Ma. "System Modeling of a Particle-Based, Pumped Thermal Energy Storage System: Performance and Control Operations." *Draft in progress.*

C. Status Reports (Conference and Workshop Presentations)

1. Ma, Z. 2025. "Thermal Energy Storage for Industry Process Energy Supply", Germany-US Energy Economic Forum, February 28, 2025.
2. Ma, Z. 2024. "System and Component Development of a Thermal Battery Using Low-Cost Stable Solid Particles." International Workshop on Carnot Batteries, German Aerospace Center (DLR), September 28, 2024.
3. Gifford J., X. Wang, J. Wang, Z. Ma, and R. Braun. 2022. "A System Modeling Platform for Particle-Based Thermal Energy Storage Systems for Long-Duration Energy Storage Applications." SolarPACES Conference 2022 (Oral Presentation Accepted).

D. Patent Applications/Issued Patents

1. Ma, Z., S. Jeong, J. Gifford, J. Hirschey, M. Shah, U. Patel, J. Martinek, NLR 25-36 "Modular Particle Thermal Energy Storage System for Distributed Energy Supply, USPTO Provisional Patent Application #63/772,133 (2025).
2. Ma, Z., Davenport, P. G., & Martinek, J. (2023). Particle-based Thermal Energy Storage Systems, U.S. Patent # 11,808,523 B2.
3. Ma, Z., Gifford, J., Davenport, P., & Wang, X. (2023). Fluidized-bed heat exchanger for conversion of thermal energy to electricity", US Patent No. 11,740,025, B2.
4. Ma, Z. 2022. Methods and Systems for Thermal Energy Storage and Their Use in Heating and Cooling. U.S. Patent No. US 11,480,395 B2, October 25, 2022.

E. Awards, Prizes, and Recognition

- Loiy Al-Ghussain, T. Johnson, J. Martinek, Z. Ma, Techno-Economic Feasibility Analysis of Solar Industrial Process Heat Using Particle Thermal Energy Storage, ES2024-131139, ASME Energy Sustainability 2024, Anaheim, California, July 15-17, 2024. **Received the Best Paper award by 2024 ES conference.**
- X. Zhang, S. Adapa, Z. Ma, R. Chen, Probing Thermal Transport in Fluidized Bed Using Modulated Photothermal Radiometry, ES2024-131247, ASME Energy Sustainability

2024, Anaheim, California, July 15-17, 2024. **Received the Best Paper award by 2024 ES conference.**

- Gifford, J., Davenport, P., Wang, X., & Ma, Z. (2023). Fabrication, Modeling, and Testing of a Prototype for Particle Thermal Energy Storage Containment. *Proceedings of the ASME 2023 17th International Conference on Energy Sustainability*. **Received the 1st place in Best Paper award by 2023 ES conference**.

References

[1] Ma, Z., Wang, X., Davenport, P., Gifford, J., and Martinek, J., 2021, "Preliminary Component Design and Cost Estimation of a Novel Electric-Thermal Energy Storage System Using Solid Particles," J Sol Energy Eng, **144**(3).

[2] Laughlin, R. B., 2020, "Mass Grid Storage with Reversible Brayton Engines," *Thermal, Mechanical, and Hybrid Chemical Energy Storage Systems*, K. Brun, T. Allison, and R. Dennis, eds., Elsevier.

[3] Ma, Z., McTigue, J., Gifford, J., Hirschey, J., Jeong, S. Y., Shah, M. P., and Martinek, J., 2024, "System and Component Development of Particle-Based Pumped Thermal Energy Storage," *Proceedings of the ASME 2024 18th International Conference on Energy Sustainability*, Anaheim, California, pp. 1–8.

[4] McTigue, J. D., Farres-Antunez, P., J, K. S., Markides, C. N., and White, A. J., 2022, "Techno-Economic Analysis of Recuperated Joule-Brayton Pumped Thermal Energy Storage," Energy Convers Manag, **252**, p. 115016.

[5] Mehos, M., Turchi, C., Vidal, J., Wagner, M., Ma, Z., Ho, C., Kolb, W., Andraka, C., and Kruizenga, A., 2017, *Concentrating Solar Power Gen3 Demonstration Roadmap*, Golden, CO (United States).

[6] Ma, Z., Wang, X., Davenport, P., Gifford, J., Cook, K., Martinek, J., Schirck, J., Morris, A., Lambert, M., and Zhang, R., 2022, "System and Component Development for Long-Duration Energy Storage Using Particle Thermal Energy Storage," Appl Therm Eng, **216**, p. 119078.

[7] Ma, Z., Wang, X., Davenport, P., Gifford, J., Martinek, J., Schirck, J., Morris, A., Lambert, M., and Zhang, R., 2022, "System and Component Development for Long-Duration Energy Storage," Appl Therm Eng, p. 119078.

[8] Ma, Z., Martinek, J., Turchi, C., McTigue, J., Sment, J., and Ho, C., 2022, "Thermal Energy Storage for Energy Decarbonization," Annual Review of Heat Transfer, (i), pp. 51–115.

[9] Ma, Z., Martinek, J., Turchi, C., McTigue, J., Sment, J., and Ho, C., 2022, "THERMAL ENERGY STORAGE FOR ENERGY DECARBONIZATION," *Annual Review of Heat Transfer*.

[10] Bell, I. H., Wronski, J., Quoilin, S., and Lemort, V., 2014, "Pure and Pseudo-Pure Fluid Thermophysical Property Evaluation and the Open-Source Thermophysical Property Library CoolProp," Ind Eng Chem Res, **53**(6), pp. 2498–2508.

[11] Nagorny, A. S., Dravid, N. V, Jansen, R. H., and Kenny, B. H., 2005, "Design Aspects of a High Speed Permanent Magnet Synchronous Motor / Generator for Flywheel Applications," *IEEE International Conference on Electric Machines and Drives, 2005.*, pp. 635–641.

[12] Gifford, J., Ma, Z., Wang, X., and Braun, R., 2023, "Computational Fluid Dynamic Analysis of a Novel Particle-to-Air Fluidized-Bed Heat Exchanger for Particle-Based Thermal Energy Storage Applications," J Energy Storage, **73**, p. 108635.
[13] Ma, Z., 2023, *Economic Long-Duration Electricity Storage by Using Low-Cost Thermal Energy Storage and High-Efficiency Power Cycle (ENDURING)*, Golden, CO (United States).
[14] Olympios, A. V., McTigue, J. D., Sapin, P., and Markides, C. N., 2022, "Pumped-Thermal Electricity Storage Based on Brayton Cycles," Encyclopedia of Energy Storage: Volume 1-4, **1–4**, pp. 6–18.
[15] Jeong, S. Y., Hirschey, J., Shah, M. P., Gifford, J., Martinek, J., and Ma, Z., 2025, "Particle Handling in Particle-Based Pumped Thermal Energy Storage," Journal of Energy Resources Technology, Part A: Sustainable and Renewable Energy, **1**(5).
[16] Valero, A., Lozano, M. A., Serra, L., Tsatsaronis, G., Pisa, J., Frangopoulos, C., and von Spakovsky, M. R., 1994, "CGAM Problem: Definition and Conventional Solution," Energy, **19**(3), pp. 279–286.
[17] Fiaschi, D., Manfrida, G., Petela, K., and Talluri, L., 2019, "Thermo-Electric Energy Storage with Solar Heat Integration: Exergy and Exergo-Economic Analysis," Energies (Basel), **12**(4), p. 648.
[18] Benato, A., 2017, "Performance and Cost Evaluation of an Innovative Pumped Thermal Electricity Storage Power System," Energy, **138**, pp. 419–436.
[19] Chen, L. X., Hu, P., Zhao, P. P., Xie, M. N., and Wang, F. X., 2018, "Thermodynamic Analysis of a High Temperature Pumped Thermal Electricity Storage (HT-PTES) Integrated with a Parallel Organic Rankine Cycle (ORC)," Energy Convers Manag, **177**, pp. 150–160.
[20] Petrollese, M., Cascetta, M., Tola, V., Cocco, D., and Cau, G., 2022, "Pumped Thermal Energy Storage Systems Integrated with a Concentrating Solar Power Section: Conceptual Design and Performance Evaluation," Energy, **247**, p. 123516.
[21] Farrés-Antúnez, P., 2018, "Modelling and Development of Thermo-Mechanical Energy Storage," University of Cambirdge.
[22] Cascetta, M., Licheri, F., Merchán, R. P., and Petrollese, M., 2023, "Operating Performance of a Joule-Brayton Pumped Thermal Energy Storage System Integrated with a Concentrated Solar Power Plant," J Energy Storage, **73**, p. 108865.
[23] Neises, T., 2020, "Steady-State off-Design Modeling of the Supercritical Carbon Dioxide Recompression Cycle for Concentrating Solar Power Applications with Two-Tank Sensible-Heat Storage," Solar Energy, **212**, pp. 19–33.
[24] McTigue, J. D., Farres-Antunez, P., Neises, T., and White, A., 2022, "Supercritical CO2 Heat Pumps and Power Cycles for Concentrating Solar Power," p. 090006.
[25] Subires, A. J., Rovira, A., and Muñoz, M., 2024, "Proposal and Study of a Pumped Thermal Energy Storage to Improve the Economic Results of a Concentrated Solar Power That Works with a Hybrid Rankine–Brayton Propane Cycle," Energies (Basel), **17**(9), p. 2005.
[26] Ho, C. K., and Iverson, B. D., 2014, "Review of High-Temperature Central Receiver Designs for Concentrating Solar Power," Renewable and Sustainable Energy Reviews, **29**, pp. 835–846.

[27] Ma, Z., Zhang, R., and Sawaged, F., 2017, "Design of Particle-Based Thermal Energy Storage for a Concentrating Solar Power System," *ASME 2017 11th International Conference on Energy Sustainability*, American Society of Mechanical Engineers.
[28] Ma, Z., Martinek, J., Turchi, C., McTigue, J., Sment, J., and Ho, C., 2022, "Thermal Energy Storage for Energy Decarbonization," Annual Review of Heat Transfer, **25**(1), pp. 51–115.
[29] Ma, Z., Wang, X., Davenport, P., Gifford, J., Cook, K., Martinek, J., Schirck, J., Morris, A., Lambert, M., and Zhang, R., 2022, "System and Component Development for Long-Duration Energy Storage Using Particle Thermal Energy Storage," Appl Therm Eng, **216**, p. 119078.
[30] Ma, Z., McTigue, J., Gifford, J., Hirschey, J., Jeong, S. Y., Shah, M. P., and Martinek, J., 2024, "System and Component Development of Particle-Based Pumped Thermal Energy Storage," *ASME 2024 18th International Conference on Energy Sustainability*, American Society of Mechanical Engineers.
[31] White, A., Parks, G., and Markides, C. N., 2013, "Thermodynamic Analysis of Pumped Thermal Electricity Storage," Appl Therm Eng, **53**(2), pp. 291–298.
[32] McTigue, J. D., White, A. J., and Markides, C. N., 2015, "Parametric Studies and Optimisation of Pumped Thermal Electricity Storage," Appl Energy, **137**, pp. 800–811.
[33] Sciacovelli, A., Li, Y., Chen, H., Wu, Y., Wang, J., Garvey, S., and Ding, Y., 2017, "Dynamic Simulation of Adiabatic Compressed Air Energy Storage (A-CAES) Plant with Integrated Thermal Storage – Link between Components Performance and Plant Performance," Appl Energy, **185**, pp. 16–28.
[34] Zhang, N., and Cai, R., 2002, "Analytical Solutions and Typical Characteristics of Part-Load Performances of Single Shaft Gas Turbine and Its Cogeneration," Energy Convers Manag, **43**(9–12), pp. 1323–1337.
[35] Dixon, S. L. ., and Hall, C. A. ., 2014, *Fluid Mechanics and Thermodynamics of Turbomachinery*, Butterworth-Heinemann.
[36] McTigue, J., Hirschey, J., and Ma, Z., 2025, "Advancing Pumped Thermal Energy Storage Performance and Cost Using Silica Storage Media," Appl Energy, **387**, p. 125567.
[37] McTigue, J., and Ma, Z., 2024, "A Dual-Mode Hybrid System Combining Solar Thermal With Pumped Thermal Energy Storage," SolarPACES Conference Proceedings, **2**.
[38] ARPA-E, 2018, "Funding Opportunity Announcement: Duration Addition to Electricity Storage (DAYS)," Funding Opportunity No. DE-FOA-0001906.
[39] National Laboratory of the Rockies, 2023, *2023 Annual Technology Baseline*.
[40] Cole, W., and Karmakar, A., 2023, *Cost Projections for Utility-Scale Battery Storage: 2023 Update*, Golden, CO (United States).
[41] McKerracher, C., 2024, "China's Batteries Are Now Cheap Enough to Power Huge Shifts," Bloomberg.